

**GAS PHASE SYNTHESIS OF MAGNETIC
NANOCOMPOSITE MATERIALS AND ITS
APPLICATION IN ANISOTROPIC-EXCHANGE-SPRING
MAGNETS**

A DISSERTATION
SUBMITTED TO THE FACULTY OF THE GRADUATE SCHOOL
OF THE UNIVERSITY OF MINNESOTA
BY

XIAOQI LIU

IN PARTIAL FULFILLMENT OF THE REQUIREMENTS
FOR THE DEGREE OF
DOCTOR OF PHILOSOPHY

JIAN-PING WANG, ADVISER

October, 2009

©Xiaoqi Liu 2009

Acknowledgements

During my five-year's PhD study, I am really grateful to all the people around me. I couldn't imagine how I could reach today without their help and support. But the first one I would like to thank is my advisor Prof. Jian-Ping Wang. Not only because he did a great job on giving me a professional education in science and research, but also because the help he offered during my hard time when I was frustrated and hesitated about my work and life.

I would like to thank all my former and current lab mates, Dr. Jiaoming Qiu, Dr. Yunhao Xu, Dr. Jianming Bai, Dr. Hao Meng, Dr. Weikang Shen, Xiaofeng Yao, Haibao Zhao, Nian Ji, Hao Wang, Yisong Zhang, Yuanpeng Li, Ying Jing, Shihai He, Hui Zhao, Liang Tu for their help and valuable discussions among us. Especially I got a lot help and suggestions from Dr. Jiaoming Qiu, Dr. Yunhao Xu, and Dr. Jianming Bai at the beginning of my PhD study. In addition I would like to thank members from the Victora group, Stadler group and Leighton group, Manish Kapoor, Xiao Shen, Jyotirmoy Saha, Liwen Tan, Xiaobo Huang, Manish sharma, Michael Manno, Dr. Maria Torija, Chunyong He for help on discussion and VSM, SQUID measurements.

I would like to thank all the MINT faculties, Prof. Randall H. Victora, Prof. Jack H. Judy, Prof. Bethanie Stadler, and Prof. Chris Leighton. I really benefit a lot from all the MINT academic activities including seminars, the annual MINT review meeting and journal club. I also want to thank my final defense committee for examining my Ph.D. dissertation.

I would like to acknowledge Dr. Ozan Ugurlu and Dr. Joysurya Basu at the characterization facility center for TEM measurement, Dr. Mike Jackson and Dr. Julie A. Bowles at the Institute for Rock Magnetism (IRM) for magnetic characterization. Special acknowledgements go to INSIC-NIST-ATP HAMR program, Seagate Technology and Heraeus Corp. for their financial support.

To my parents and my brother

To my dear fiancé Lili

Abstract

The improvement of the properties of magnetic materials has reached a critical stage since it is more and more difficult to discover new materials to achieve higher performance. Nanocomposite material is a new generation of materials, which combines different materials in nano-scale to generate unachievable properties from single phase materials. Nanocomposite materials have very broad applications including permanent magnets, nanocrystalline magnetic soft materials, solar cells, biomedical materials and devices.

In this study, a novel gas phase synthesis process is developed for fabrication of nanocomposite materials. This technique represents a general process and is applicable to most materials. The synthesis system consists of a magnetron-sputtering-based gas-phase nanoparticle deposition source, conventional thin film sputtering sources and a modified substrate holder with external magnetic field generator. Anisotropic exchange-spring magnet with nanocomposite structure, based on a FePt/Fe-Ni system, has been successfully fabricated for the first time in this research work, through using the novel nanocomposite fabrication process. FePt/Fe-Ni anisotropic exchange-spring nanocomposite consists of exchange coupled $L1_0$ FePt hard phase and Fe-Ni soft phase. It has greatly enhanced the energy product compared to a single phase of FePt or Fe-Ni. This structure also has a defined easy-axis, thereby improving its energy product from the isotropic case (124%). Systematic magnetic and structural studies have been performed. The optimized hard phase volume ratio is found experimentally for the first time to be

around 10%, which confirms the theoretical finding by Skomski and Coey 15 years ago. Studies on materials with ultra-high crystalline anisotropy such as $L1_0$ FePt, $SmCo_5$ and materials with potential ultra-high saturation magnetization such as $Fe_{16}N_2$ are also included.

Contents

Acknowledgements	i
Abstract	iv
List of Tables	viii
List of Figures	ix
Chapter 1 Introduction	1
1.1 Material science developed into nanoscale	1
1.2 Magnetic nanocomposite materials and their applications	2
1.3 Outline of the thesis	3
Chapter 2 Synthesis methods of nano-structured materials	5
2.1 Introduction to synthesis methods of magnetic nano-structured materials	5
2.2 Physical vapor deposition (PVD) process	8
2.2.1 Thermal evaporation process	8
2.2.2 Sputtering process	11
2.3 Chemical vapor deposition (CVD) process	13
2.4 Thermodynamics in the formation of nanoparticles in gas phase.	14
2.4.1 Nucleation mechanism of nanoparticle in gas phase	14
2.4.2 Growth mechanism of nanoparticle in gas phase	17
2.4.3 Cooling processes to generating supersaturated vapor	19
2.5 Sputtering based gas phase synthesis process	21
2.6 Summary	23
References:	24
Chapter 3 Gas phase synthesis of magnetic nanocomposite materials	26
3.1 Introduction	26
3.2 A novel gas phase synthesis process	28
3.2.1 System setup	28
3.2.2 Introduction of FePt alloy	30
3.3 Energy control of gas phase nanoparticles formation	33
3.3.1 Initial Energies of Ar ⁺ ions, Fe, Pt atoms outside the plasma region.. ..	33
3.3.2 Energies of Ar ⁺ ions, Fe, Pt and Ar atoms in the plasma region... ..	35
3.3.3 Energy flow in plasma region	36
3.4 Important factors of gas phase nanoparticles synthesis	38
3.4.1 Aggregation time effect	38
3.4.2 Magnetic field effect	40
3.4.3 Gas pressure effect	46
3.4.4 Discharge current effect	50

3.5	Simultaneously control of phase and size of directly ordered L1 ₀ FePt nanoparticles	53
3.5.1	Experiment setup.....	53
3.5.2	Results and discussion	53
3.5.3	Summary	62
3.6	Matrix material fabrication and orientation control of magnetic nanocomposites	63
3.7	Advantages of the novel gas phase nanocomposite synthesis process.....	66
3.8	Summary	67
	References:.....	68
Chapter 4	Theoretical model of exchange-spring magnets.....	71
4.1	Introduction of exchange-spring magnets	71
4.2	Basic idea of exchange-spring magnets (2D model)	74
4.2.1	Reversal process of exchange-spring magnet	75
4.2.2	Critical dimensions of hard and soft phase	77
4.2.3	Exchange coupling strength	79
4.3	Two basic structures of exchange-spring magnets	81
4.4	Anisotropic and isotropic exchange-spring magnets	84
4.5	Summary	86
	References:.....	87
Chapter 5	Gas phase synthesis of FePt/Fe-Ni anisotropic exchange-spring magnets with nanocomposite structure	94
5.1	Introduction.....	94
5.2	Fabrication process	96
5.3	Microstructure	99
5.3.1	Shape and magnetic properties of L1 ₀ FePt nanoparticles..	99
5.3.2	Nanocomposite film characterization	100
5.3.3	In-plane easy axis alignment.....	101
5.4	Magnetic properties	106
5.5	Anisotropic vs. isotropic exchange-spring magnets	110
5.6	Hard phase volume effect	112
5.7	Experimental result versus theoretical calculation.....	116
5.8	Summary	118
	References:.....	119
Chapter 6	Conclusions and perspectives.....	122
6.1	Conclusions	122
6.2	Perspectives.....	123
	Bibliography:	125
	Appendix:	138
A	Localized Fe 3d electron states in Fe ₁₆ N ₂	138
B	Surface effects on the magnetization switching behavior of L1 ₀ FePt nanoparticle	151
C	Studies on SmCo ₅ with ultrahigh crystalline anisotropy	170

List of Tables:

Appendix A:

Table 1 Ratio R , orbital (M_o), spin (M_s) and total magnetic moment (M) of different Fe 3d states, extracted from XMCD spectra in Fig. 3. (M value of Fe_{16}N_2 phase was calculated from its saturation magnetization value. R value of Fe $3d^5$ and $3d^6$ were calculated from the spectra in ref. [28]. The magnetic moment of Fe $3d^5$ and $3d^6$ were calculated by Hund's rules.) 146

List of figures:

Figure 2.1 Synthesis methods of magnetic nano-structured materials.....	6
Figure 2.2 Two typical thermal evaporation systems using (a) resistive heating source and (b) electron beam heating source, respectively	9
Figure 2.3 Molecular beam epitaxy deposition system	10
Figure 2.4 (a) schematic drawing of a sputtering system (b) sputtering process on target surface.	12
Figure 2.5 Configuration of a sputtering based gas-phase nanoparticle synthesis system ^{10b} . K is a magnetron sputtering gun used for atom vapor generation. S is the substrate holder. Nanoclusters were formed under high pressure inert gas and swept out by carrier gas through vent-hole B1 and B2.	22
Figure 3.1 Schematic drawing of the novel gas phase synthesis system.	29
Figure 3.2 (a) fcc crystalline structure for A1 phase FePt ($c = a$) (b) fct crystalline structure for L1 ₀ phase FePt ($c = 0.96a$).....	32
Figure 3.3 Simplified configuration of the sputtering system	34
Figure 3.4 Energy source and energy flow during the sputtering based gas phase FePt nanoparticle synthesis process.....	36
Figure 3.5 FePt nanoparticle fabricated with different aggregation time. (a) 2.3 t_0 , (b) 1.6 t_0 , (c) 1.23 t_0 , and (d) t_0	39

Figure 3.6 Modification of the magnetic field on target surface.....	41
Figure 3.7 Contour plot of the magnetic flux density on the cross-section plane of the (a) conventional target configuration and (b) our new designed target configuration.	42
Figure 3.8 L ₁₀ FePt nanoparticle fabricated with different cone width. Cone widths used are (a) 10mm (b) 20mm (c) 25mm.....	45
Figure 3.9 L ₁₀ FePt nanoparticles fabricated at different gas pressure: (a) 390 mTorr, (b) 452 mTorr, (c) 514 mTorr and (d) 573 mTorr.	48
Figure 3.10 L ₁₀ FePt nanoparticles fabricated at different discharge current: (a) 0.6 A, (b) 0.8 A, (c) 0.9 A and (d) 1.0 A.....	51
Figure 3.11 Energy (thermal environment) requirements for the formation of L ₁₀ FePt nanoparticles in gas phase.....	55
Figure 3.12 Experimental factors for the simultaneously control of the phase and size of L ₁₀ FePt nanoparticles.	57
Figure 3.13 (a) Size control of L ₁₀ FePt nanoparticles. (b) TEM bright field images, TEM diffraction patterns and magnetic hysteresis loops of L ₁₀ FePt nanoparticles with sizes of 6nm, 12 nm and 17nm.	59
Figure 3.14 Three different morphologies of 12 nm L ₁₀ FePt nanoparticles observed by HRTEM	61
Figure 3.15 Substrate configuration for co-deposition of nanoparticles (NP) and matrix materials.....	64
Figure 4.1 Schematic one-dimensional model of exchange-spring magnet ⁷ ..	74

Figure 4.2 Hysteresis loops of 1D exchange-spring magnets with different exchange coupling strength.....	79
Figure 4.3 Two basic structures of exchange-spring magnets: (a) multilayer structure, (b) nanocomposite structure.....	82
Figure 4.4 Simple cubic arrangements of hard phase particles in matrix.....	82
Figure 4.5 Schematic drawing for (a) anisotropic exchange-spring magnet and (b) isotropic exchange-spring magnet.....	84
Figure 5.1 (a) Anisotropic exchange-spring nanocomposites fabrication system, (b) illustration of the easy-axis field alignment process.....	96
Figure 5.2. (a) dominated shape of 5.8 nm $L1_0$ FePt nanoparticles and (b) its schematic drawing. (c) The magnetic hysteresis loop of 5.8 nm $L1_0$ FePt nanoparticles.	99
Figure 5.3 cross section TEM image of the FePt/Fe-Ni anisotropic nanocomposites.....	100
Figure 5.4. XRD pattern of the FePt/Fe-Ni anisotropic nanocomposites. (SiO ₂ peaks, labeled with small squares, from left to right are SiO ₂ (220), (310), (330) and (331)).	101
Figure 5.5 Schematic drawing of (a) 3D view FePt/Fe-Ni anisotropic exchange-spring magnets, (b) cross section view of XY plane and (c) cross-section view of YZ plane.....	102
Figure 5.6 (a) YZ plane cross-section HRTEM picture of the FePt/Fe-Ni anisotropic nanocomposites and (b) its corresponding diffraction pattern. (c) XY plane cross-section view HRTEM picture of the FePt/Fe-Ni anisotropic nanocomposites and (d) its corresponding diffraction pattern.....	104

Figure 5.7 Magnetic properties of (a) anisotropic FePt/Fe-Ni nanocomposite, (b) FePt/Fe exchange decoupled nanocomposite.....	106
Figure 5.8 Distribution of (a) H_{sw} and (b) H_{swr}	108
Figure 5.9 (a) Recoil loops and δ M-H curve of FePt/Fe-Ni anisotropic nanocomposites.....	109
Figure 5.10 Hysteresis loops of anisotropic and isotropic FePt/Fe-Ni exchange-spring magnets.....	110
Figure 5.11 Coercivity (H_c), saturation magnetization (M_s) and magnetization remanence (M_r) as functions of $L1_0$ FePt volume ratio in the FePt/Fe-Ni anisotropic exchange-spring nanocomposites.....	112
Figure 5.12 Energy product $(BH)_{max}$ as a function of $L1_0$ FePt volume ratio in the FePt/Fe-Ni anisotropic exchange-spring nanocomposites. Exchange-spring magnets using $L1_0$ FePt nanoparticles with different ordering parameters, 85% are labeled with square marks and 70% are labeled with star mark..	114
.	
Appendix A:	
Fig. 1 Crystalline structure of (a) $Fe_{16}N_2$ and (b) Fe_8N (white-Fe; grey-N), (For Fe_8N , N atoms randomly distribute at all the possible N sites and keep N-Fe atom ratio at 1:8); Crystalline environment of (c) Fe-4e; (d) Fe-8h; (e) Fe-4d.	141
Fig. 2 XRD spectra of (a) sample A with single Fe_8N phase and (b) sample B with $Fe_8N+Fe_{16}N_2$ phases.....	142
Fig. 3 XAS and XMCD spectra of (A) sample A, (B) sample B, (C) delocalized Fe 3d state in bulk iron [25] and (D) localized Fe 3d ⁷ state [29]..	144
Fig. 4 Hysteresis loops recorded for N atoms at K-edge 399 eV and Fe atoms at L_3 edge 707eV on (a) sample A and (b) sample B.....	148

Appendix B:

Figure 1. (Color online) Directly ordered $L1_0$ FePt nanoparticles prepared using a gas-phase aggregation technique at room temperature. (Ref [15]) (a) TEM micrograph of particles showing the uniform size distribution (b) HRTEM image of one chemically ordered particle with its c-axis (the magnetic easy axis) lying in-plane (c) A 3-D atomic reconstruction of the $L1_0$ FePt particle shown in (b). It has a length of 6.7 nm along the [001] axis. (d) Schematic drawing of the eight equivalent $\{111\}$ planes in (c). 156

Figure 2. Reversal magnetization loops for (a) non-embedded 5.8nm $L1_0$ FePt nanoparticles (b) 5.8nm $L1_0$ FePt nanoparticles embedded in soft FePt matrix and (c) non-embedded 12nm $L1_0$ FePt nanoparticles, measured at 5 Kelvin. In (a) the solid line stands for a normal hysteresis loop including the signal contribution from both hard and soft phases, the dashed partial curve is a DC demagnetization remanence curve counting only the irreversible contribution. 158

Figure 3. DCD remanence curves of 5.8nm $L1_0$ FePt nanoparticles as a function of measurement temperature. Figure (b) is a zoom-in of the kink area showing in figure (a) at low fields. 160

Figure 4. Comparison between moments switched at reversal fields of -2000 Oe and -20000 Oe (5.8nm $L1_0$ FePt nanoparticles). Up to -2000 Oe there are about 16 % of all the moments switched and the switching is independent of temperature. Around -20000 Oe the percentage of switched moments is a function of temperature. 161

Figure 5. (Color online) (a) The chemical environment of a surface platinum atom (blue color) in the octahedral $L1_0$ phase FePt nanoparticle. Four of the six iron atoms are on the surface (white color) and the other two are interior (orange color). (b) The remanence state of one octahedral $L1_0$ FePt nanoparticles with transverse surface anisotropy. Here arrows represent the moments from iron atoms and all platinum atoms have been omitted for clarity. Red arrows are surface moments and black arrows are interior moments, respectively. (c) 3D micro-magnetic simulated hysteresis loop of 5.8 nm $L1_0$ FePt nanoparticles using the model described in Fig. 5 (a) and (b), compared to experimental measurement..... 164

Appendix C.1:

Figure 1. XRD pattern of Ta(3nm)/Sm₁₄Co₅₈Cu₂₈(10nm)/Ru(4nm)/Ru(16nm)/Ta(4.2nm)/glass. The inset shows its magnetic hysteresis loops in out-of-plane (black dots) and in-plane (white dots) directions..... 173

Figure 2 (a) Magnetic hysteresis loops in the perpendicular direction and (b) XRD patterns of samples with different Sm-Co-Cu compositions. (XRD results from top to bottom represent sample with composition: Sm₁₄Co₅₈Cu₁₈, Sm₁₆Co₆₃Cu₂₁, Sm₁₆Co₇₃Cu₁₁, and Sm₁₇Co₈₃.)..... 175

Figure 3 (a) Magnetic hysteresis loops and (b) XRD patterns of Sm₁₄Co₅₈Cu₂₈. (XRD results from top to bottom represent sample with deposition temperature: 350°C, 250°C, and 150°C.) 176

Figure 4 Magnetic hysteresis loops in the out-of-plane direction of Sm₁₄Co₅₈Cu₁₈ films on pure Ru (0002) underlayer with different thicknesses. 178

Appendix C.2:

Figure 1 (a) XRD patterns and (b) Magnetic hysteresis loops in the out-of-plane direction of Sm-Co-Cu (20nm) films on Ru(Cr)(10nm)/Ru(10nm) underlayer with different Ru-Cr compositions. 187

Figure 2 (a) Magnetic hysteresis loops, (b) XRD and (c) TEM image of Ta(3nm)/Sm-Co-Cu(10nm)/Ru(4nm)/Ru(16nm)/Ta(4.2nm)/glass. 189

Figure 3 RBS spectra for Sm-Co-Cu films with structure Ta(3nm)/Sm-Co-Cu(10nm)/Ru(4nm)/Ru(16nm)/Ta(4.2nm)/glass. 192

Figure 4 Angle dependence of (a) coercivity H_c and (b) remanence coercivity H_{cr} of Sm-Co-Cu film with structure Ta(3nm)/Sm-Co-Cu(10nm)/Ru(4nm)/Ru(16nm)/Ta(4.2nm)/glass (angles respect to the out-of-plane direction). 193

CHAPTER 1

INTRODUCTION

1.1 Materials science developed into nanoscale

After hundreds of years' study, the objects of modern magnetic physics have developed from the macro magnetic properties of magnetic materials to the micro behaviors of basic particles such as electrons, ions, etc. The study of basic particles directly leads to the basic understanding of magnetism in solid state materials, since the intrinsic properties of magnetic materials such as magnetization and crystalline anisotropy are determined by the basic particles in atomic scale.

Accordingly, nano-structured magnetic materials attract a great deal of attention. Not only because studies on nano-structured magnetic materials help our understanding of magnetism but also because these nano-structured magnetic materials show unique and unachievable properties, compared to conventional magnetic materials.

For materials science, the development of nano-structured materials opens the door to new technologies. Nano-structured magnetic materials can be engineered to achieve different properties. Therefore the performance improvement of current magnetic materials heavily relies on nano-structured materials engineering.

1.2 Magnetic nanocomposite materials and their applications

Magnetic nanocomposite materials are defined as composite materials with two or more different magnetic materials (phases), and relatively strong magnetic interaction existing between the different materials (phases). Magnetic nanocomposite materials are usually in the form of magnetic nanoparticles or granular materials embedded in a magnetic or a non-magnetic matrix.

Nowadays, magnetic nanocomposite materials are extremely widely used in magnetic recording systems, permanent magnets, nanocrystalline magnetic soft materials, biomedical materials and devices, etc. In this thesis work, studies on gas phase synthesis of magnetic nanocomposite materials are performed. A novel gas phase synthesis process has been developed for nanocomposite fabrication. This technique represents a general process and is applicable to various materials. Anisotropic exchange-spring magnet with nanocomposite structure has been successfully fabricated for the first time, based on a FePt/Fe-Ni system, by using this novel nanocomposite fabrication process.

1.3 Outline of the thesis

The Chapters of this thesis are organized as the following:

Chapter 2 first introduces most of the conventional synthesis methods of magnetic nanostructured materials. Then it focuses on the gas-phase synthesis methods, and discusses the thermodynamic of magnetic nanoparticle formation in gas phase.

Chapter 3 is the detailed study of our novel gas-phase magnetic nanocomposites synthesis process. FePt alloy is chosen to demonstrate how the chemical ordering and the particle size of nanostructured materials can be controlled in our nanocomposites fabrication system. Matrix materials fabrication and easy-axis control of the magnetic nanocomposites are also included in this chapter.

Chapter 4 introduces the background and basic idea of exchange-spring magnets and its advantages. Theoretical models of exchange-spring magnets are discussed. Then the advantage and disadvantages of two basic structures of exchange-spring magnets are discussed and compared. At last, the mechanism of how the anisotropic-exchange-spring magnets generate higher energy product compared to isotropic exchange-spring magnets is explained.

Chapter 5 performs a systematical study of the gas-phase fabricated anisotropic-exchange-spring FePt/Fe-Ni magnets. The study includes the

characterization of crystal structure, magnetic properties and the volume effects of $L1_0$ FePt hard phase.

Chapter 6 first summarizes the work on the gas-phase synthesis of magnetic nanocomposites, and the anisotropic exchange-spring magnets. Then it gives the future directions and outlooks of this gas-phase synthesis technique and anisotropic exchange-spring magnets.

CHAPTER 2

SYNTHESIS METHODS OF MAGNETIC NANO-STRUCTURED MATERIALS

2.1 Introduction to synthesis methods of magnetic nanostructured materials

Magnetic nano-structured materials are defined as magnetic materials, including alloy, compounds and composites, that have or their components have nanometer sized structures in one or more dimensions¹. Based on the dimensions, magnetic nano-structured materials can be classified into three types:

1. Zero dimension nano-structured magnetic materials, which have nanometer sized structure in three dimensions, such as magnetic nanoparticles.
2. One dimension nano-structured magnetic materials, which have nanometer sized structure in two dimensions, such as magnetic nanowires.
3. Two dimension nano-structured magnetic materials, which have nanometer

sized structure in one dimension, such as magnetic thin films or super lattices.

After over several decades' study, many synthesis methods of magnetic nano-structured materials have been developed. Basically, most of the synthesis methods can be classified into two categories: physical and chemical processes.

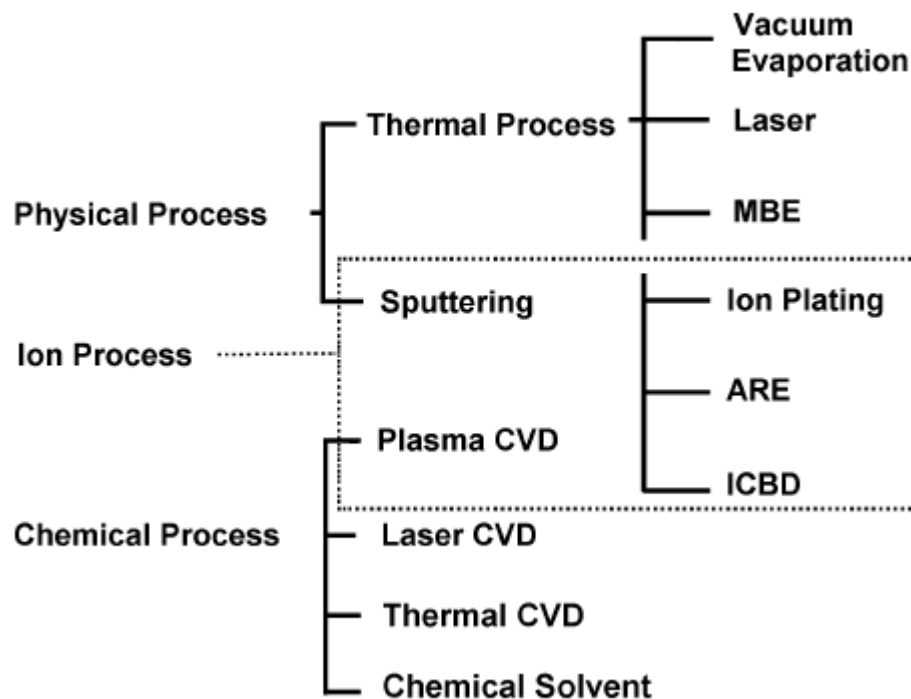


Figure 2.1 Synthesis methods of magnetic nano-structured materials².

As shown in Figure 2.1, the physical process, which also called physical vapor deposition process (PVD), consists of two categories, one is thermal evaporation process and the other is sputtering process. The thermal process includes vacuum evaporation, laser evaporation, molecular beam epitaxy (MBE), ion plating,

activated reactive evaporation (ARE), and ionized cluster beam deposition (ICBD).

The chemical process also consists of two categories, one is chemical vapor deposition (CVD) process and the other is chemical solvent process. The CVD processes include plasma CVD, laser CVD and thermal CVD processes.

2.2 Physical vapor deposition (PVD) process

2.2.1 Thermal evaporation process

For the first category of PVD process, thermal evaporation, the basic working principle is: in a vacuum chamber, thermally evaporate the source materials by a heating source such as resistive heating or electron beam heating, and then condense the evaporated atoms or clusters of source materials on a substrate. The schematic drawings of two typical thermal evaporation systems are shown in Figure 2.2.

Resistive heating source is most often used in thermal evaporation process. However resistive heating can't be used for source materials with high melting temperature. Instead electron beam heating source can reach sufficient high temperature for evaporating most of the materials.

Laser deposition, also called pulsed laser deposition (PLD), is another thermal evaporation process, which uses a high-power pulsed laser to ablate the source materials. Besides thermal effect, the pulsed laser can also cause plasma formed on the surface of target materials. Therefore PLD includes both of thermal evaporation process and plasma sputtering process. The plasma process will be discussed later in this chapter.

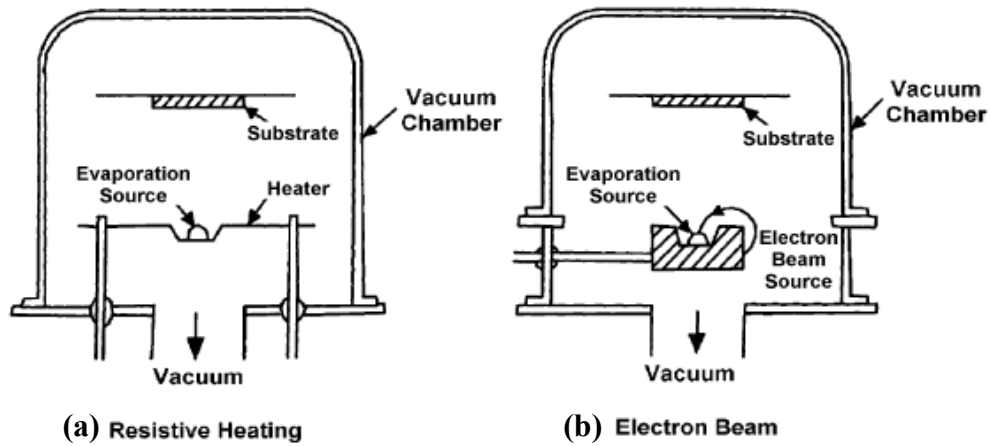


Figure 2.2 Two typical thermal evaporation systems using (a) resistive heating source and (b) electron beam heating source, respectively¹.

Molecular beam epitaxy (MBE) deposition process is considered as the most reliable process in thermal evaporation process. Since the evaporation rate of each source material is accurately controlled by an in situ computer control unit. Extremely thin film, down to single atomic layer, can be deposited by MBE process. Figure 2.3 shows a schematic drawing of a typical MBE deposition system. Right now, MBE process is widely used for various materials, especially semiconductor and superconductor materials.

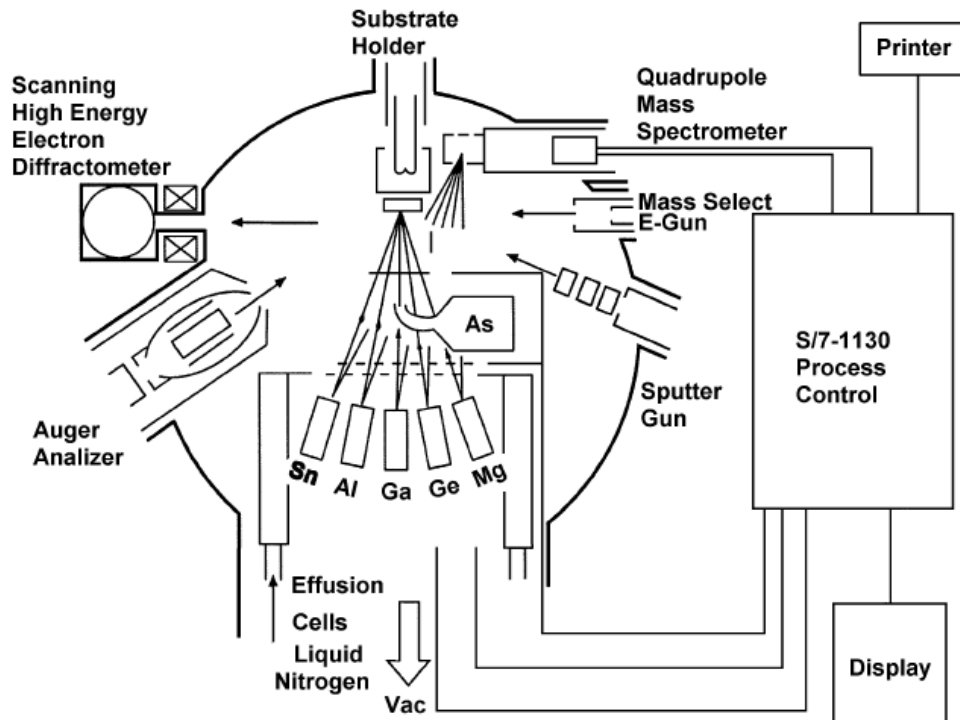


Figure 2.3 Molecular beam epitaxy deposition system³.

Ion plating is another thermal evaporation process that involves plasma.

The basic process is: in a conventional thermal evaporation vacuum chamber, insert a plasma area between the material source and substrate, and apply a voltage on the substrate. The evaporated atoms or atom clusters are negatively charged, then accelerated by the electrical field, finally reach the substrate. Through the electrical field acceleration, material adhesion on the substrate is improved.

Activated reactive evaporation (ARE) is similar to ion plating, the difference is instead of a plasma, ARE injects reactive gas into to region between the materials source and substrate to make the source material react with the reactive gas.

Ionized cluster beam deposition (ICBD) is also similar to ion plating process. The difference is that before the evaporated atoms moving to the plasma area, ICBD make the evaporated atoms form clusters by cooling the atoms. Thus the atom clusters instead of atoms, reach the substrate.

2.2.2 Sputtering process

Sputtering process is one of the most important PVD deposition processes of nano-structured material fabrication. Figure 2.4 shows (a) a schematic drawing of sputtering system (b) sputtering process on target surface.

The basic idea is: In a sputtering chamber, as shown in figure 2.4 (a) the target (source materials) is connected to a DC power supply and the vacuum chamber is grounded. Sputtering gas, usually argon (Ar) gas is injected into the chamber. Due to the strong electrical field, plasma can be formed on the surface of the target. Plasma consists of Ar^+ ions and electrons e^- . Therefore, a continuous glow discharge current is formed between the target and grounded chamber. Ar^+ ions are accelerated by electrical field and the target is bombarded by these energetic Ar^+ ions. Target atoms are scattered out of the target surface, as shown in figure 2.4 (b).

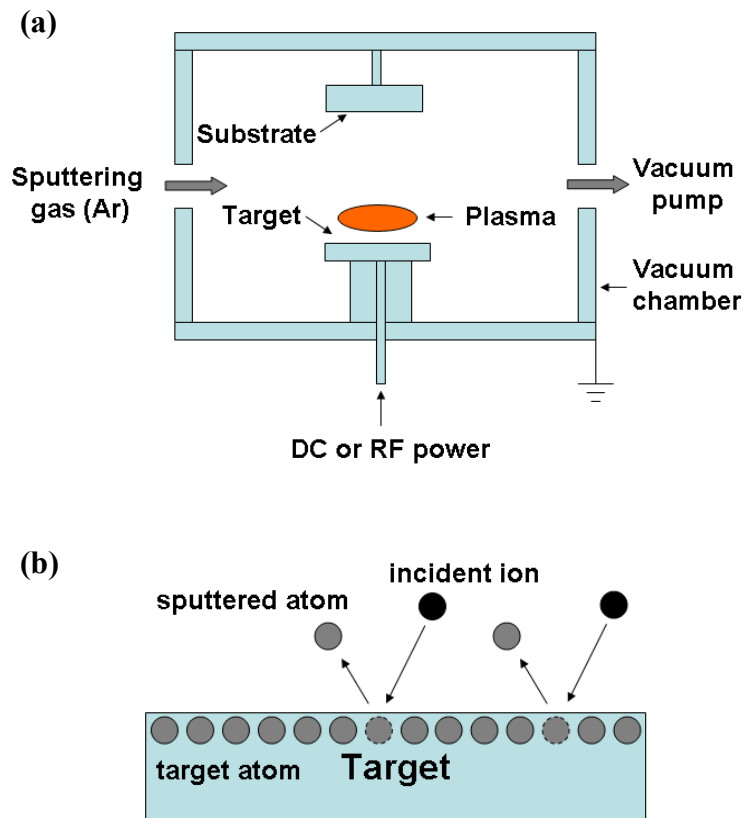


Figure 2.4 (a) schematic drawing of a sputtering system (b) sputtering process on target surface.

To maintain and enhance the plasma density, magnets are applied under the target. The sputtering process therefore is called magnetron sputtering. For non-metal targets, RF power can be used. This sputtering process is called RF sputtering. Reactive gas can also be added to the sputtering gas to change the material composition on the substrate. This sputtering process is called reactive sputtering. The physics of plasma and technical considerations of sputtering process will be discussed in detail in following sections.

2.3 Chemical vapor deposition (CVD) process

In chemical vapor deposition (CVD) process, the source materials are first vaporized and decomposed into atoms or molecules, and then react with other vapors, gases or liquids, and finally yield reaction product on the substrate¹.

Based on the use of different methods of enhancing the chemical reaction, CVD process can be classified into plasma assisted CVD, laser assisted CVD, and thermal assisted CVD. The introducing of plasma, laser or thermal effect into CVD process helps break the chemical bond and activate the chemical reaction.

2.4 Thermodynamics in the formation of nanoparticle in gas phase

Among all the synthesis methods of nano-structured materials, gas-phase synthesis process is one of the most important methods for both large scale production and fundamental research⁴. Since gas-phase synthesis process not only is able to produce large quantities of nanoparticles but also has high level of control on particle properties, such as size, shape, phase etc.

In this section, thermodynamics of the formation of nanoparticle in gas phase, including the nucleation and growth process will be studied in detail.

2.4.1 Nucleation mechanism of nanoparticle in gas phase

Although for the sputtering-based gas phase synthesis process, the nanoparticle or nanocluster formation mechanism is very complicated due to the presence of plasma, the non-uniformity of magnetic field, and the non-uniformity of gas pressure and gas flow in the vacuum chamber, we can still use classical thermodynamics⁵ to get a basic understanding of the nanoparticle nucleation and growth process in gas phase.

In fact the gas phase condensation process is a commonly seen phenomenon in nature, such as the formation of rain or snow.

The basic process is: First a vapor of source materials is generated through various evaporation processes. When the vapor pressure exceeds the super-saturation limit, small nuclei begin to form in the vapor gas. This nuclei formation process can be either heterogeneous if there are already some nucleation seeds existing in the vapor or homogeneous if there is no nucleation seeds existing in the vapor. After the formation, nuclei will grow into bigger particles through either surface growth or agglomeration, which depends on the vapor conditions and nuclei density etc.

For the gas phase synthesis of nano-structured materials, the whole process happens in a high vacuum chamber (base pressure of $10^{-7} \sim 10^{-9}$ Torr), therefore the homogeneous process is preferred. For a thermodynamic process, everything is determined by the Gibbs free energy [5].

$$dG = Vdp - sdT \quad (2.1)$$

Here G is the Gibbs free energy, V is specific volume, p is pressure, s is the specific entropy, and T is temperature.

In a vapor, integrate dG along the meta stable isotherm from saturation pressure p' to the supersaturated pressure p at temperature T , the excess of specific Gibbs free energy can be obtained in the form of:

$$\Delta G = RT \ln p/p' \quad (2.2)$$

Here R is the ideal gas constant. For a nucleus, the Gibbs free energy will be:

$$\Delta G = -\frac{4}{3}\pi r^3 \rho RT \ln S + 4\pi r^2 \sigma \quad (2.3)$$

Here r , ρ and σ are nucleus radius, density and surface free energy, respectively. The

$S=p/p'$ is defined as the super saturation ratio. The first term in equation (2.3) is bulk Gibbs free energy derived from equation (2.2). The second term is surface Gibbs free energy.

As shown in equation 2.3, the super saturation ratio S must be larger than 1. If $S < 1$, then $\Delta G > 0$, which means the formation of nuclei is not favorable to minimize the ΔG Gibbs free energy. Therefore $S > 1$ is a pre-required condition for the nucleus to form in a vapor.

Because ΔG Gibbs free energy is a function of nucleus radius r , we can use equation (2.3) to derive a critical value for nucleus radius r :

$$r_c = \frac{3\sigma}{\rho RT \ln S} \quad (2.4)$$

Therefore the critical value for ΔG Gibbs free energy is:

$$\Delta G_c = \frac{16\pi\sigma^3}{3(\rho RT \ln S)^2} \quad (2.5)$$

When $r = r_c$, ΔG_c reaches its maximum value. When $r < r_c$, $d\Delta G_c/dr > 0$, which means ΔG_c increases with r_c . When $r > r_c$, $d\Delta G_c/dr < 0$, which means ΔG_c decreases with r_c . Therefore if the formed nucleus radius is smaller than its critical value r_c , the nucleus will decrease its size to minimize ΔG Gibbs free energy. Eventually the nucleus will vanish. If the formed nucleus radius is larger than its critical value r_c , the nucleus will increase its size to minimize ΔG Gibbs free energy. So only the nucleus with radius larger than its critical value will keep growing.

2.4.2 Growth mechanism of nanoparticle in gas phase

In previous section, the gas-phase nanoparticle nucleation mechanism is discussed. In this section, two basic particle growth mechanisms, surface growth and agglomeration, will be studied.

For surface growth mechanism, particles keep growing through absorbing atoms from the atom vapor and adding atoms to the particle surface. Therefore surface growth is a homogenous process. The growth rate is expressed as⁶:

$$\dot{N} = [n_s \exp(-\Delta G_c / K_B T)] 4\pi r_c^2 \left[\frac{\alpha (P_v - P_s) N_A}{\sqrt{2\pi MRT}} \right] \quad (2.6)$$

where n_s is the available nucleation site (number of atoms in gas phase), ΔG_c is the change of Gibbs free energy for a nucleus with the critical size, $4\pi r_c^2$ is surface area of a nucleus with a critical radius r_c , α is the sticking coefficient (number of sticking atoms/number of impinging atoms), P_v is the vapor pressure of the supersaturated vapor, P_s is the vapor pressure on the nucleus surface, N_A is the Avogadro's number and M is the atomic weight.

From equation (2.5) and (2.6), the main factors that influence the particle surface growth rate are:

1. n_s , the available nucleation site (or the number of atoms in gas phase). The growth rate is proportional to the density of available atoms in the vapor.

2. Supersaturation ratio S . The growth rate is higher with higher supersaturation

ratio.

3. T , the temperature. The surface growth rate decreases following the increase of temperature. At higher temperature, atoms in the vapor possess higher energy and it is harder for them to be absorbed by nuclei. The vapor also has higher supersaturation pressure at higher temperature which leads to smaller supersaturation ratio S .

For the particle agglomeration or particle coalescence mechanism, particle grows through the merging of more nuclei. In gas phase, all nuclei are not stationary, rather moving in a random manner (Brownian motion). Therefore in a vapor with a high concentration of nuclei, the probability of the collision among nuclei is very high. Nuclei can quickly increase their size by merging with more nuclei.

Growth mechanism has great influences on the properties of the particle formed. For surface growth mechanism, particles usually have a smaller size, narrower size distribution, and better crystallinity. For agglomeration or coalescence mechanism, particles usually have relatively larger size and wider size distribution. The particles formed usually have polycrystalline structure and the crystallinity is relatively lower. The reason is that through surface growth, particle size growth rate is relatively lower. So atoms have enough energy and time to self-organize on the particle surface to seek a low energy state, which will lead to a good crystalline structure automatically.

Which mechanism dominates in the particle growth process is determined by

the vapor supersaturation ratio. High vapor supersaturation ratio causes both high nucleation rate and high nuclei concentration in the vapor⁷. Therefore the agglomeration or coalescence mechanism will dominate the particle growth process. Contradictorily, at low vapor supersaturation ratio, the surface growth mechanism dominates.

One thing needs to be mentioned is that the vapor supersaturation ratio is directly related to the vapor temperature. The vapor saturation pressure is proportional to the temperature for most materials. With the same vapor pressure, vapor supersaturation ratio is higher at low temperature and lower at high temperature. Therefore for the vapor of certain material with certain pressure, the agglomeration or coalescence mechanism is dominated at low temperature and surface growth mechanism is dominated at high temperature.

2.4.3 Cooling processes to generating supersaturated vapor

As mentioned in above section, the vapor saturation pressure inversely depends on the temperature. Therefore a vapor cooling process will effectively generate supersaturated vapor.

Basically there are two ways of cooling the vapors:

1. The first one is inputting inert gas to cool the vaporized atoms through collision in which energy is transferred from energized vapor atoms to low energy

inert gas atoms.

2. The second method is suddenly expanding the vapor volume to cool down the vaporized atoms which is also called supersonic jet expansion.

The sudden volume expansion in the second method introduces a very fast particle nucleation and growth process, which is favorable for a large quantity of the fabrication of nanoparticles. However, the second method has a poor control of the particle nucleation and growth process compared to the first method due to the time issue.

2.5 Sputtering based gas-phase synthesis process

Gas-phase synthesis process has been studied for a long time^{8, 9} with a big concern on the nanoparticle yield issues. Harberland et al¹⁰ developed a gas phase nanocluster synthesis system using a magnetron sputtering gun to generate materials vapors and achieved relatively high particle yield. However, their method is very limited in controlling the phase and size of the nanoparticles. Thereafter, a lot of research work has been done on magnetic nano-structured materials using gas phase deposition process¹¹.

Figure 2.5 shows the gas phase nanocluster synthesis system developed by Harberland et al [10b]. The basic working principle of this system is: A magnetron sputtering gun is allocated into a high gas pressure chamber to generate supersaturated vapor of target atoms. The gas pressure is controlled by the control the input inert gas (Ar) in this sputtering chamber. The vaporized target atoms are cooled by Ar atoms and start the nanocluster nucleation and growth process. Vacuum pumps are connected to the substrate chamber. Therefore formed nanoclusters are then carried by Ar gas flow through vent-hole B1 and B2 and reach the substrates.

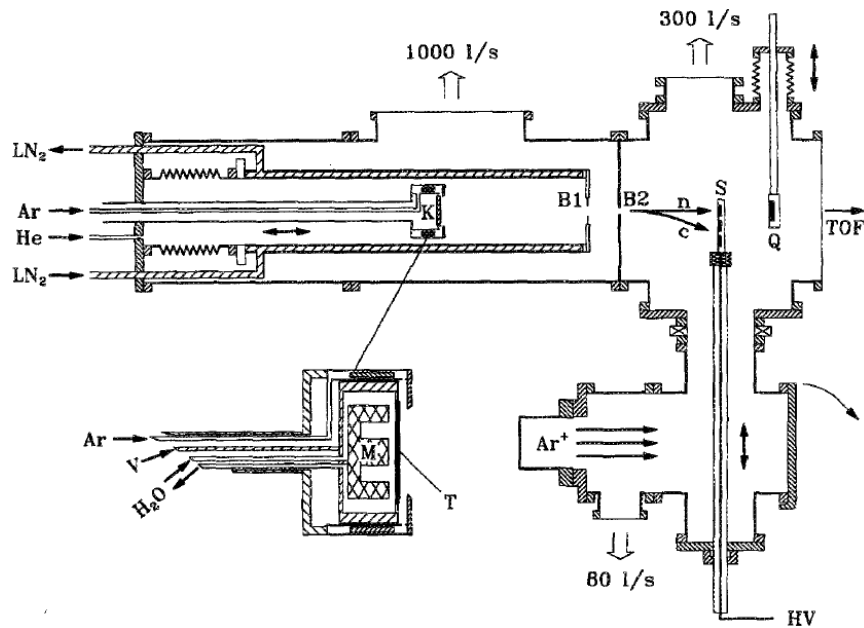


Figure 2.5 Configuration of a sputtering based gas-phase nanoparticle synthesis system^{10b}. K is a magnetron sputtering gun used for atom vapor generation. S is the substrate holder. Nanoclusters were formed under high pressure inert gas and swept out by carrier gas through vent-hole B1 and B2.

The system built by Harberland et al is based on a sputtering process. However, in the sputtering process, the plasma area is very narrow and non-uniform. The thermal environment of the nanoparticles growth process is under very limited control. Therefore their method is very limited in controlling the phase and size of the nanoparticles.

2.6 Summary

In this chapter, most of the common synthesis methods of nano-structured materials are reviewed. The thermodynamics in formation of nanoparticles in gas phase is studied in detail. At last, conventional sputtering based gas phase synthesis process is introduced, including its limits.

Reference:

-
- ¹ Kiyotaka Wasa, Makoto Kitabatake and Hideaki Adachi
Thin film materials technology: sputtering of compound materials, Publisher William Andrew, New York (2004)
- ² Bunshah, R. F., (ed.), Deposition Technologies for Films and Coatings, Noyes Publications, NJ, (1982); Mattox, D. M., Handbook of Physical Vapor Deposition Processing, Noyes Publications, NJ (1998); Mahan, J. E., Physical Vapor Deposition of Thin Films, John Wiley & Sons, New York (2000); Elshabini-Riad, A., and Barlow, F. D., III, (ed.), Thin Film Technology Handbook, McGraw-Hill, New York (1997)
- ³ Esaki, L., Proc. 6th Int. Vacuum Congr., Kyoto, *Jpn. J. Appl. Phys.*, 13:Suppl. 2(Pt. 1):821–828 (1974)
- ⁴ Stark W J and Pratsinis S E, *Powder Technol.* 126, 103–8 (2002)
- ⁵ a) J. E. McDonald, *American Journal of Physics*, 30, 870, 1962; b) J. E. McDonald, *American Journal of Physics*, 31, 31, 1963
- ⁶ M. Ohring, The materials science of thin films: deposition and structure, 2nd ed. (Academic Press, San Diego, CA, 2002).
- ⁷ K. H. Lieser, *Angew. Chem. Internat. Ed.* 8, 188, 1969
- ⁸ C. G. Granqvist and R. A. Buhrman, *J. Appl. Phys.* 47(5), 2200, 1976
- ⁹ K. Sattler, J. Muhlbach and E. Recknagel, *Phys. Rev. Lett.* 45, 821 (1980).
- ¹⁰ a) H. Haberland, M. Karrais, M. Mall, and Y. Thurner, *J. Vac. Sci. Tech.* A10, 3266, 1992; b) H. Haberland, M. Mall, M. Moseler, Y. Qiang, T. Reiners, and Y. Thurner, *J. Vac. Sci. Tech.* A12, 2925, 1994

- ¹¹ C. Binns, K. N. Trohidou, J. Bansmann, S. H. Baker, J. A. Blackman, J-P Bucher, D. Kechrakos, A. Kleibert, S. Louch, K-H Meiwes-Broer, G. M. Pastor, A. Perez, and Y. Xie, *J. Phys. D: Appl. Phys.* 38, R357, 2005

CHAPTER 3

GAS PHASE SYNTHESIS OF MAGNETIC NANOCOMPOSITE MATERIALS

3.1 Introduction

Nanostructured magnetic materials have extremely wide applications, such as magnetic recording media^{1, 2}, spin electronics^{3, 4}, magnetoresistive sensor^{5, 6}, future quantum computing^{7, 8}, etc. However, nearly all of these applications have very strict requirements on the properties of nanostructured magnetic materials. The properties of nanostructured magnetic materials depend on the properties of the nanoclusters or nanoparticles inside the nanostructured magnetic materials. Therefore a precise control of the properties of the nanoclusters or nanoparticles, such as phase, size, and size distribution etc, is required.

Although the synthesis of nanoparticles by gas-condensation has been

demonstrated by Granqvist and Buhrman as early as in the 1970s⁹ and a lot of research have been performed^{10, 11}, the direct precise control of the nanoparticle formation in gas phase was still unable to achieve. The post-formation processes, such as post-annealing and on-line heating, were also studied to control the properties of the nanoparticles, but these processes introduced new problems such as particle agglomeration and crystalline structure twinning^{12,13,14,15}.

In this chapter, we will introduce our novel gas phase synthesis process, and perform a systematical study on how the properties of nanoparticles (nanoclusters) such as phase and size are controlled by precisely controlling the energy environment of the nanoparticle formation. The fabrication of nanoparticles (nanoclusters) is the most important part of any kinds of nano-structured materials including the nanocomposite materials. Thereafter, matrix fabrication and orientation control of the magnetic nanocomposites on the substrate will be discussed.

3.2 A novel gas phase synthesis process

3.2.1 System setup

The schematic drawing of a typical deposition system of our novel gas phase magnetic nanocomposite materials synthesis process is shown in Figure 3.1. The deposition system consists of a magnetron sputtering based gas phase nanoparticle deposition source and a conventional thin film sputtering gun. The gas phase nanoparticle deposition source is located on the left hand side and the matrix sputtering gun is installed in the substrate chamber on the right hand side. The nanoparticle deposition source points directly to the substrate while the matrix sputtering gun is located about 30 degree relative to the out-of-plane direction of the substrate plane.

The two chambers where gas phase nanoparticle deposition source and the matrix sputtering gun are located are named as source chamber and deposition chamber, respectively. These two chambers are connected through one or two apertures, which are used to control the gas pressure in the two chambers separately and used to control the dependence of the gas pressure on gas flow rate in the source chamber. Both chambers are equipped with a two stage pumping system, which includes mechanical pumps and cryo pumps. The base pressure of system is 4×10^{-8}

Torr. During the material deposition process, only the cryo pump at the rear of deposition chamber is pumping, to control the gas flow path from source chamber to deposition chamber.

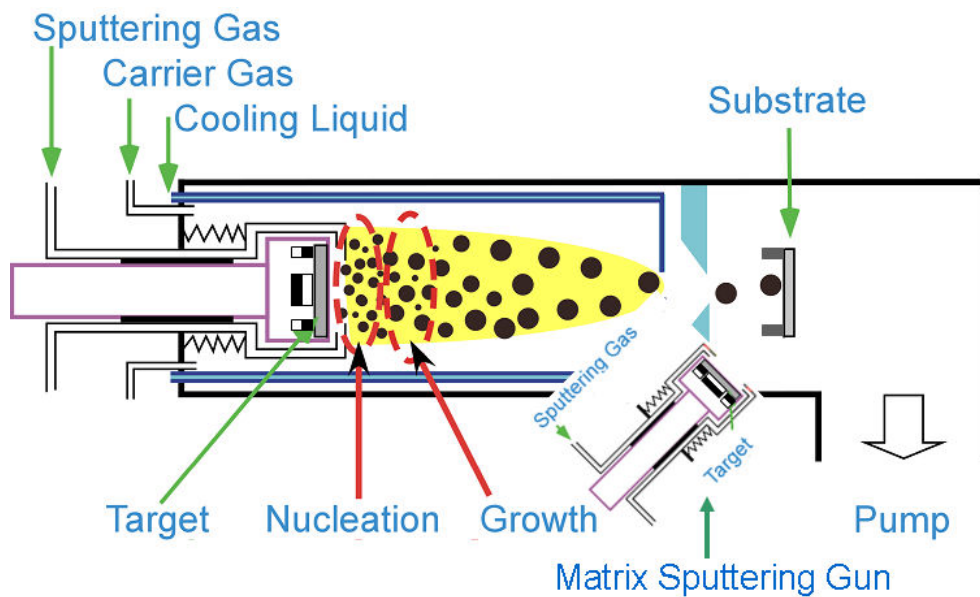


Figure 3.1 Schematic drawing of the novel gas phase synthesis system.

Both the nanoparticle deposition source and matrix sputtering gun are working in direct current (DC) mode. But RF mode can also be used if necessary. Both the carrier gas and sputtering gas are argon (Ar) gas. Sputtering targets are cooled by cooling waters. In following sections, we will first study the working principles of the nanoparticle deposition source, and then investigate the matrix fabrication.

3.2.2 Introduction of FePt alloy

For the deposition of nanocomposite materials using our novel gas phase synthesis system, the nanocluster (nanoparticle) deposition source is the key component. The nanocluster (nanoparticle) deposition source controls the properties of nanoparticles embedded in the nanocomposite materials, which dominates the whole properties of nanocomposite materials. So in following sections, we will emphasize the nanoparticle synthesis process. The most important discoveries and new physics in our study also lie on the nanoparticle synthesis process.

To demonstrate the advantages of our novel synthesis process on precisely controlling every stage in nanoparticle formation process, FePt alloy is chosen as the target material.

The reason is FePt nanoparticles not only form a good research platform for fundamental materials science and physics in nanoscale^{16,17,18,19}, but also from the technological perspective, chemically ordered L1₀ FePt nanoparticles are future candidates of extremely high areal density magnetic recording media^{20,21,22}. Conventional fabrication methods normally can only generate A1 phase FePt nanoparticles and a solid state phase transformation from A1 to L1₀ phase (usually a post-annealing process) is inevitable^{21, 23}. The post-annealing process causes serious problems, such as nanoparticle agglomeration and size distribution broadening²⁴,

which are not favored by both fundamental physics studies and magnetic recording application. But in our recently developed gas phase synthesis method, FePt nanoparticles are directly ordered in gas phase^{25,26} and open for magnetic orientation tuning²⁷. Furthermore, since the nucleation, growth and chemical ordering of L1₀ FePt nanoparticles are all completed in gas phase, the morphology, crystallinity and chemical ordering of FePt nanoparticles are directly related to the intrinsic energy balance during the formation of nanoparticles. This makes it possible to understand the underline physics of nanoparticle growth²⁸, size dependence of nanoparticle morphology^{17, 18} and atomic arrangements on nanoparticle surface¹⁹.

For near equiatomic FePt alloy, the binary phase diagram shows that FePt have two phases, one is the A1 (FCC) phase which is stable at temperatures above 1300°C, the other is the L1₀ (FCT) phase which is thermodynamically stable under 1300°C. The crystalline structures for A1 and L1₀ phase FePt alloy are shown in Figure 3.2 (a) and (b), respectively. For A1 phase, Fe and Pt atoms are completely randomly distributed in the fcc lattice, forming a chemically disordered phase. However for L1₀ phase, Fe and Pt atoms are chemically ordered and form a chemical ordered fct lattice with alternative Fe and Pt atom layers. Because the special crystalline structure, L1₀ phase FePt possesses very high magnetocrystalline anisotropy energy (MAE) ($\sim 7 \times 10^7$ ergs/cm³)²⁹. The magnetocrystalline anisotropy energy comes from the polarization of Pt atoms due to the hybridization between Pt 5d and Fe 3d

states, and the strong spin-orbit coupling in 5d electrons of Pt^{30} . Contradictorily, because of the lack of chemical ordering, A1 phase loses the high magnetocrystalline anisotropy energy.

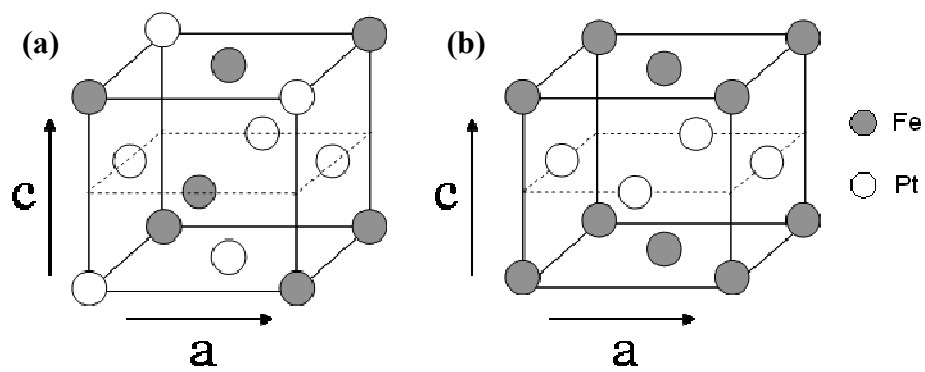


Figure 3.2 (a) fcc crystalline structure for A1 phase FePt ($c = a$) (b) fct crystalline structure for L1₀ phase FePt ($c = 0.96a$)

3.3 Energy control of gas phase nanoparticle formation

As discussed in the section 2.2, the formation of nanoparticles in gas phase is a completely thermodynamic process, in which the energy of individual atoms, nuclei and ions determined the final state of the particles. Therefore in order to control the properties or final state of the particles, it is critical to control the energy of atoms, nuclei and ions involved in the nanoparticles formation.

3.3.1 Initial Energies of Ar^+ ions, Fe, Pt atoms outside the plasma region

In the sputtering based gas phase synthesis system shown in Figure 3.1, the energy source and energy flow that involved are all directly related to the plasma. To quantitatively analyze the energy and energy transfer inside the plasma region, a simplified configuration of the sputtering system is used to calculate the energy of the atoms and ions in the plasma region, as shown in Figure 3.3.

Plasma is basically an ionized gas which consists of Ar^+ ions and electrons e^- . Since the sputtering chamber is full of Ar gas, Ar atoms also exist in the plasma region.

During the sputtering process, FePt metal target is connected to the cathode, facing the plasma area. Therefore Ar^+ ions are accelerated by the electrical field between the cathode and anode and fly to the target. For typical magnetron plasma

the average ion energy has been determined to be³¹:

$$E_i = 0.733 \times V_{DC} (eV) \quad (3.1)$$

Since the working DC voltage between the cathode and anode is usually around 300 V, the kinetic energy of the Ar^+ ions just before they hit the target is about 220 eV. The target material atoms (Fe and Pt atoms in this case) are knocked out of the metal target through the bombardment by Ar^+ ions. The kinetic energy of

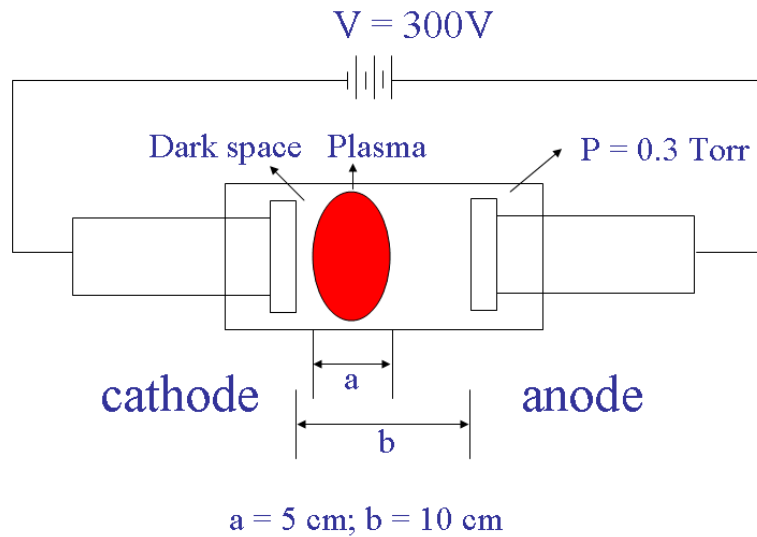


Figure 3.3 Simplified configuration of the sputtering system

Ar^+ ions is dissipated in three ways: one is to break the bonding of Fe and Pt atoms in the metal target, second is to transfer to the kinetic energy of free Fe and Pt atoms, third is the residue kinetic energy of Ar^+ ions. The kinetic energy of free Fe and Pt atoms are about 10 eV ³², according to the thermal energy at temperature of $1.2 \times 10^6\text{ K}$.

3.3.2 Energies of Ar⁺ ions, Fe, Pt and Ar atoms in plasma region

If there is no current, DC voltage drop is uniformly distributed in the plasma region. However, during the sputtering process, the DC voltage drop mostly happens in the dark space on the target surface which is usually 1-2 mm wide. But the voltage drop in the whole plasma region still has about 20 V^{33, 34}. Therefore the average energy gain per Ar⁺ ion from electrical field is about 10 eV.

The mean free path of Ar⁺ ions in the plasma is calculated by:

$$\lambda = \frac{RT}{\sqrt{2}\pi d^2 N_A P} \quad (3.2)$$

Here the R is gas constant, T is temperature, d is the diameter of Ar⁺ ion, N_A is Avogadro constant, and P is pressure. The mean free path of Ar⁺ ions is calculated to be 1 mm. As indicated in Figure 3.3, the width of plasma region is about 5 cm. Therefore if one Ar⁺ ion travels through the plasma, there will be about 50 collisions between Ar⁺ ion and Ar atoms.

The Ar atoms initially have thermal energy at room temperature. So energy will transfer from Ar⁺ ions to Ar atoms through collision. Since the numbers of Ar⁺ ions and Ar atoms have a ratio of 1:1000, the average energy transferred to one Ar atom will be 10eV/1000 = 0.01 eV. Therefore the average thermal temperature of Ar atoms should be 0.01eV/k_B + 300(room temperature) = 420 K. The average thermal temperature of Ar⁺ ions should be 10eV/50/k_B + 300(room temperature) = 2700 K.

3.3.3 Energy flow in plasma region

Based on the thermal energy calculations in section 3.3.2, the energy flow in the plasma region should be in a pattern as shown in Figure 3.4.

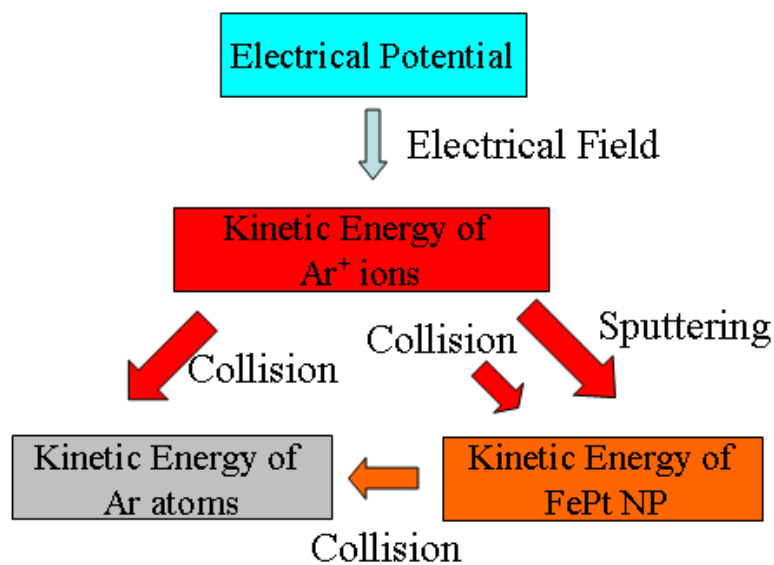


Figure 3.4 Energy source and energy flow during the sputtering based gas phase FePt nanoparticle synthesis process.

All the energies come from the electrical field. Ar⁺ ions gain kinetic energy directly from the electrical field and bombard with the FePt metal target. Fe and Pt atoms gain initial kinetic energy from Ar⁺ ions, and quickly cool down through collisions with low energy Ar atoms. Once the cooling process creates a supersaturated vapor of Fe and Pt atoms, Fe and Pt atoms begin the nanoparticle

formation process, which includes both the nucleation and growth processes. The kinetic energy of Fe and Pt atoms changes to the thermal energy of FePt nanoparticles.

The surrounding environment temperature is determined by Ar^+ ions and Ar atoms. Ar atoms gain energy from both Ar^+ ions and FePt nanoparticles through collision. Basically Ar^+ ions work as the heating source and Ar atoms work as the cooling source for FePt nanoparticles. Therefore the thermal environment of FePt nanoparticles during the formation process is totally determined by Ar^+ ions and Ar atoms in the plasma region.

Initially Fe and Pt atoms have really high energy (1.2×10^6 K), which is enough for FePt nanoparticle to form any crystalline structure. The final state of the FePt nanoparticles will completely depend on the cooling process. In other words, the final state of the FePt nanoparticles completely depends on the thermal environment. Therefore controlling the energy of Ar^+ ions and Ar atoms in the plasma region is equal to control the final state of FePt nanoparticles.

3.4 Important factors of gas phase nanoparticles synthesis

In this section, we will present our systematic study on several important experimental factors for the phase and size control of directly ordered L1₀ FePt nanoparticles and then give the physical understanding based on the energy control scheme. Finally, we will show how the phase and size of directly ordered L1₀ FePt nanoparticles are controlled simultaneously in experiments.

3.4.1 Aggregation time effect

Although all the experimental parameters are closely correlated when influence the FePt nanoparticle formation. We are still able to experimentally observe the influence of a single parameter when other parameters are fixed at certain value.

The first important factor related to the nanoparticle formation is the aggregation time, which is the total time of the nanoparticle nucleation and growth process. It is very straightforward that the aggregation time will heavily influence the nanoparticle formation. However it is not easy to experimentally determine the exact aggregation time of FePt nanoparticles. Considering that FePt nanoparticles are carried to the substrate by Ar carrier gas, the flowing rate of Ar carrier gas can be

used as an indicator for the aggregation time.

Figure 3.5 shows four samples of FePt nanoparticles fabricated using different Ar carrier gas flow rate. For sample (a) to (d), the carrier Ar gas flow rates are 16, 23, 30, 37 sccm respectively. If we assume the aggregation time is t_0 when carrier Ar gas flow rate is 37 sccm. Then the aggregation time for sample (a) to (d) are $2.3 t_0$, $1.6 t_0$, $1.23 t_0$, and t_0 , respectively.

It is clearly seen that following the shorten of the aggregation time, the big

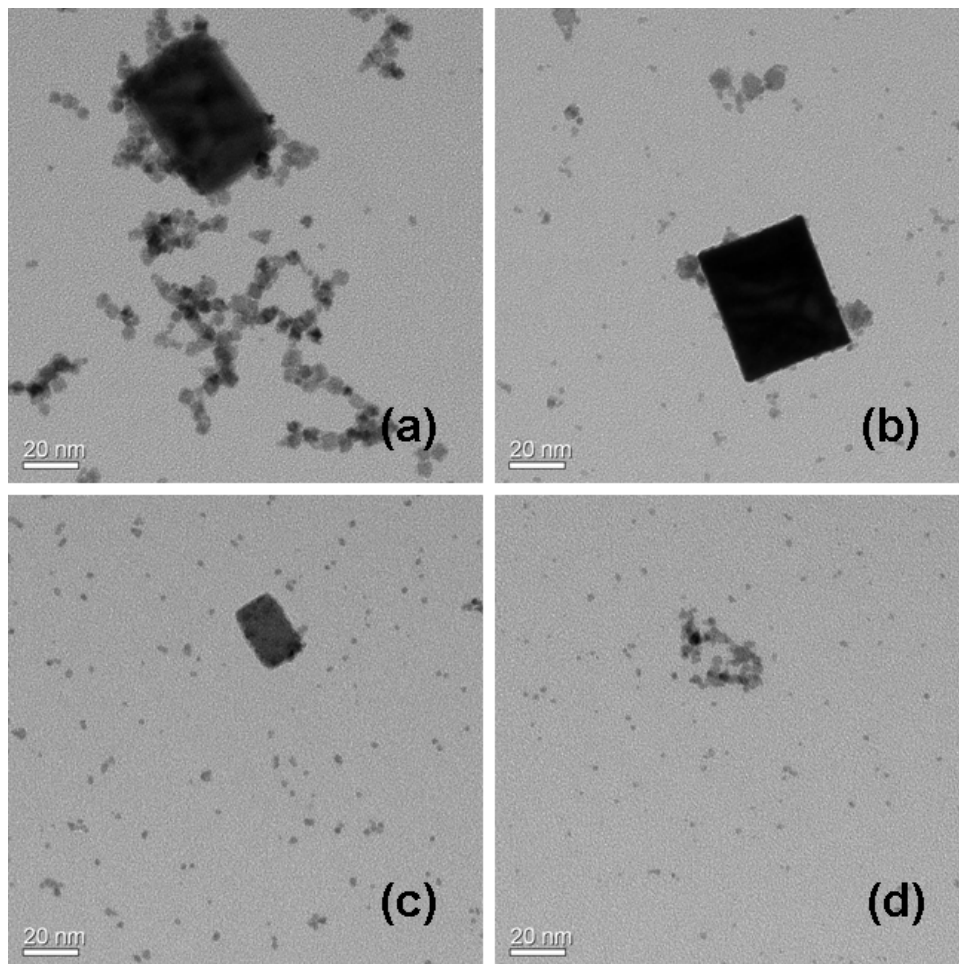


Figure 3.5 FePt nanoparticle fabricated with different aggregation time.

(a) $2.3 t_0$, (b) $1.6 t_0$, (c) $1.23 t_0$, and (d) t_0 .

black FePt nanoparticle gradually reduces its size and finally disappears. The yield and size of smaller particles that surrounding the big one also shows the trend of decreasing following the decreasing of aggregation time.

The result that the size of nanoparticle is proportional to aggregation time agrees well with our nanoparticle growth mode. Especially that for the big FePt nanoparticle whose size is larger than 50 nm, they are more likely formed in the agglomeration growth mode instead of surface growth mode.

3.4.2 Magnetic field effect

One of the most important new designs of our novel gas phase magnetic nanocomposite synthesis system is the modification of the magnetic field on target surface²⁵, as shown in Figure 3.6. Compared to the conventional magnetron sputtering target configuration, a ring and a cone made of iron are located on the top surface of the target. Figure 3.6 shows the cross-section view of the target configuration. The iron ring and cone are shown in yellow color.

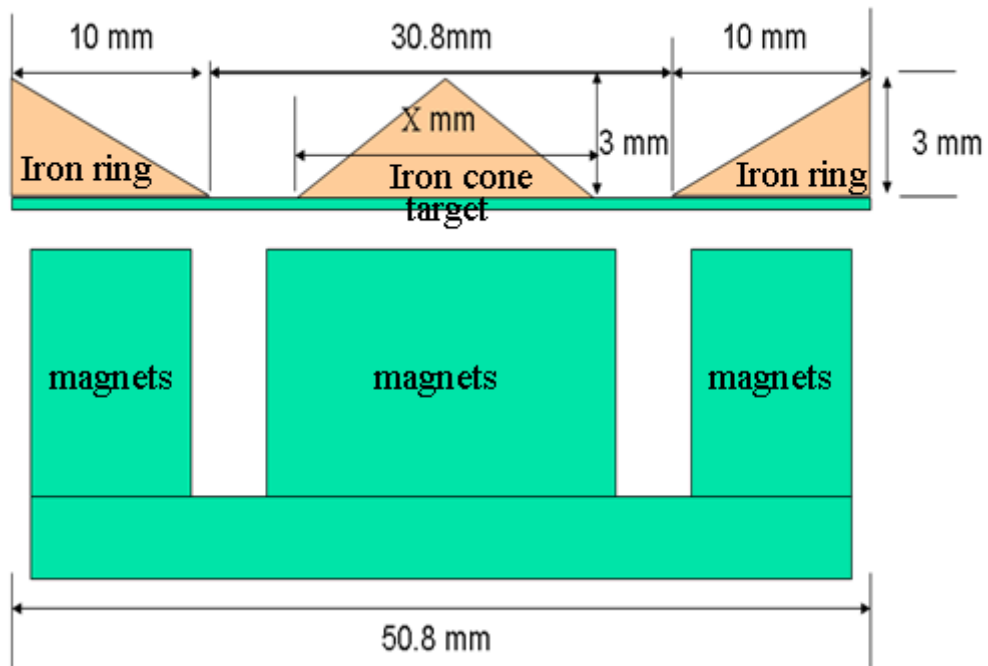


Figure 3.6 Modification of the magnetic field on target surface.

While the dimensions of the iron ring are fixed, the iron cone has a variable width, as indicated in the figure.

For magnetron sputtering, the shape of the plasma region is determined by the magnetic field on the target surface. The surface magnetic field is normally supplied by the permanent magnets on the back of the sputtering target. The conventional target configuration works well when the target material has low magnetic permeability. However when the target materials are ferromagnetic with high permeability, most of the magnetic flux are maintained inside the target, very few magnetic flux are going out of the target. So the surface magnetic field is very weak. In this case, the plasma region is narrow and the plasma density is low which are not

preferred by nanoparticle fabrication.

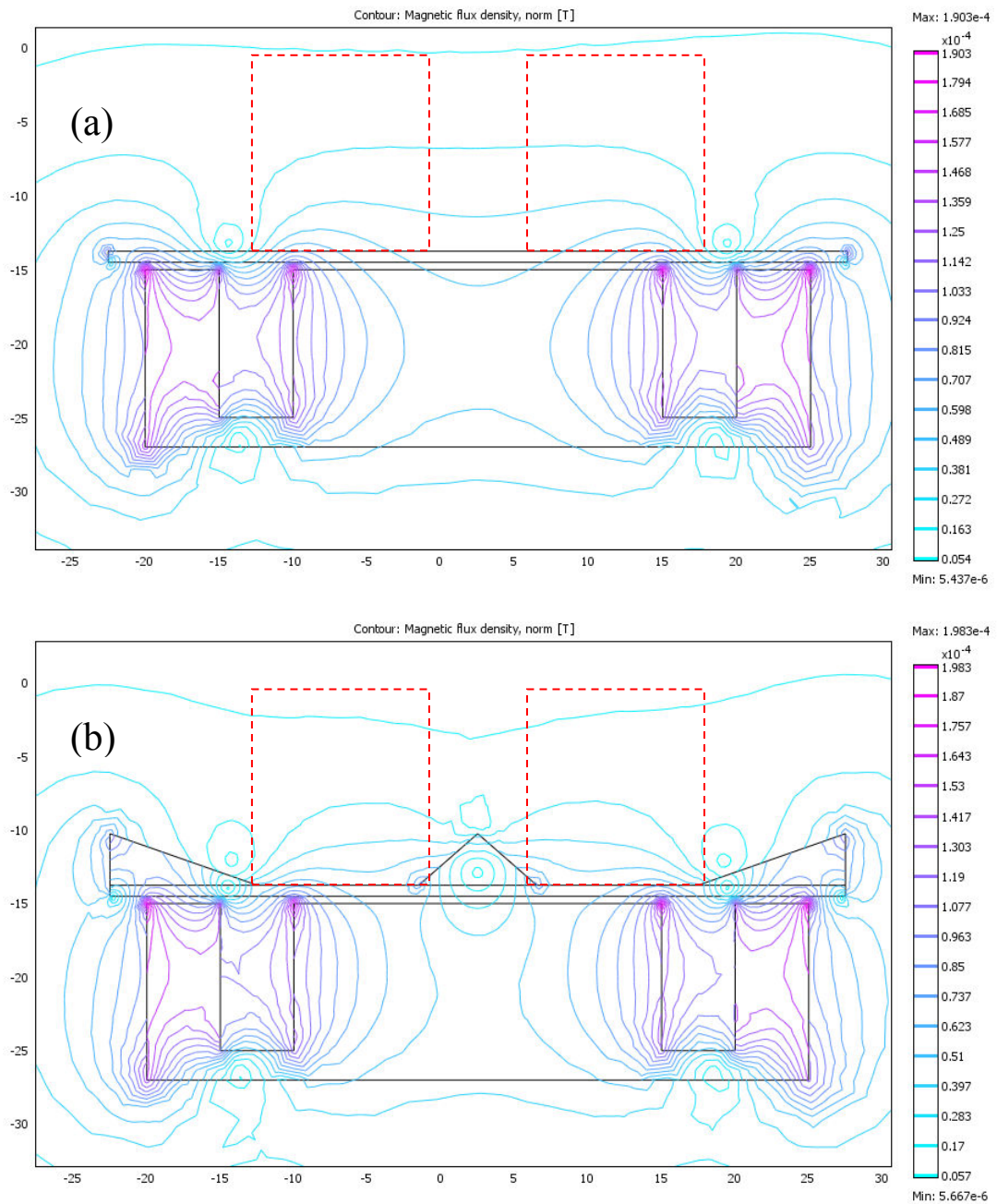


Figure 3.7 Contour plot of the magnetic flux density on the cross-section plane of the (a) conventional target configuration and (b) our new designed target configuration.

The adding of the iron ring and iron cone with high magnetic permeability successfully changes the magnetic flux density on the target surface. To quantitatively study the effect of iron ring and cone on the target surface magnetic field, FEMLAB is used to calculate the magnetic flux density on target surface. In Figure 3.7, the magnetic flux density for (a) convention target configuration and (b) target with iron ring and cone configuration are contour plotted. The areas of interest are the plasma regions, which are indicated by red dashed lines, as shown in Figure 3.7. There are two most important points showing up after comparing Figure 3.7 (a) and (b):

1. By adding the iron ring and cone, which are made of high permeability material iron, magnetic flux is more extended outside the target. Therefore, the magnetic field is stronger in the plasma region, especially the component of magnetic field that is parallel to the target surface. The parallel magnetic field has the effect of trapping electrons, which can effectively decrease the difficulty of plasma generation and increase the plasma density. Furthermore, because of the extension of magnetic flux, the plasma region is elongated in the perpendicular direction of target. The increase of plasma density and elongation of the plasma region give us more freedom to control the energy environment and manipulate the nanoparticle nucleation and growth²⁵.

2. Magnetic flux is confined between the iron ring and cone and especially dense in the area close to the edge of iron ring and cone. Therefore the sputtering

track width, which is under the plasma region and on the sputtering target surface, is directly defined by the width of the iron ring and cone. In this study, the iron ring width is fixed. Therefore the sputtering track width is only determined by the width of the iron cone.

The effects of the different iron cone width are experimentally studied and the results are shown in Figure 3.8. Figure 3.8 (a) (b) and (c) are the $L1_0$ FePt nanoparticles fabricated using iron cone width of 10 mm, 20 mm, and 25 mm respectively. The discharge current is fixed at 0.9 A. 570 mTorr gas pressure is used.

In Figure 3.8, left column shows the TEM bright field images of $L1_0$ FePt nanoparticles and right column shows the TEM diffraction patterns of $L1_0$ FePt nanoparticles. It is clearly seen that:

1. The nanoparticle yield is increasing following the increase of iron cone width.
2. The size of nanoparticle is more uniform following the increase of iron cone width.
3. The chemical ordering of the $L1_0$ FePt nanoparticles is increasing following the increase of iron cone width. Here the chemical ordering is estimated by comparing the relative diffraction strength of (110) and (111) diffraction ring.

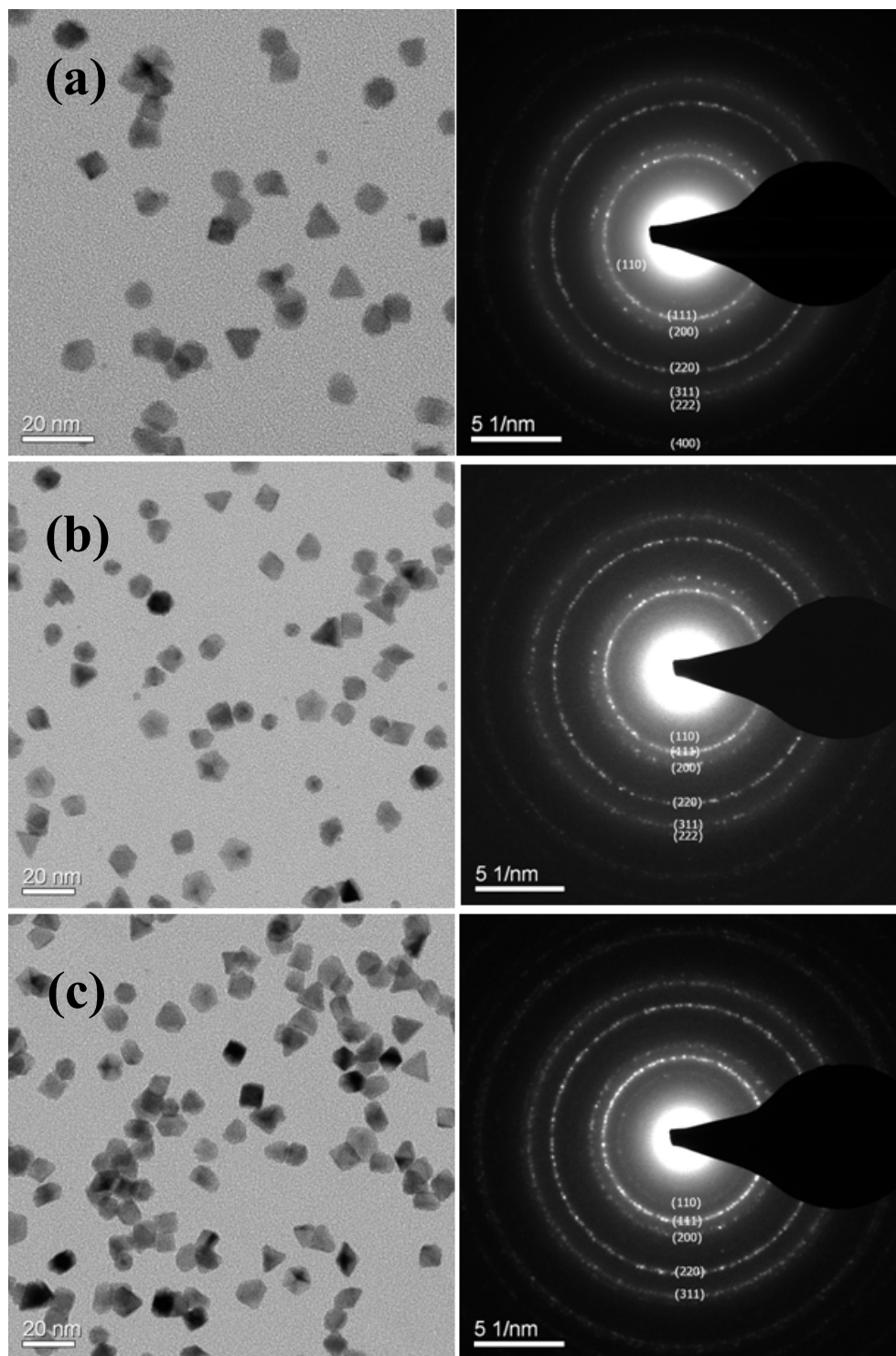


Figure 3.8 $L1_0$ FePt nanoparticle fabricated with different cone width. Cone widths used are (a) 10mm (b) 20mm (c) 25mm.

Basically all these effects are related to the plasma density and plasma uniformity on the sputtering track. For narrow iron cone width (10 mm), the separation of iron ring and iron cone is large. Plasma density are higher at the region close to iron ring and cone edge and lower at the region away from both iron ring and cone (center area of the sputtering track). This causes non-uniform sputtering on the track. Since the plasma density is low at the center area of the sputtering track, the effective sputtering track width is small. For broader iron cone width (20, 25 mm), iron ring and iron cone are fairly close, absolute sputtering track width is narrower. However, the plasma density are more uniform cross the whole sputtering track, and plasma density is also high at the sputtering track center, the effective sputtering track width is in fact broader than the case of narrow iron cone. The increase of plasma uniformity and effective sputtering track width explains the yield, uniformity and ordering increase of $L1_0$ FePt nanoparticle with broader iron cone.

3.4.3 Gas pressure effect

As in the discussion about the energy flow in gas phase nanoparticle nucleation and growth, the Ar gas works as the cooling source. The thermal energy transfers from FePt nanoparticles to Ar atoms by collision. The higher the Ar gas pressure, the higher the collision frequency is. Therefore the cooling rate of the FePt

nanoparticle is proportional to the Ar gas pressure. The gas pressure has great impacts on both the FePt particle nucleation and growth.

For nanoparticle nucleation, higher gas pressure leads to larger super saturation ratio, therefore more nuclei are formed compared to low gas pressure. For nanoparticle growth, different cooling rate leads to different nanoparticle structure. Normally, only in a certain range of cooling rate, FePt nanoparticle can form single crystal structure with $L1_0$ chemically ordered phase. If the cooling rate is too low, FePt nanoparticles have small size and are in A1 chemically disordered phase. If the cooling rate is too high, FePt nanoparticles usually have polycrystalline structure which is the result of particle agglomeration.

If sputtering Ar gas and carrier Ar gas are using the same gas input, gas pressure effect is then related to the aggregation time effect, which makes the situation more complicated.

For the 4 samples shown in Figure 3.9 (a)-(d), Ar gas flow rate are 16, 19, 22 and 25 sccm respective, corresponding to the gas pressure of (a) 390 mTorr, (b) 452 mTorr, (c) 514 mTorr and (d) 573 mTorr. The discharge current is fixed at 0.8 A. 25 mm iron cone is used.

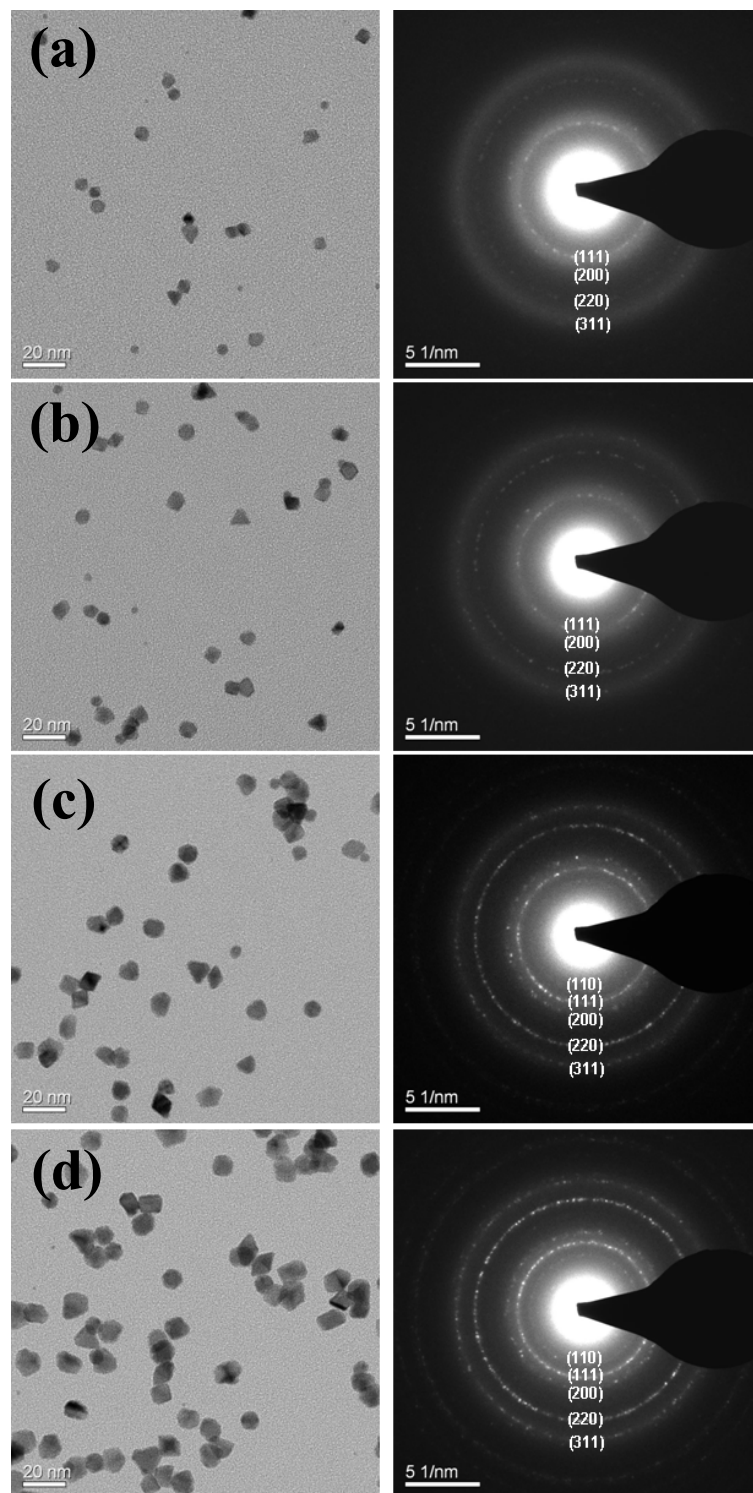


Figure 3.9 $L1_0$ FePt nanoparticles fabricated at different gas pressure: (a) 390 mTorr, (b) 452 mTorr, (c) 514 mTorr and (d) 573 mTorr.

If sputtering Ar gas and carrier Ar gas are using the same gas input, gas pressure effect is then related to the aggregation time effect, which makes the situation more complicated.

For the 4 samples shown in Figure 3.9 (a)-(d), Ar gas flow rate are 16, 19, 22 and 25 sccm respective, corresponding to the gas pressure of (a) 390 mTorr, (b) 452 mTorr, (c) 514 mTorr and (d) 573 mTorr. The discharge current is fixed at 0.8 A. 25 mm iron cone is used.

The results from Figure 3.9 (a)-(d) are:

1. The yield of nanoparticles increases with gas pressure.
2. The size and size uniformity increases with gas pressure.
3. The crystallinity and chemical ordering of nanoparticles increases with gas pressure. FePt nanoparticles in Figure 3.9 (a) and (b) are in A1 phase. FePt nanoparticles in Figure 3.9 (c) and (d) are in L1₀ phase.

The low pressure induces low super saturation ratio and low cooling rate, which cause low density of formed nuclei and low growth rate. Therefore at low temperature, the yield of nanoparticles is low and the size of nanoparticle is small. When the gas pressure increases to a proper range, not only are the yield and size of FePt nanoparticles increased, but also the crystallinity of FePt nanoparticles are improved and finally reaches L1₀ phase. However, further increase the gas pressure, the gas flow rate is too high which causes the aggregation time greatly shortened.

Also the cooling rate is too fast at high pressure. Therefore the yield, size and crystallinity of FePt nanoparticle move to the worse direction.

3.4.4 Discharge current effect

As in the discussion about the energy flow in gas phase nanoparticle nucleation and growth, Ar^+ ions work as the heating source. Ar^+ ions not only give Fe and Pt atoms extremely high initial energy, but also change the cooling rate of FePt nanoparticles in the plasma region. Discharge current represents the total number of Ar^+ ions involved in the sputtering process. Therefore the larger the discharge current, the higher the temperature in the plasma region, which means the slower the cooling rate.

Figure 3.10 (a)-(d) shows the TEM bright field image and diffraction patterns of 4 samples of FePt nanoparticle fabricated at discharge currents of (a) 0.6 A, (b) 0.8 A, (c) 0.9 A and (d) 1.0 A respectively. The fabrication gas pressure is fixed at 573 mTorr. 25 mm iron cone is used.

There are two phenomenons that are clearly observed in Figure 3.10:

1. The total nanoparticles yield increases when discharge current increases from 0.6 A to 0.9 A, and decreases when discharge current further increases from 0.9 A to 1.0 A.

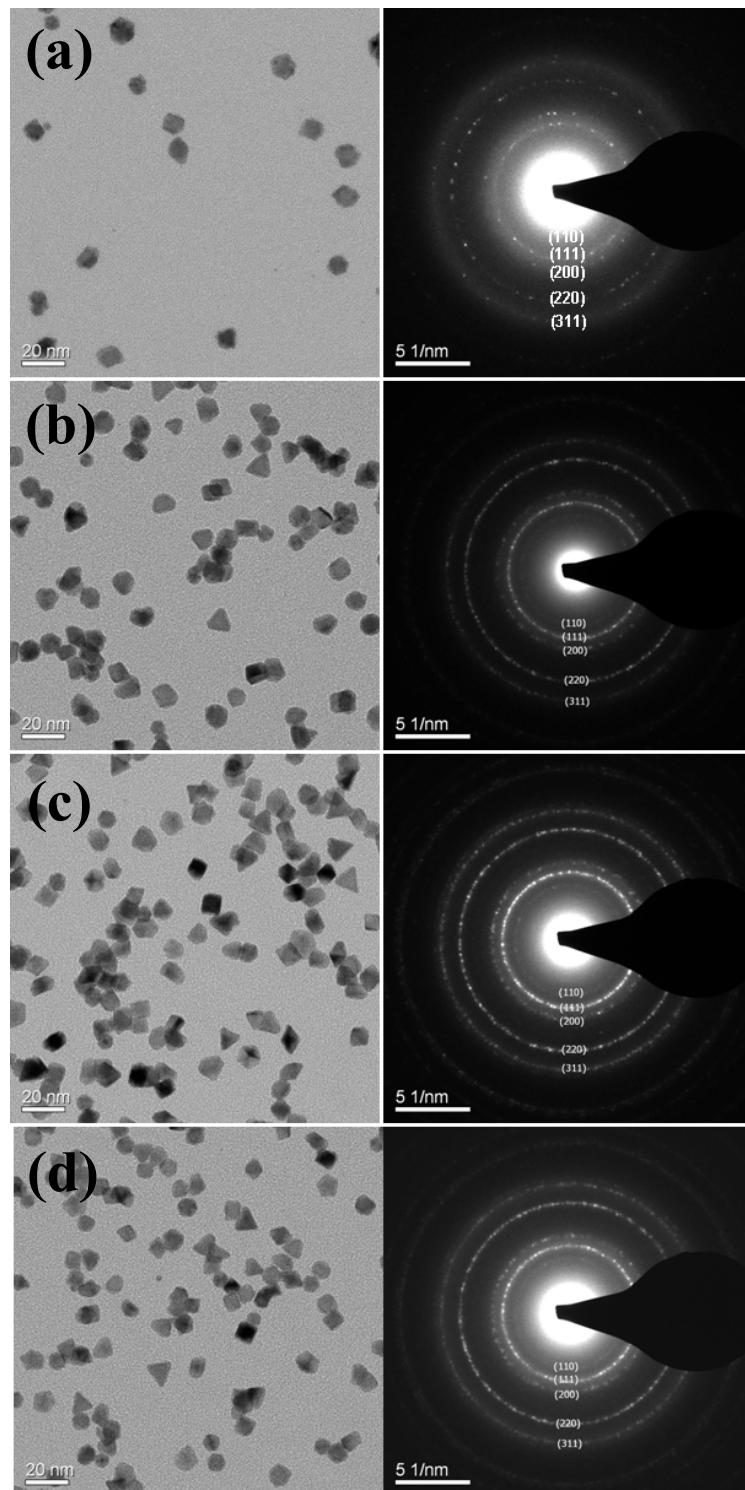


Figure 3.10 L1₀ FePt nanoparticles fabricated at different discharge current: (a) 0.6 A, (b) 0.8 A, (c) 0.9 A and (d) 1.0 A.

2. The crystallinity of FePt nanoparticle improves when discharge current increases from 0.6 A to 0.9 A, but becomes worse when discharge current further increases from 0.9 A to 1.0 A.

The explanation is when discharge current is as low as 0.6 A, the cooling rate is high since discharge current is a heating source, which causes bad crystallinity. And the sputtered Fe and Pt free atoms density is low at low discharge current which causes low nanoparticles total yield. When discharge current increases from 0.6 A to 0.9 A, the cooling rate is slowed down and sputtered Fe and Pt free atoms density increases. Therefore both the yield and crystallinity of FePt nanoparticles are improved. However when discharge current further increases from 0.9 A to 1.0 A, the heating is overshoot, so the cooling rate is too slow. Both the nucleation rate and surface growth rate of FePt nanoparticles is low. Therefore both the yield and crystallinity of FePt nanoparticles move to the worse direction.

3.5 Simultaneously control of the phase and size of directly ordered L1₀ FePt nanoparticles

3.5.1 Experiment setup

All FePt nanoparticles were fabricated by DC sputtering FePt targets using a home-made gas condensation nanoparticle deposition system, as shown in Figure 3.1. The schematic drawing of the nanoparticle deposition system is shown in figure 1(a). The base pressure of the sputtering chamber was 5×10^{-8} Torr. Argon (Ar) gas was used as both sputtering gas and carrier gas. All the substrates that were used to collect nanoparticles including TEM grids and Si wafers were kept at room temperature during the whole process of nanoparticle fabrication.

The microstructure and morphology of FePt nanoparticles were examined by a FEI Tecnai F30 Transmission Electron Microscopy (TEM). The composition of FePt nanoparticles was tested by TEM energy dispersive x-ray analysis (EDX). The magnetic properties of FePt nanoparticles were characterized by a superconducting quantum interference device (SQUID) magnetometer.

3.5.2 Results and discussion

The nucleation and growth processes of FePt nanoparticles start and completely

finish in gas phase. FePt nuclei are formed through the condensation of supersaturated vapor of Fe and Pt atoms. Thereafter FePt nuclei continue to grow either by surface growth or by coagulation. The microstructure and morphology of FePt nanoparticles are directly determined by the thermal conditions in the thermal dynamic process of particle nucleation and growth. Therefore the formation of $L1_0$ ordered phase and particle size control can be realized by controlling the thermal environment of FePt nanoparticles during the fabrication.

The energy flows in the gas phase synthesis of nanoparticles are shown in Figure 3.4. First, Ar^+ ions in the plasma gain kinetic energy through DC electrical field acceleration. Then, Fe and Pt atoms are knocked out from the alloy target by high energy Ar^+ ions and gain initial kinetic energy from Ar^+ ions. FePt particles begin to form when the energized Fe and Pt atoms reach supersaturation in the Ar gas. Most of the kinetic energy of Fe and Pt atoms changes to the Gibbs free energy of FePt nanoparticles. FePt nanoparticles are very “hot” at the beginning, and then cooled down by collision with Ar atoms which are in low energy state and working as cooling gas. Energy is also transferred between Ar^+ ions and Ar atoms. During the whole process of FePt nanoparticles’ formation, energy keeps transferring among the Ar^+ ions, FePt nanoparticles and Ar atoms. Therefore in experiments, the initial energy of FePt nanoparticles can be adjusted by controlling the sputtering voltage and current density, and the cooling rate of FePt nanoparticles can be controlled by Ar gas pressure.

Based on experimental results, the energy (thermal environment) requirements of fabricating $L1_0$ phase FePt nanoparticle are shown in a qualitative manner in Figure 3.11.

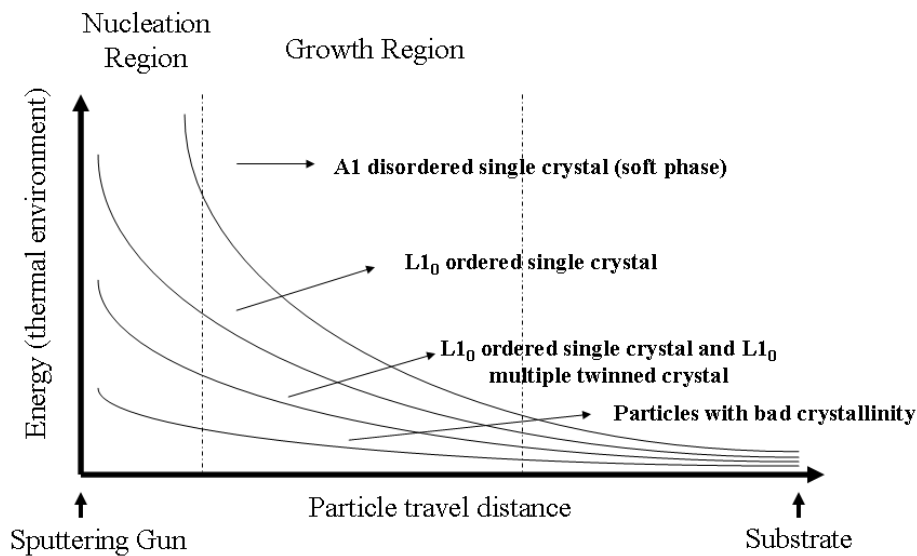


Figure 3.11 Energy (thermal environment) requirements for the formation of $L1_0$ FePt nanoparticles in gas phase.

The x axis represents the distance between the sputtering gun and substrate. The energy of FePt nanoparticles is in a decreasing trend following their travelling distance because of collisions with Ar atoms. If starting with high initial energy and cooling down at a fast rate, FePt nanoparticles prefer to form A1 disordered phase. When the initial energy and cooling rate are reduced to a proper value, FePt nanoparticles will form $L1_0$ ordered single crystals. If the initial energy and cooling

rate are further reduced, FePt nanoparticles can still form $L1_0$ phase, but particles will be a mixture of single crystals and multiply twined crystals. But if the initial energy and cooling rate are reduced to an extremely low level, FePt nanoparticles can not form good crystallized structure. The explanation for these behaviors is: when FePt nanoparticles possess high initial energy, FePt nanoparticles are in A1 disordered phase. Because Fe and Pt atoms have plenty of energy to relocate in FePt particles, Fe and Pt atoms are randomly distributed in FePt nanoparticles. So if FePt nanoparticles are cooled down too fast, their A1 disordered structure will be kept. When FePt nanoparticles are given with too low initial energy, Fe and Pt don't have the ability to move in FePt nanoparticles. So FePt nanoparticles can not be well crystallized. Only with enough initial energy and a relatively slow cooling rate, Fe and Pt atoms in the FePt nanoparticles have the ability and time to form $L1_0$ ordered structure, which is a low temperature favored state. Therefore, to control the initial energy and cooling rate of FePt nanoparticles, sputtering voltage, current density and Ar gas pressure need to be adjusted to appropriate values. Higher or lower value of sputtering voltage, current density and Ar gas pressure resulted in A1 not $L1_0$ phase FePt nanoparticles.

Besides disclosing the phase control of FePt nanoparticles, another achievement in this study is the particle size control. Figure 3.12 shows experimental factors for the simultaneously control the phase and size of $L1_0$ FePt nanoparticles.

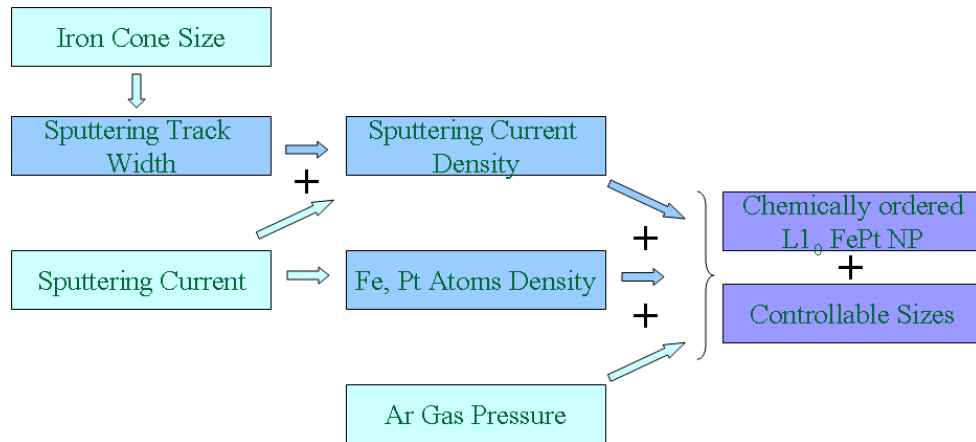


Figure 3.12 Experimental factors for the simultaneously control of the phase and size of $L1_0$ FePt nanoparticles.

While the energy (thermal environment) controls the phase formation of FePt nanoparticle, the atom density of Fe and Pt atoms in the region of particle formation controls the size of FePt nanoparticles. Since the Ar^+ ions work as the heating source and Ar atoms work as the cooling source, the energy (thermal environment) of FePt nanoparticles in growth process is determined by the discharge current (sputtering current) density and the Ar gas pressure. The density of Fe and atoms is determined by the total discharge current. Therefore, to simultaneous control the phase and size of FePt nanoparticles, we need to explore the proper combinations of discharge (sputtering) current density, Fe and Pt free atom density and Ar gas pressure, As shown in Figure 3.12.

From the principle of DC sputtering, the atom density of Fe and Pt atoms is

determined by the total sputtering current. However, the sputtering current density has to be kept in a fixed value while the total sputtering current is adjusted. In this study, combinations of an iron ring and an iron cone with different diameters (10 mm to 25 mm) are added to the surface of sputtering target to control the sputtering track width and adjust the plasma. The sputtering track width decreases with the increase of the iron cone's diameter. In this way, sputtering current density can be kept constant while the total sputtering current can be adjusted in a wide range. The required Ar gas pressure for a fixed cooling rate is also different for FePt nanoparticles with different sizes. The reason is that the energy losing rate of larger particles is slower than smaller particles at the same cooling gas pressure.

Figure 3.13 shows the successful fabrication of $L1_0$ FePt nanoparticles with three different sizes. The experimental parameters of fabricating $L1_0$ FePt nanoparticles with different sizes are illustrated in a qualitative manner in Figure 3.13 (a). The Fe and Pt atom densities refer to the atom density of Fe and Pt in the gas phase during the sputtering process. It shows that large $L1_0$ FePt nanoparticles (17nm) were fabricated at the condition of high Fe and Pt atom density and high Ar gas pressure, smaller $L1_0$ FePt nanoparticles (12nm) were fabricated at relatively smaller Fe and Pt atom densities and lower Ar gas pressure and 6nm $L1_0$ FePt nanoparticles were fabricated at smallest Fe, Pt atom density and lowest Ar gas pressure. The sputtering current densities for these FePt particles with different size were slightly different.

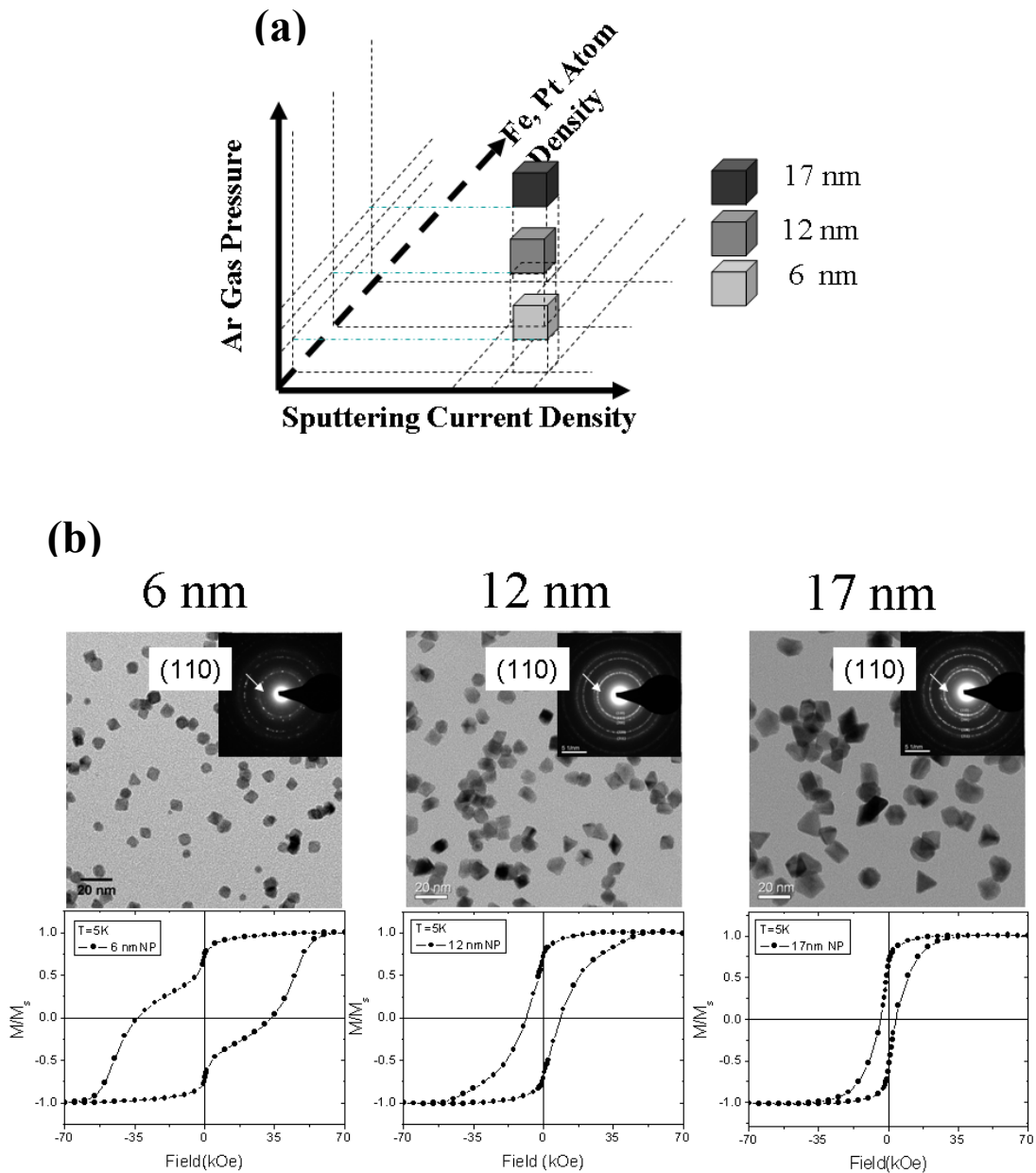


Figure 3.13 (a) Size control of $L1_0$ FePt nanoparticles. (b) TEM bright field images, TEM diffraction patterns and magnetic hysteresis loops of $L1_0$ FePt nanoparticles with sizes of 6nm, 12 nm and 17nm.

Figure 3.13 (b) shows the TEM bright field images, TEM diffraction patterns and the hysteresis loops of FePt nanoparticles. The composition of all FePt nanoparticles tested by TEM-EDX is found to be Fe₄₉Pt₅₁. The TEM bright field images show that the sizes of FePt nanoparticle are 6(1±0.11)nm, 12(1±0.11)nm and 17(1±0.11)nm sizes, respectively. All three TEM diffraction patterns of FePt nanoparticles show (110), (111), (200), (220), (311) and (222) diffraction rings. Since (110) diffraction ring is one of the fingerprints of FePt L₁₀ phase, this result reveals that FePt nanoparticles with all three mean sizes are in L₁₀ chemically ordered phase. From the hysteresis loops, 6nm nanoparticles show the highest coercivity field, 33 kOe at 5K. The measured coercivity fields of 12nm and 17nm nanoparticles at 5K are 9 kOe and 4 kOe respectively. There are two reasons for the relatively low coercivity for 12nm and 17nm L₁₀ FePt nanoparticles. The first one is that the sputtering current densities for 12nm and 17nm nanoparticles are smaller than 6nm nanoparticles, which could cause the ordering parameters of 12nm and 17nm L₁₀ FePt nanoparticles smaller than that of 6nm L₁₀ FePt nanoparticles (shown in figure 3.13 (a)). The magnetic anisotropy constant (K_u) of 6nm FePt particles, estimated from the saturation field and magnetization, is about 3×10^7 erg/cm³. The order parameter of 6nm FePt particle is about 80-85%, estimated from the ordering parameter dependence of FePt anisotropy constant^{35, 36}. For 12nm and 17nm FePt particles, the ordering parameters are estimated in the range of 75-80%.

The second reason is that nanoparticles with multiply twinned structure appear in 12nm and 17nm $L1_0$ FePt nanoparticles, which are caused by the smaller sputtering current density and larger Ar gas pressure.

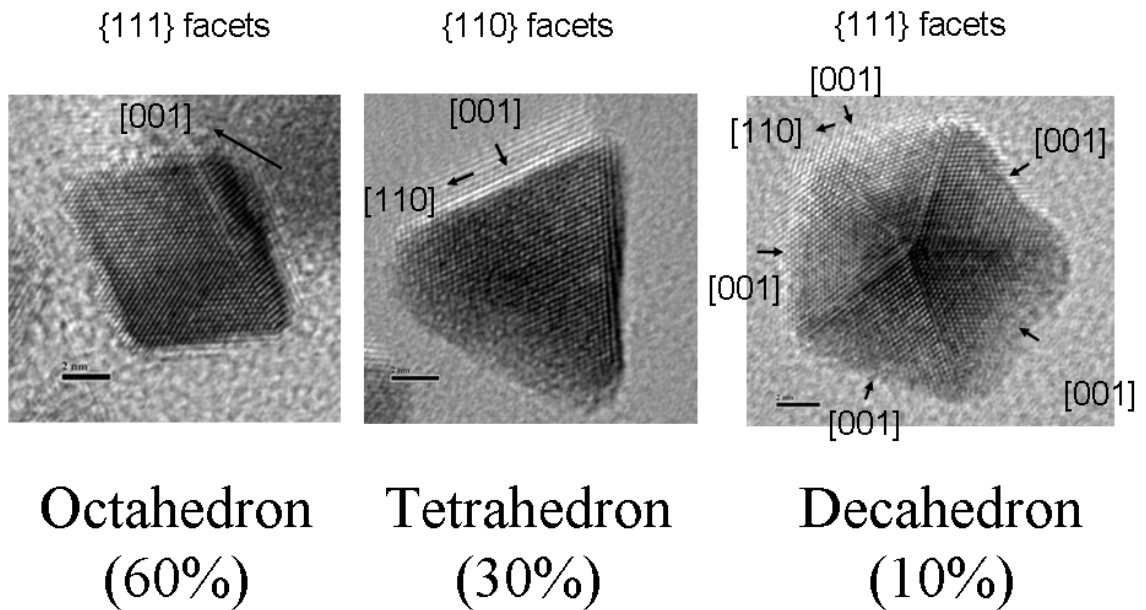


Figure 3.14 Three different morphologies of 12 nm $L1_0$ FePt nanoparticles observed by HRTEM.

Figure 3.14 shows the three typical shapes existing in the 12nm $L1_0$ FePt nanoparticles. The first one is octahedron shape with eight $\{111\}$ facets. The second one is tetrahedron shape with four $\{110\}$ facets. The first two are both single crystal nanoparticles. The third one is decahedron shape with 10 $\{111\}$ facets, which is a multiply twinned structure. The ratios of 12nm nanoparticles with octahedron, tetrahedron and decahedron shapes are 60%, 30% and 10% respectively. As a

reference, for 6nm $L1_0$ FePt nanoparticles, only octahedron and tetrahedron shapes are observed, decahedron shape is absent. For 17nm $L1_0$ FePt nanoparticles, the ratio of decahedron shaped particles increased to 15%. As shown in the HRTEM images (Figure 3. 14), octahedron and tetrahedron shaped $L1_0$ FePt nanoparticles have a single (001) easy axis, while decahedron particles have five (001) easy axes all point to the center. The theoretical coercivity value of decahedron shape particle is zero. Therefore, decahedron shaped FePt nanoparticles will drag down the overall coercivity for 12nm and 17nm $L1_0$ FePt nanoparticles. The observation shown in Figure 3.14 also reveals that the morphologies of $L1_0$ FePt nanoparticles critically depend on the energy conditions (thermal environment) of nanoparticles' nucleation and growth.

3.5.3 Summary

Simultaneously controlling the chemical ordering and size of FePt nanoparticle was successfully achieved in gas phase synthesis. It was found that energy conditions (thermal environment) were more responsible for the chemical ordering of FePt nanoparticles. Meanwhile the mean size of FePt nanoparticles was more related with the initial Fe and Pt atoms' density. Multiply twined structure were found in 12nm and 17nm $L1_0$ FePt nanoparticles, but were absent in 6nm $L1_0$ FePt nanoparticles.

3.6 Matrix material fabrication and orientation control of magnetic nanocomposites

In previous sections, we detailed studied our novel gas phase magnetic nanoparticle (nanocluster) synthesis process. In this section, we discuss the fabrication process of the whole magnetic nanocomposites materials, including the matrix fabrication.

As shown in Figure 3.1, the matrix materials for the nanocomposites are fabricated by a separated magnetron sputtering gun, which is placed in the substrate chamber. Different to the nanoparticle (nanocluster) deposition source which works in a relatively high Ar gas pressure range (300-600 mTorr), the matrix sputtering gun usually works in a low Ar gas pressure range (1-10 mTorr) which is similar to the pressure range for thin film materials fabrication. At low Ar gas pressure, matrix materials are denser and close contacts with the nanoparticles (nanoclusters) that are going to be embedded in the nanocomposites. The working principles of matrix fabrication therefore are the same as thin film sputtering technique³⁷.

Figure 3.15 illustrated the co-deposition process of magnetic nanocomposite materials. While nanoparticles (nanoclusters) are carried to substrate by Ar gas flow from the nanoparticle deposition chamber, the matrix materials are co-deposited to the substrate by the matrix sputtering gun. The matrix materials reach the substrate

in form of atoms³⁷, therefore close contact between matrix and nanoparticles can be expected. Theoretically, as many as needed nanoparticle deposition sources and matrix sputtering guns can be placed into this gas phase nanocomposite synthesis system. In our study, only one nanoparticle deposition source and one matrix sputtering gun are used to demonstrate this synthesis process.

Co-deposition of Nano-Particles and matrix film

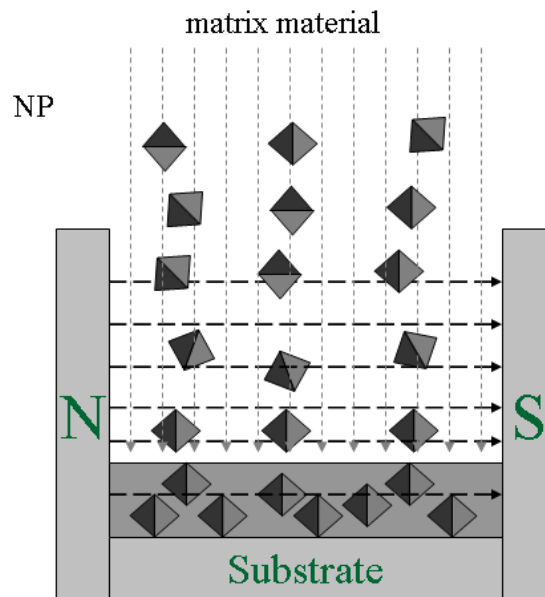


Figure 3.15 Substrate configuration for co-deposition of nanoparticles (NP) and matrix materials.

One of the most important advantages of our magnetic nanocomposite synthesis process is the ability to control the orientation of the magnetic

nanocomposites. Permanent magnets can be allocated on the substrate holder to supply an external magnetic field, as shown in Figure 3.15. Therefore, these magnetic materials are magnetized by the external field during the process of approaching to the substrate. Since the nanoparticles (nanoclusters) and the matrix materials are all magnetic materials and all of them are deposited onto the substrate in gas phase, these magnetized magnetic materials will rotate their moment direction along the external field direction to minimize the magnetic static energy. In this way, the easy-axis orientation control of the magnetic nanocomposite materials is achieved. The experimental demonstration of the orientation control will be shown in chapter 5, “Gas phase synthesis of FePt/Fe-Ni anisotropic-exchange-spring nanocomposite”.

3.7 Advantages of the novel gas phase nanocomposite synthesis process

Comparing to the conventional nanocomposite synthesis technique such as the PVD and CVD methods discussed in chapter 2, our novel gas phase nanocomposite synthesis process has following advantages:

1. It is a general process, which is applicable for most of the magnetic materials. And it is compatible with current widely used industrial sputtering systems.
2. Magnetic materials involved in the nanocomposite materials are synthesized independently in different vacuum chambers, which give the freedom to manipulate all the materials independently.
3. Nanostructured magnetic materials are all synthesized in gas phase without any post-annealing like treatment, which not only give the freedom to engineer the composite material during deposition such as easy-axis alignment etc, but also avoid the problems in nanostructured material fabrication such as agglomeration and lattice twinning etc.

3.8 Summary

In this chapter, our novel gas phase nanocomposite synthesis process is introduced. FePt nanoparticle is used to detail explain our new understanding of gas phase nanoparticle formation process (energy control model). Base on our new energy control model of gas phase nanoparticles formation process, simultaneously control of the phase and size of $L1_0$ FePt nanoparticles is successfully achieved. Finally, the matrix fabrication method and orientation control design for magnetic nanocomposite materials are presented.

Reference:

- ¹ H. N. Bertram, Theory of magnetic recording (Cambridge University Press, Cambridge, New York, 1994).
- ² S. X. Wang and A. M. Taratorin, Magnetic information storage technology (Academic Press, San Diego, 1999)
- ³ Ziese M and Thornton M J (ed) 2001 Spin Electronics (Berlin: Springer)
- ⁴ Coey J M D, Viret M and von Moln'ar S 1999 Adv. Phys. 48 167
- ⁵ Grunberg P, Schreiber R, Pang Y, Brodsky M B and Sowers H, Phys. Rev. Lett. 57, 2442 (1986)
- ⁶ Baibich M N, Broto J M, Fert A, Nguyen Van Dau F, Petroff F, Etienne P, Creuzet G, Friederich A and Chazelas J, Phys. Rev. Lett. 61, 2472 (1988)
- ⁷ Cowburn R P and Welland M E, Science 287, 1466 (2000)
- ⁸ Lagmago Kamta G and Starace A F, Phys. Rev. Lett. 88, 107901 (2002)
- ⁹ C. G. Granqvist and R. A. Buhrman, J. Appl. Phys. 47, 2200 (1976).
- ¹⁰ K. Sattler, J. Muhlbach and E. Recknagel, Phys. Rev. Lett. 45, 821 (1980).
- ¹¹ H. Haberland, M. Karrais, M. Mall and Y. Thurner, J. Vac. Sci. Technol., A 10, 3266 (1992).
- ¹² C. G. Granqvist, R. A. Buhrman, J. Wyns and A. J. Sievers, Phys. Rev. Lett. 37, 625 (1976).

-
- ¹³ S. Stappert, B. Rellinghaus, M. Acet and E. F. Wassermann, *J. Cryst. Growth* 252, 440 (2003).
- ¹⁴ S. Stoyanov, V. Skumryev, Y. Zhang, Y. Huang, G. Hadjipanayis and J. Nogues, *J. Appl. Phys.* 93, 7592 (2003).
- ¹⁵ Z. R. Dai, S. H. Sun and Z. L. Wang, *Nano Lett.* 1, 443 (2001).
- ¹⁶ C. Antoniak et. al., *Phys. Rev. Lett.* 97, 117201 (2007)
- ¹⁷ M. E. Gruner, et. al., *Phys. Rev. Lett.* 100, 087203 (2008)
- ¹⁸ Michael Muller, Karsten Albe, *Acta Materialia* 55, 6617 (2007)
- ¹⁹ R. M. Wang, et. al. *Phys. Rev. Lett.* 100, 017205 (2008)
- ²⁰ C. A. Ross, *Annu. Rev. Mater. Res.* 31, 203 (2001).
- ²¹ Shouheng Sun, et al., *Science* 287, 1989 (2000).
- ²² D. Weller, A. Moser, L. Folks, M. E. Best, W. Lee, M. F. Toney, M. Schwickert, J. Thiele, and M. F. Doerner, *IEEE Trans. Magn.*, 36, 10 (2000)
- ²³ D. L. Peng, T. Hihara, and K. Sumiyama, *Appl. Phys. Lett.*, 83, 350 (2003).
- ²⁴ Z. R. Dai, S. Sun, and Z. L. Wang, *Nano Lett.* 1, 443 (2001).
- ²⁵ Jiaoming Qiu and Jian-Ping Wang, *Appl. Phys. Lett.* 88, 19205 (2006)
- ²⁶ Xiaoqi Liu and Jian-Ping Wang, *J. Appl. Phys.* 105, 07A722 (2009)
- ²⁷ Jiaoming Qiu, Jianmin Bai and Jian-Ping Wang, *Appl. Phys. Lett.* 89, 222506 (2006)
- ²⁸ K Wegner, P Piseri, H Vahedi Tafreshi and P Milani, *J. Phys. D: Appl. Phys.*, 39, R439–R459 (2006).

-
- ²⁹ O. A. Ivanov, L. V. Solina, V. A. Demshina, L. M. Magat, *Fiz. Metal. Metalloved.* **35**, 92 (1973)
- ³⁰ G. H. O. Daalderop, P. J. Kelly, and M. F. H. Schuurmans, *Phys. Rev. B.* **44**, 12054 (1991)
- ³¹ M. J. Goeckner, J. A. Goree, and T. E. Sheridan, *IEEE Trans. Plasma Sci.* **19**, 301 (1991)
- ³² J. A. Thornton, *Thin Solid Films*, **54**, 23 (1978)
- ³³ O.H. Chin, *Journal Fizik Malaysia*, **V.24** p107 (2003)
- ³⁴ V. I. Kirichenko, *Sov. Phys. - Techn. Phys.*, **21**(9), 1080 (1976)
- ³⁵ Okamoto S, et al, *Phys. Rev. B*, **66**, 024413 (2002)
- ³⁶ J B Staunton, et al, *J. Phys.: Condens. Matter*, **16**, S5623–S5631 (2004)
- ³⁷ Kiyotaka Wasa, Makoto Kitabatake and Hideaki Adachi, *Thin film materials technology: sputtering of compound materials*, Publisher William Andrew, New York (2004); Bunshah, R. F., (ed.), *Deposition Technologies for Films and Coatings*, Noyes Publications, NJ, (1982); Mattox, D. M., *Handbook of Physical Vapor Deposition Processing*, Noyes Publications, NJ (1998); Mahan, J. E., *Physical Vapor Deposition of Thin Films*, John Wiley & Sons, New York (2000); Elshabini-Riad, A., and Barlow, F. D., III, (ed.), *Thin Film Technology Handbook*, McGraw-Hill, New York (1997).

CHAPTER 4

THEORETICAL MODEL OF EXCHANGE-SPRING MAGNETS

4.1 Introduction to exchange-spring magnets

Permanent magnet materials are extremely widely used in various industries, including electronics (e.g. portable audio and video), information storage (e.g. Hard Disk Drive), medical devices (e.g. MRI), automotive industry (e.g. hybrid and fuel cell vehicles), motors, power generators, energy storage, etc. The Permanent magnets market in 2007 has reached 8,955 million dollars and will soar to 21,020 million dollars in 2020¹.

Energy product (energy density), $(BH)_{\max}$, is one of the most important characters of permanent magnets materials, which measures the magneto static energy stored in the magnets(strength of the magnets). However, since the development of rare earth permanent magnets (e.g. Sm-Co, Nd-Fe-B, Sm-Fe-N) ^{2,3,4}

when $(BH)_{\max}$ reached 56.7 MGOe (451kJ/m^3) on Nd-Fe-N materials^{5,6}, there has been no new breakthrough on $(BH)_{\max}$ value. To further improve the $(BH)_{\max}$, a new type of permanent magnet material, exchange-spring permanent magnets, was introduced in early 1990's, and are expected to generate giant energy product (as high as 120 MGOe)^{7,8}.

The idea of exchange-spring magnets is to make composite magnet materials consisting of two ferromagnetic coupled phases, one of which is hard phase to provide high coercivity and the other is soft phase to provide high saturation magnetization [7]. A lot of research has been done on fabricating exchange-spring type magnets. The hard phase materials that have been used include Sm-Co^{9,10,11,12,13,14,15,16,17,18}, Fe(Co)-Pt(Pd)^{19,20,21,22,23,24,25,26,27}, Nd(Sm, Pr, Zr)-Fe-B^{28,29,30,31,32,33,34,35,36,37,38}, Sm-Fe-N^{39,40}, etc. The soft phase materials are usually Fe (Co) or Fe (Co) rich material. Basically exchange-spring magnets with two different structures have been studied, one is multilayer structure^{9-13, 19-22, 28-29,41,42} and the other is nanocomposite structure^{14-18, 23-27, 30-40}.

Although a lot of effort has been put on exchange-spring magnets, significant increasing of $(BH)_{\max}$ value has not been achieved experimentally until now. The highest reported $(BH)_{\max}$ value of exchange-spring magnets is 20.1 MGOe. The problems are:

1. Crystalline anisotropies of hard phase materials are not high enough. The highest $(BH)_{\max}$ value was reached using Nd-Fe-B. However, $L1_0$ FePt and SmCo_5 both have higher crystalline anisotropy, therefore better than Nd-Fe-B⁴³.

2. The exchange coupling strength between hard and soft phases is not strong enough.

3. The volume ratio of soft phase is not maximized. In this sense, nanocomposite structure is better than multilayer structure. The reason is the maximum soft phase volume ratio in nanocomposite structure is larger than in multilayer structure.

4. The exchange-spring magnets currently fabricated are isotropic, not anisotropic.

In this chapter, the basic idea of exchange-spring magnets including a 1-D theoretical model will be introduced. Then two basic structures for the exchange-spring magnets are discussed. The advantages of anisotropic-exchange-spring magnets compared to isotropic-exchange-spring magnets are also studied.

4.2 Basic idea of exchange-spring magnets (1D model)

The basic idea of exchange-spring magnets was first introduced by Eckart F. Kneller and Reinhard Hawig⁷. They used a one-dimensional model to illustrate the idea of exchange-spring magnets, as shown in Figure 4.1.

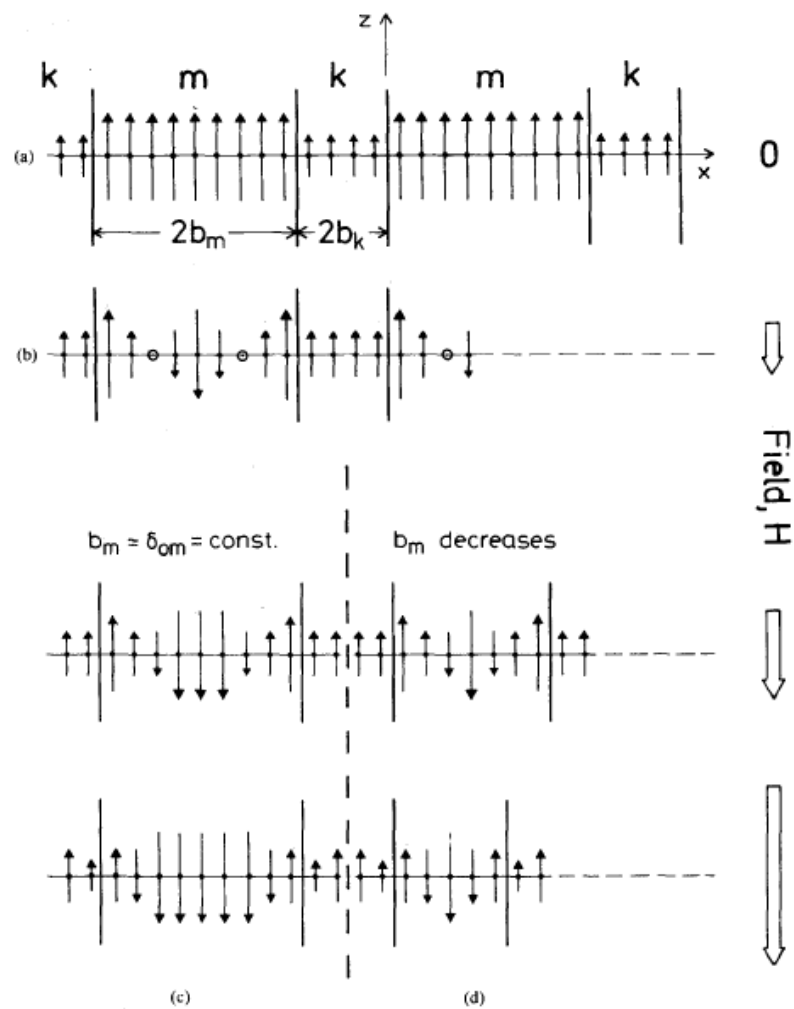


Figure 4.1 Schematic one-dimensional model of exchange-spring magnet⁷.

In their one-dimensional model, the exchange-spring magnet is defined as a composite magnetic material, consisting of two well dispersed and mutually exchange-coupled phases, one of which is a magnetic hard material providing a high nucleation field for irreversible magnetization reversal labeled as k-phase, and the other is a magnetic soft material providing a high saturation magnetization (M_s) labeled as m-phase. This composite magnetic material is expected to obtain an extremely high energy product ($(BH)_{\max}$) that can't obtained from any current permanent magnet materials.

4.2.1 Reversal process of exchange-spring magnet

The reversal process of this one-dimensional exchange-spring magnet is illustrated in Figure 4.1. Both k and m phase are assumed to have uniaxial crystalline anisotropy along Z axis. When the external magnetic field is zero, all the magnetic moments, labeled as arrows, in k and m phase are aligned in the up direction (the pre-defined uniaxial easy axis direction of both k and m phase), to minimized the crystalline anisotropy energy. The dimensions for k and m phase are defined as $2b_m$ and $2b_k$ respectively.

When an external magnetic field along negative Z axis is applied and gradually increases its magnitude, reversed moments first appeared at the center of the m phase and two domain walls are formed at the both sides of the reversed domains in

the center of m phase. The moments at the boundaries of m phase don't reverse at the first stage because of the exchange-coupling with k phase. The moments in k phase also don't reverse at the first stage because of their high crystalline anisotropy energy.

When the magnitude of the reversal magnetic field further increases, domain walls are pressed to the boundaries between m and k phase. For the moments in the domain walls, there are three energies competing, first one of which is magnetic static energy, second one of which is crystalline anisotropic energy, third one of which is exchange energy.

When the magnitude of the reversal magnetic field keeps increasing and reaches a critical value, the magnetic static energy plus the exchange energy will exceed the crystalline anisotropy energy for the moments at k phase boundaries and adjacent to the domain wall. At this situation, domain wall will begin to invade into the k phase from m phase.

After the magnitude of the reversal magnetic field reaches a sufficient large value, all the moments in both m and k phase will be fully reversed by the reversal field (saturated in negative Z direction).

From the reversal process in 1D model of exchange-spring magnet, it is clearly seen that:

1. The nucleation field and coercivity field of the exchange-spring magnets are not only determined by the properties of k and m phase such as anisotropy and exchange constants, but also determined by the dimensions of k and m phase.
2. Exchange-coupling strength between k and m phase plays an important role in the reversal process.

4.2.2 Critical dimensions of hard and soft phase

In this section, we will focus on studying the critical dimensions of hard (k) and soft (m) phases. The calculation was first performed by Eckart F. Kneller and Reinhard Hawig⁷.

Let us first look at the energy of an 180° Bloch domain wall. Assume that the total energy of 180° domain wall is E_w ⁴⁴:

$$E_w = \delta K + \delta A (\delta / \pi)^2 \quad (4.1)$$

Here δ is the wall thickness, K and A are the crystalline anisotropic and exchange constants respectively. For the equilibrium domain wall:

$$dE_w / d\delta = 0 \quad (4.2)$$

Then the equilibrium domain wall thickness is calculated from (4.2):

$$\delta_e = \pi(A / K)^{1/2} \quad (4.3)$$

The energy of the equilibrium domain wall can be calculated by using δ_e ,

$$E_{ew} = 2\pi(AK)^{1/2} \quad (4.4)$$

As we discussed in the reversal process, the critical point is when the domain wall penetrated into the k phase from m phase. Form equation (4.4), since the anisotropy constant in k phase is much larger than in m phase. Therefore the prerequisite for the domain wall penetration is that the m phase domain wall energy density reaches the equilibrium value in k phase. The increase of domain wall energy density in m phase is caused by the compression of domain wall length. Then, the prerequisite condition is:

$$E_w(m)/\delta(m) = E_{ew}(k)/\delta_e(k) \quad (4.5)$$

Assume that the crystalline anisotropy and exchange constant for hard/soft phase are K_k/K_m and A_k/A_m respectively. Then derive from (4.5):

$$K_m + A(\pi/\delta_m)^2 = 2K_k \quad (4.6)$$

Since $K_m \ll K_k$, K_m can be ignored. Therefore the critical dimension for m phase is derived from equation (4.6):

$$\delta_m^c = \pi(A_m/2K_k)^{1/2} \quad (4.7)$$

Normally, the critical dimension for k phase is taken as the equilibrium domain wall thickness of k phase:

$$\delta_k^c = \pi(A_k/K_k)^{1/2} \quad (4.8)$$

Since $A_k < A_m$ and $A_k \approx A_m$, so approximately,

$$\delta_k^c = \delta_m^c \quad (4.9)$$

4.2.3 Exchange coupling strength

In section 4.2.2, when we are calculating the critical dimensions for the m and k phase, there is an important assumption that strong exchange coupling exists at the boundary between the k and m phase.

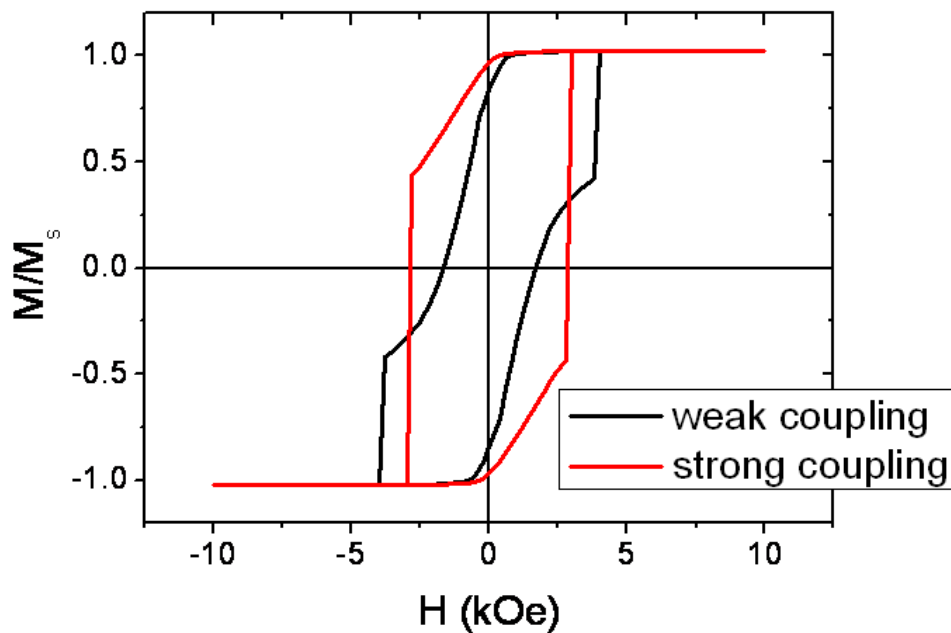


Figure 4.2 Hysteresis loops of 1D exchange-spring magnets with different exchange coupling strength.

The exchange coupling strength between k and m phase is more important for high energy product purpose, compared to the dimension requirements. Figure 4.2 calculated the hysteresis loops of a 1D exchange-spring magnet⁴⁵ with different

exchange coupling strength using OOMMF⁴⁶. It is clearly seen that strong exchange coupling yields a loop with much better squareness compared to weak exchange coupling, which corresponding to a much larger energy product.

What happens with weak exchange coupling is that the reversal of hard (k) and soft (m) phase is no longer a continuous process, but a two phase separated reversal. Because of the weak exchange coupling, the moments in the soft phase will reverse first. The domain wall in the soft phase can never penetrate into the hard phase. The hard phase will not switch until it forms a domain wall by itself. The reversal processes for the hard and soft phase are almost irrelevant. So the hysteresis loop basically is just the linear sum of two loops from hard and soft phase.

Therefore, to obtain a high energy product from the exchange-spring magnets, a fairly large exchange coupling between the hard and soft phase is extremely necessary.

4.3 Two basic structures of exchange-spring magnets

For simplicity, 1D model of exchange-spring magnets is used for theoretical considerations, which enables us to gain a clear insight view of the reversal mechanism and several critical requirements of exchange-spring magnets. However, practical 3D structures have to be studied.

Basically there are two structures for exchange-spring magnets:

1. Multilayer structure with alternative layers of hard and soft phase materials.
2. Nanocomposite structure with nano-sized hard phase materials embedding in a matrix of soft phase materials.

These two basic structures are plotted in Figure 4.3. From the aspect of fabrication difficulty of these two structures, multilayer structure is easier to fabricate and nanocomposite structure is harder. However, with the same hard and soft materials, nanocomposite structure can generate higher energy product.

From the critical dimensions of hard and soft phase calculation in section 4.2.2, equation (4.9) gives that the critical dimension of hard phase is equal to that of soft phase. If the multilayer structure is used, then the thickness of the hard phase layer should be equal to the thickness of soft phase layer, which means that the hard phase has a volume ratio of 50%.

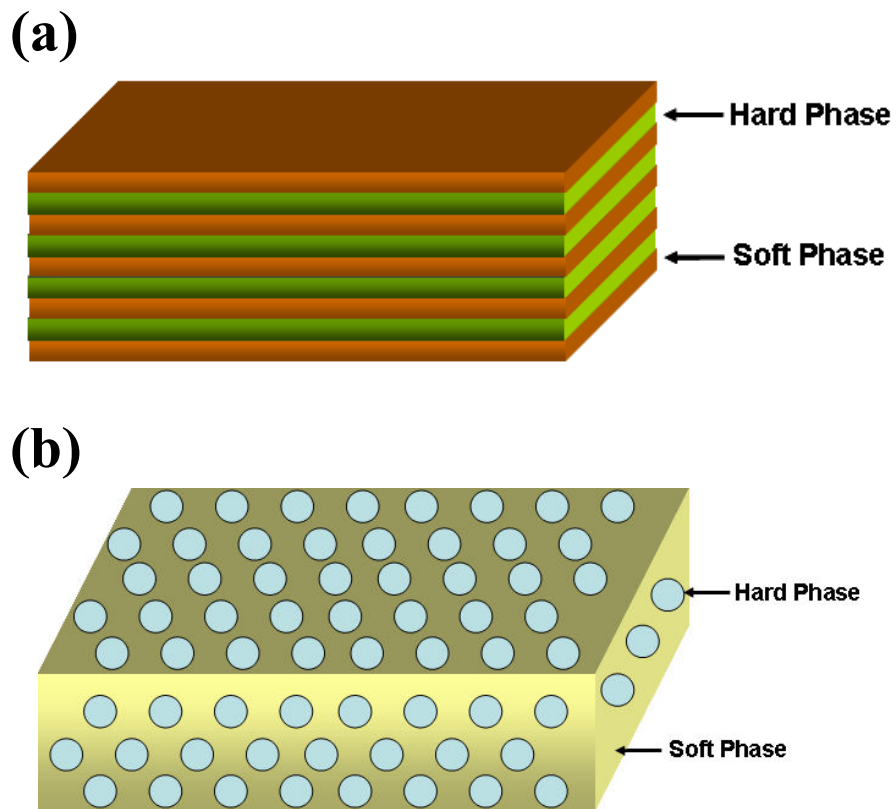


Figure 4.3 Two basic structures of exchange-spring magnets: (a) multilayer structure, (b) nanocomposite structure.

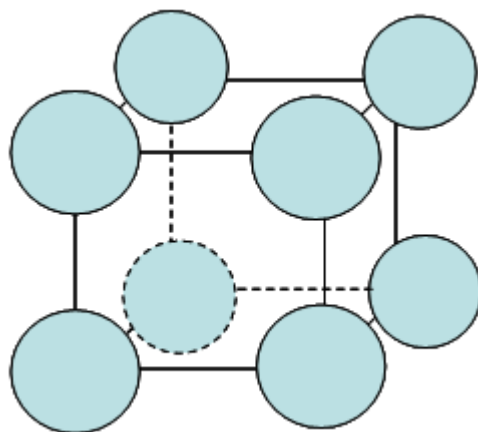


Figure 4.4 Simple cubic arrangements of hard phase particles in matrix.

But if the nanocomposite structure is used and assuming that hard phase particles uniformly distributed in the matrix and with a simple cubic lattice like arrangement, as shown in Figure 4.4, then equation (4.9) requires that the distance between any two hard phase particles is equal to the diameter of the hard phase particle. In this case, the hard phase has a volume ratio of just:

$$V_h \% = \frac{4}{3} \pi r^3 / 64r^3 = 6.5\% . \quad (4.10)$$

Therefore, to obtain the same reversal nucleation field, multilayer structure needs 50% volume of hard phase, and nanocomposite structure just needs 6.5% volume of hard phase. Considering that hard phase materials normally have lower saturation magnetization, the saturation magnetization of the exchange-spring magnets with nanocomposite structure will be much larger than the saturation magnetization of the exchange-spring magnets with multilayer structure. So the energy product of the exchange-spring magnets with nanocomposite structure will be much larger than that with multilayer structure.

Therefore, to obtain extremely high energy product, nanocomposite structure is preferred for exchange-spring magnets.

4.4 Anisotropic and isotropic exchange-spring magnets

For an exchange-spring magnet with nanocomposite structure, there is another important issue to be considered. Whether the magnet should be anisotropic or isotropic?

To clearly address this question, a simplified model is built, as shown in Figure 4.5. Assume that the exchange-spring magnet consists of many identical units and all the units have a uniaxial easy axis. For the anisotropic exchange-spring magnets, the easy axes of all the units are aligned to a single direction. For the isotropic exchange-spring magnets, the easy axes of all the units are randomly oriented.

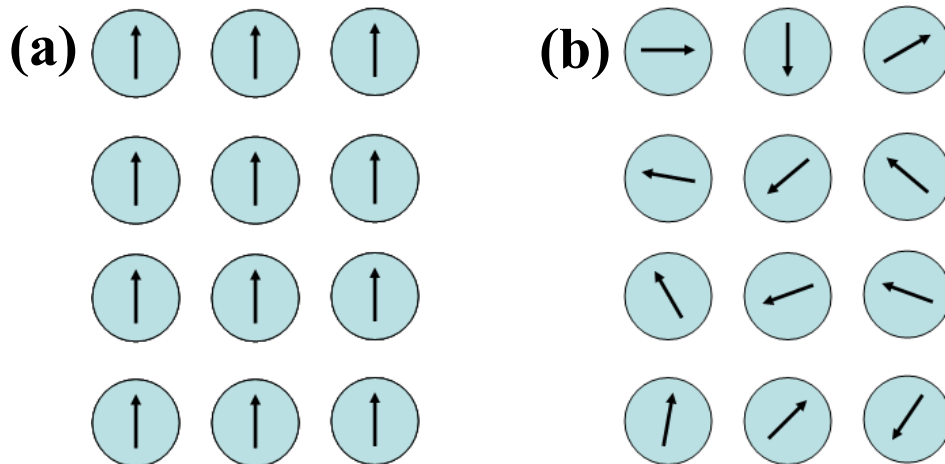


Figure 4.5 Schematic drawing for (a) anisotropic exchange-spring magnet and (b) isotropic exchange-spring magnet

Micromagnetic simulations can be used to calculate the hysteresis loops of the anisotropic and isotropic magnets. However in a very straightforward way, we can easily estimate the energy product difference between the anisotropic and isotropic magnets. Here the energy product of the anisotropic magnet is the energy product along its easy axis.

For the anisotropic magnet case, we can use the Stoner-Wohlfarth model⁴⁴ to calculate its energy product:

$$H_c = 2K / M_s \quad (4.11)$$

$$B_r = 4\pi M_s \quad (4.12)$$

So for a square loop that derived from Stoner-Wohlfarth model,

$$(BH)_{\max} = -H_c(B_r - H_c) = 4K^2 / M_s^2 - 8\pi K \quad (4.13)$$

For the isotropic magnet case, we can take every thing as same as in the anisotropic magnet case, except for the K value. Because of the randomly dispersed easy axis of the units, the effective K value for isotropic magnets is:

$$K_{\text{eff}} = \frac{\int_0^{\pi/2} K \cos \theta d\theta}{\int_0^{\pi/2} d\theta} = 2K / \pi \approx 0.64K \quad (4.14)$$

So the anisotropy K decreases 36% in the isotropic magnet compared to anisotropic. Therefore, normally the energy product $(BH)_{\max}$ of the anisotropic magnet is at least 100% larger than the isotropic magnets.

4.5 Summary

In this Chapter, we first reviewed the development of permanent magnet materials and introduced the basic ideas of the exchange-spring magnets. Then we studied the critical dimensions of the hard and soft phase. Two basic structures, multilayer structure and nanocomposite structure, were compared, and nanocomposite structure was found to be preferred for energy product enhancement. Through estimation, anisotropic exchange-spring magnets were found to have at least 100% improvement in energy product compared to isotropic exchange-spring magnets.

Reference:

- ¹ Data source: Webmagnetics (2007 Data).
- ² J.M.D. Coey, “Invited paper Perspectives in permanent magnetism”, *J. Magn. Mater.* 140-144, 1041-1044 (1995).
- ³ O Gutfleisch, “Review article Controlling the properties of high energy density permanent magnetic materials by different processing routes”, *J. Phys. D: Appl. Phys.* 33, R157-R172 (2000).
- ⁴ David Brown, Bao-Min Ma, Zhongmin Chen, “Topic review: Developments in the processing and Properties of NdFeb-type permanent magnets”, *J. Magn. Mater.* 248, 432-440 (2002).
- ⁵ K. Khlopkov, O. Gutfleisch, D. Eckert, D. Hinz, B. Wall, W. Rodewald, K. –H. Muller and L. Schultz, “Local texture in Nd-Fe-B sintered magnets with maximized energy density”, *Journal of Alloys and Compounds* 365, 259-265 (2004).
- ⁶ A. S. Kim and F. E. Camp, “High performance NdFeB magnets (invited)”, *J. Appl. Phys.* 79(8), 5035-5039 (1996).
- ⁷ Eckart F. Kneller, and Reinhard Hawig, “The exchange spring magnet: A new material principle for permanent magnets”, *IEEE Trans. on Magn.* 27(4), 3588-3600 (1991).
- ⁸ Ralph Skomski and J. M. D. Coey, “Giant energy product in nanostructured two-phase magnets”, *Phys. Rev. B* 48(21), 15812-15816 (1993).

- ⁹ I. A. Al-Omari and D. J. Sellmyer, “Magnetic properties of nanostructured CoSm/FeCo films”, *Phys. Rev. B.* 52(5), 3441 (1995)
- ¹⁰ Eric E. Fullerton, J. Samuel Jiang, C. H. Sowers, J. E. Pearson and S. D. Bader, “Structure and magnetic properties of exchange spring Sm-Co/Co superlattices”, *Appl. Phys. Lett.* 72(3), 380-382 (1998).
- ¹¹ J. S. Jiang, J. E. Pearson, Z. Y. Liu, B. Kabius, S. Trasobares, D. J. Miller, S. D. Bader, D. R. Lee, D. Haskel, G. Srajer, and J. P. Liu, “Improving exchange spring nanocomposite permanent magnets”, *Appl. Phys. Lett.*, 85(22), 5293-5295 (2004).
- ¹² J. Zhang, Y. K. Takahashi, R. Gopalan, and K. Hono, “Sm(Co, Cu)₅/Fe exchange spring multilayer films with high energy product”, *Appl. Phys. Lett.* 86, 122509 (2005).
- ¹³ V. Neu, K. Hafner, A. K. Patra and L. Schultz, “Fully epitaxial, exchange coupled SmCo₅/Fe/SmCo₅ trilayers”, *J. Phys. D: Appl. Phys.* 39, 5116-5120 (2006).
- ¹⁴ A. Yan, A. Bollero, O. Gutfleisch, and K. -H. Muller, “Microstructure and magnetization reversal in nanocomposite SmCo₅/Sm₂Co₁₇ magnets”, *J. Appl. Phys.* 91(4), 2192 (2002)
- ¹⁵ Jian Zhang, Shao-ying Zhang, Hong-wei Zhang and Bao-gen Shen, “Structure, magnetic properties and coercivity mechanism of nanocomposite SmCo₅/α-Fe magnets prepared by mechanical milling”, *J. Appl. Phys.* 89(10), 5601 (2001)

-
- ¹⁶ Q. Zeng, Y. Zhang, M. J. Bonder, G. C. Hadjipanayis, and R. Radhakrishnan, “Bulk SmCo₅/α-Fe composite by plasma pressure consolidation”, IEEE Trans. Magn. 39(5), 2974 (2003)
- ¹⁷ Yanglong Hou, Shouheng Sun, Chuanbing Rong, and J. Ping Liu, “SmCo₅/Fe nanocomposites synthesized from reductive annealing of oxide nanoparticles”, Appl. Phys. Lett. 91, 153117 (2007)
- ¹⁸ N.V. Rama Rao, R. Gopalan, M. Manivel Raja, V. Chandrasekaran, D. Chakravarty, R. Sundaresan, R. Ranganathan, K. Hono, “Structural and magnetic studies on spark plasma sintered SmCo₅/Fe bulk nanocomposite magnets”, J. Magn. Mater. 312, 252-257 (2007).
- ¹⁹ R.F. Sabiryanov, S. S. Jaswal, “Electronic structure and magnetic properties of hard/soft multilayers”, J. Magn. Mater. 177-181, 989-990(1998).
- ²⁰ Joseph E. Davies, Olav Hellwig, Eric E. Fullerton, J. S. Jiang, S. D. Bader, G. T. Zimanyi and Kai Liu, “Anisotropy dependence of irreversible switching in Fe/SmCo and FeNi/FePt exchange spring magnet films”, Appl. Phys. Lett. 86, 262503 (2005).
- ²¹ Francesca Casoli, Franca Albertini, Simone Fabbrici, Claudio Bocchi, Lucia Nasi, Roberta Ciprian and Luigi Pareti, “ Exchange coupled FePt/Fe bilayers with perpendicular magnetization”, IEEE Trans. Magn. 41(10), 3877 (2005).
- ²² Jian Zhou, Ralph Skomski, Xingzhong Li, Wei Tang, George C. Hadjipanayis and David J. Sellmyer, “ Permanent-Magnet Properties of Thermally Processed FePt and FePt-Fe Multilayer Films”, IEEE Trans. Magn. 38(5), 2802 (2002).

- ²³ Hao Zeng, Jing Li, J. P. Liu, Zhong L. Wang, and Shouheng Sun, “Exchange-coupled nanocomposite magnets by nanoparticle self-assembly”, *Nature* 420, 395 (2002)
- ²⁴ Junichi Kawanura, Kazuhisa Sato and Yoshihiko Hirotsu, “Fabrication of exchange-coupled α -Fe/L1₀-FePd nanocomposite isolated particles”, *J. Appl. Phys.* 96(7), 3906 (2004)
- ²⁵ Katayun Barmak, Jihwan Kim, Roger A. Ristau, and Laura H. Lewis, “Ferromagnetic exchange spring nanocomposites of A1+L1₀ CoPt”, *IEEE Trans. Magn. Magn.* 38(5), 2799 (2002).
- ²⁶ X. Rui, J. E. Shield, Z. Sun, Y. Xu, and D. J. Sellmyer, “In-cluster-structured exchange-coupled magnets with high energy densities”, *Appl. Phys. Lett.* 89, 122509 (2006).
- ²⁷ P. Sharma, J. Waki, N. Kaushik, D. V. Louzguine-Luzgin, H. Kimura, A. Inoue, “High coercivity characteristics of FePtB exchange-coupled nanocomposite thick film spring magnets produced by sputtering”, *Acta materialia* 55, 4203-4212 (2007)
- ²⁸ M. Shindo, M. Ishizone, H. Kato, T. Miyazaki, A. Sakuma, “Exchange spring behavior in sputter-denposited α -Fe/Nd-Fe-B multilayer magnets”, *J. Magn. Magn. Mater.* 161, L1-L5 (1996).
- ²⁹ B. Z. Cui, M. J. O’Shea, “Hard magnetic properties of rapidly annealed NdFeB/Co films and intergrain interactions”, *J. Magn. Magn. Mater.* 279, 27-35 (2004)

- ³⁰ R. Coehoorn, D. B. de Mooij, J. P. W. B. Duchateau, and K. H. J. Buschow, *J. Phys. (Paris), Colloq.* 8, 669 (1988).
- ³¹ L. Withanawasam, G. C. Hadjipanayis, R. F. Krause, “Enhanced remanence in isotropic Fe-rich melt-spun Nd-Fe-B ribbons”, *J. Appl. Phys.* 75(10), 6646 (1994).
- ³² I. Panagiotopoulos, L. Withanawasam, G. C. Hadjipanayis, “Exchange spring behavior in nanocomposite hard magnetic materials”, *J. Magn. Magn. Mater.* 152, 353-358 (1996).
- ³³ D. Goll, M. Seeger, H. Kronmüller, “Magnetic and microstructural properties of nanocrystalline exchange coupled PrFeB permanent magnets”, *J. Magn. Magn. Mater.* 185, 49-60 (1998).
- ³⁴ P. G. McCormick, W. F. Miao, P. A. I. Smith, J. Ding, R. Street, “Mechanically alloyed nanocomposite magnets (invited)”, *J. Appl. Phys.* 83(11), 6256 (1998)
- ³⁵ K. Raviprasad, M. Funakoshi, and M. Umemoto, “Synthesis and characterization of Nd₂Fe₁₄B-25% Fe nanocomposite magnets”, *J. Appl. Phys.* 83(2), 921 (1998).
- ³⁶ H. Ono, N. Waki, M. Shimada, T. Sugiyama, A. Fujiki, H. Yamamoto, “Isotropic bulk exchange spring magnets with 134kJ/m³ prepared by spark plasma sintering method”, *IEEE Trans. Magn.* 37(4), 2552 (2001)
- ³⁷ Z. C. Wang, H. A. Davies, S. Z. Zhou, M. C. Zhang and Y. Qiao, “Preparation and magnetic properties of melt-spun Nd₂Fe₁₄(BC)/ α -Fe nanocomposite magnets”, *J. Appl. Phys.* 91(10), 7884 (2002).

- ³⁸ A. M. Gabay, Y. Zhang, and G. C. Hadjipanayis, “Die-upset hybrid Pr-Fe-B nanocomposite magnets”, *Appl. Phys. Lett.* 85(3), 446 (2004).
- ³⁹ Y. Otani, A. Moukarika, Hong Sun and J. M. D. Coey, “Metal bonded $\text{Sm}_2\text{Fe}_{17}\text{N}_{3-\delta}$ magnets”, *J. Appl. Phys.*, 69(9), 6735 (1991).
- ⁴⁰ J. J. Wyslocki, P. Pawlik, W. Kaszuwara, M. Leonowicz, “Magnetic properties and intrinsic magnetic parameters of nanocrystalline Sm-Fe-N magnets”, *J. Magn. Mater.* 272-276, e1929-e1930 (2004).
- ⁴¹ T. Leineweber, H. Kronmuller, “Micromagnetic examination of exchange coupled ferromagnetic nanolayers”, *J. Magn. Mater.* 176, 145-154 (1997).
- ⁴² Matteo Amato, Angelo Rettori, Maria Gloria Pini, “Exchange-spring behavior of hard/soft magnetic multilayers: optimization study of the nanostructure”, *Phys. B* 275, 120-123 (2000).
- ⁴³ Dieter Weller, Andreas Moser, Liesl Folks, Margaret E. Best, Wen Lee, Mike F. Toney, M. Schwickert, Jan-Ulrich Thiele, and Mary F. Doerner, “High Ku materials Approach to 100 Gbits/in²”, *IEEE Trans. Magn.* 36(1), 10 (2000).
- ⁴⁴ Robert C. O’Handley, “Modern Magnetic Materials: Principles and Applications”, publisher Wiley-Interscience (1999)
- ⁴⁵ The material settings are: For m soft phase, $M_s=1.6 \times 10^6$ A/m, $A = 6 \times 10^{-12}$ J/m, $K=1 \times 10^5$ J/m³; For k hard phase, $M_s=1.6 \times 10^6$ A/m, $A = 6 \times 10^{-12}$ J/m, $K=7 \times 10^6$ J/m³. Dimensions for m and k phase are both 2 nm. For strong m and k coupling, $A =$

$6 \times 10^{-12} \text{J/m}$., for weak m and k coupling, $A = 1.2 \times 10^{-12} \text{J/m}$. Calculation settings are:

the damping coefficient used is $\alpha=0.5$, the cell size are 0.5nm .

⁴⁶ M. Donahue and D. Porter, The Object Oriented MicroMagnetic Framework (OOMMF) project at ITL/NIST, <http://math.nist.gov/oommf/>.

CHAPTER 5

SYNTHESIS OF FePt/Fe-Ni ANISOTROPIC-EXCHANGE-SPRING MAGNETS

5.1 Introduction

The improvements of the energy product of permanent magnets reached a difficult stage since the discovery of RE-TM materials (e.g. Sm-Co, Nd-Fe-B). It is more and more difficult to discover new hard materials to achieve higher energy product^{1,2,3}. Exchange-spring magnet is a new generation of permanent magnets materials which is expected to set new record for the energy product value of permanent magnets^{4,5,6}. It is a composite material which contains two exchange-coupled magnetic phases, one is soft phase and the other is hard phase⁴. These two exchange-coupled magnetic phases have the ability to preserve high

magnetization and coercivity simultaneously, therefore greatly enhance the energy product (theoretically 170% increases to current energy product record value^{5,7}).

Although exchange-spring magnets are convenient to realize in multi-layer structure^{8,9,10,11,12,13,14,15,16,17,18}, calculation results show that nanocomposite structure has more potential to render ultrahigh energy product^{2,19}. To maintain the high magnetization and coercivity, the grain sizes of both hard and soft phases in the nanocomposite needs to be in order of 10 nm^{4,5,6}. Therefore special chemical processes are developed and isotropic nanocomposites have been fabricated^{20,21}.

Anisotropic nanocomposite can further enhance the energy product (124% increases in our case) by further increasing the magnetization remanence and coercivity on the base of isotropic nanocomposites. For chemical methods, magnetic hard and soft phase are formed through chemical reaction and completely mixed during the synthesis process, which lead to the difficulties in further controlling the nanostructures in the composites, such as the easy-axis orientation control of hard phase which is essential for fabrication of anisotropic nanocomposites.

In this Chapter, we report a novel gas phase approach that fabricates the hard and soft phase independently and greatly increases the flexibility in further controlling the nanostructures. Using this technique, anisotropic exchange-spring nanocomposites are successfully fabricated for the first time. For demonstration, we picked the model system FePt/Fe-Ni. L1₀ magnetic hard FePt nanoparticles are

embedded into a Fe-Ni magnetic soft matrix. The hard and soft phase materials are exchange coupled and have controlled easy and hard directions.

5.2 Fabrication process

The fabrication system consists of a magnetron sputtering based gas phase nanoparticle deposition source and a conventional thin film sputtering gun. As shown in Figure 1 (a), the gas phase nanoparticle deposition source is located on the left hand side and the matrix sputtering gun is installed in the substrate chamber on the right hand side. The nanoparticle deposition source points directly to the substrate while the matrix sputtering gun is located about 30 degree relative to the perpendicular direction of the substrate plane.

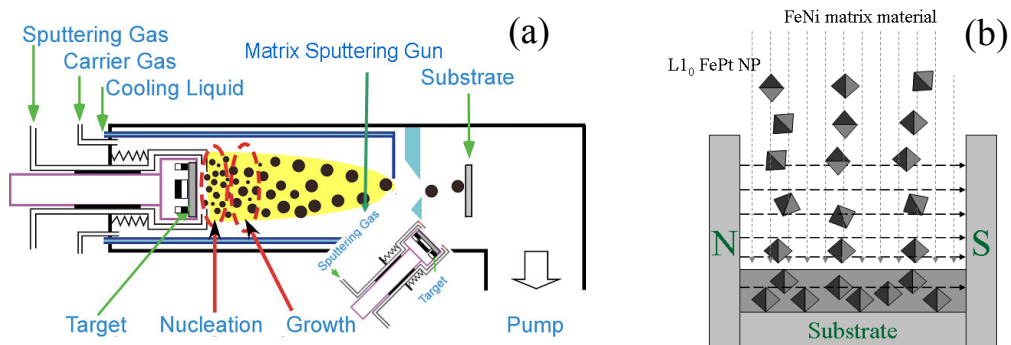


Figure 5.1 (a) Anisotropic exchange-spring nanocomposites fabrication system, (b) illustration of the easy-axis field alignment process.

The base pressure of the system was 4×10^{-8} Torr. A $\text{Fe}_{0.5}\text{Pt}_{0.5}$ target was used for the fabrication of FePt nanoparticles. The working pressure of the nanoparticle source chamber was kept at 410~420 mTorr by a total Ar gas flow of 16.5 sccm. The sputtering voltage and current used for the nanoparticle source were 288 V and 0.60 A respectively. Monodispersed and gas phase directly ordered $L1_0$ FePt nanoparticles with controllable sizes were formed in the nanoparticle source chamber and carried to the substrate by Ar gas flow^{22, 23}. In the substrate chamber, the working pressure was kept at about 7 mTorr by an Ar gas flow of 15 sccm. The matrix sputtering gun used a $\text{Fe}_{0.8}\text{Ni}_{0.2}$ target and deposited Fe-Ni matrix materials on the substrate with $L1_0$ FePt nanoparticles simultaneously. The sputtering voltage and current used for the matrix sputtering gun were 464 V and 0.20 A respectively. In this study, 25nm thick nanocomposite films were deposited on surface oxidized Si wafer. $L1_0$ FePt nanoparticles with average size of $5.8(1 \pm 0.11)$ nm were used as hard phase¹⁸. The volume ratio of $L1_0$ FePt nanoparticles in the nanocomposite films was 33%, calculated from deposition rates. To define the easy axis of the FePt/Fe-Ni nanocomposites, a 5 kOe external field was applied parallel to the substrate plane by a pair of permanent magnets as shown in Figure 1(b). Randomly oriented FePt nanoparticles were magnetized in the Ar gas flow and rotated their easy axis (001) towards the external field's direction until they reached the substrate²⁴. Therefore an

in-plane easy axis of the FePt/Fe-Ni nanocomposite was defined along the external field's direction and an in-plane hard axis perpendicular to the external field's direction.

5.3 Microstructure

5.3.1 Shape and magnetic properties of L1₀ FePt nanoparticles

Figure 5.2 (a) and (b) shows dominated shape of 5.8 nm L1₀ FePt nanoparticles and its schematic drawing. The shape is octahedron with 8 (111) facets. L1₀ FePt nanoparticles have a uniaxial easy axis along (001) direction, which pointing from one corner of the octahedron to the opposite corner, as shown in Figure 5.2 (a). The large coercivity (figure 5.2 (c), 35 kOe at 5K) indicates that the FePt nanoparticles are in magnetic hard phase. Detailed information about the gas phase fabrication of L1₀ FePt nanoparticles are reported in reference 22 and 23.

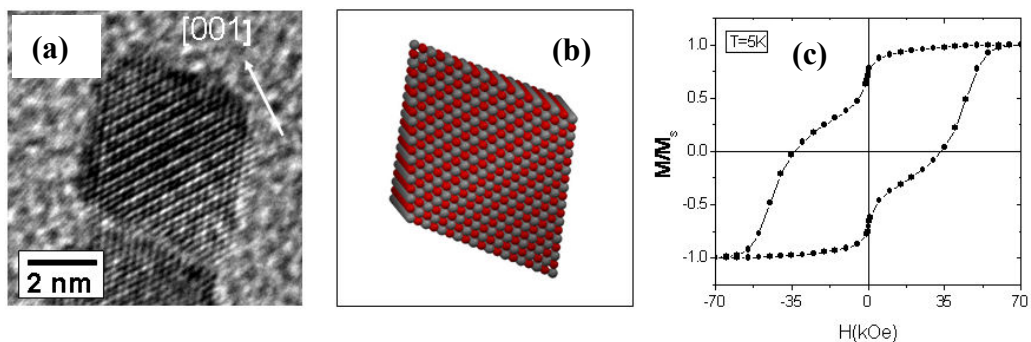


Figure 5.2 (a) Dominated shape of 5.8 nm L1₀ FePt nanoparticles and (b) its schematic drawing. (c) The magnetic hysteresis loop of 5.8 nm L1₀ FePt nanoparticles.

5.3.2 Nanocomposite film characterization

Large scale TEM cross section picture of FePt/Fe-Ni anisotropic nanocomposites is shown in Figure 5.3. The thickness of the nanocomposite film is about 25 nm. SiO₂ and Si layers in the substrate are also clearly observed.

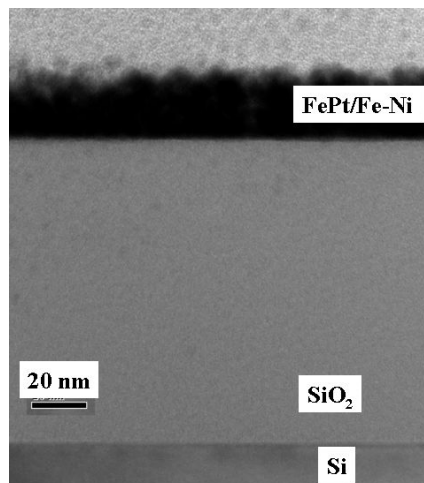


Figure 5.3 cross section TEM image of the FePt/Fe-Ni anisotropic nanocomposite.

Figure 5.4 shows the X-ray diffraction (XRD) pattern of the FePt/Fe-Ni anisotropic nanocomposites. FeNi (110) and FeNi(111) peaks and FePt (220) and (002) peaks are clearly observed. This result indicates that FeNi matrix has a

polycrystalline structure and the easy axes of FePt nanoparticles are not 100% aligned, which will be discussed in next section. Besides the FePt and FeNi lattice diffraction peaks, Si and SiO₂ lattice diffraction pattern are also observed, which comes from the surface oxidized Si substrate.

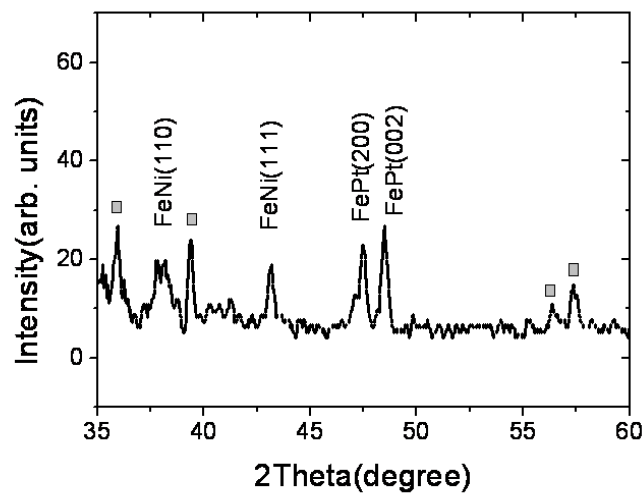


Figure 5.4 XRD pattern of the FePt/Fe-Ni anisotropic nanocomposite. (SiO₂ peaks, labeled with small squares, from left to right are SiO₂ (220), (310), (330) and (331) respectively).

5.3.3 In-plane easy axis alignment

As described in the fabrication process, an external magnetic field is applied to align the easy axes of L1₀ FePt nanoparticles in the nanocomposite film. Since L1₀ FePt nanoparticles have a uniaxial easy axis along their (001) direction, the expected

microstructure of the FePt/Fe-Ni exchange-spring magnets should be same structure shown in Figure 5.5.

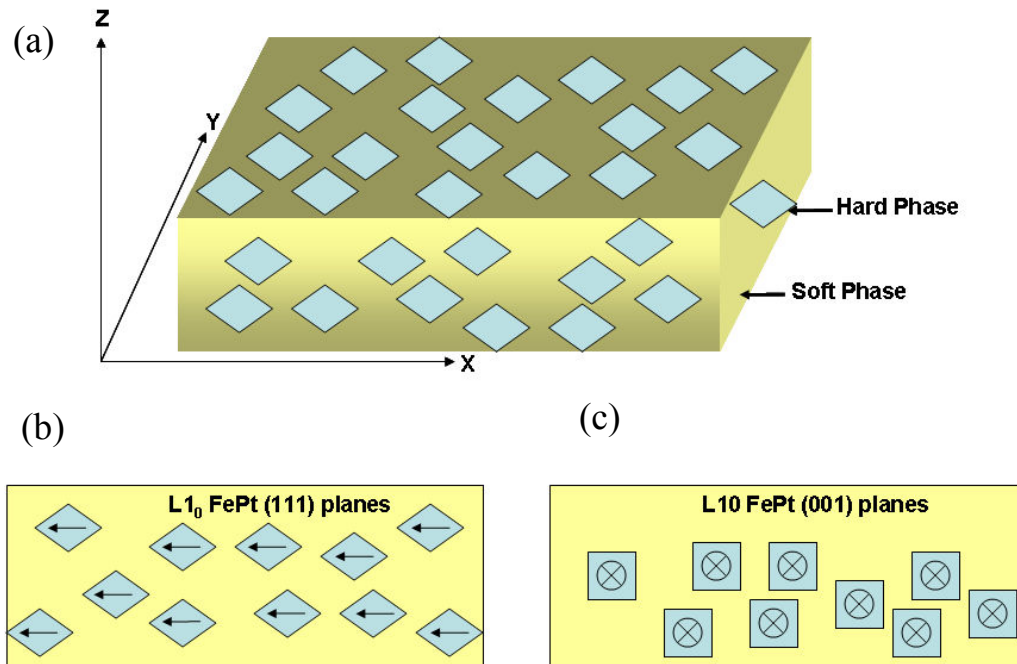


Figure 5.5 Schematic drawing of (a) 3D view FePt/Fe-Ni anisotropic exchange-spring magnets, (b) cross section view of XY plane and (c) cross-section view of YZ plane.

All the embedded octahedron shape $L1_0$ FePt nanoparticles should have their (001) direction lying in the XY plane, as shown in Figure 5.5 (a). If high resolution transmission electron microscopy (HRTEM) cross section pictures of the FePt/Fe-Ni exchange-spring magnets are captured in XY or XZ plane, then all the easy axes of $L1_0$ FePt nanoparticles should lie in the paper plane and point to an aligned direction.

Only (111) crystalline planes of $L1_0$ FePt nanoparticles can be observed, as shown in Figure 5.5(b). If HRTEM cross section pictures of the FePt/Fe-Ni exchange-spring magnets are captured in YZ plane, then all the easy axes of $L1_0$ FePt nanoparticles should lie perpendicular to the paper plane. Only (001) crystalline planes of $L1_0$ FePt nanoparticles can be observed, as shown in Figure 5.5(c).

The experimental in-plane easy axis alignment results are characterized by high resolution transmission electron microscopy (HRTEM). Figure 5.6 (a) is the cross section picture of the anisotropic nanocomposite. The cross section was obtained by cutting perpendicular to the easy axis. It is observed that the picture contains two regions with different crystal structure, one with lattice fringe distance of 0.197nm corresponding to fct structured FePt (200) and (020) planes, the other with lattice fringe distance of 0.178nm and 0.209nm corresponding to fcc structured FeNi (200) and (111) planes. The corresponding diffraction spots of the FePt and FeNi planes are also observed in the diffraction pattern of the cross section TEM sample (figure 5.6 (b)).

The observation of FePt (200) and (020) planes parallel to the easy axis proves that the (001) axis of FePt nanoparticles are successfully aligned to the defined easy axis. The plane view TEM picture (Figure 5.6(c)) also shows that the corners of FePt nanoparticles are aligned pointing to the left. In Figure 5.6 (d), the appearance of FePt (110) diffraction pattern proves that the FePt nanoparticles are in $L1_0$ magnetic hard phase.

The experimental results shown in Figure 5.6 exactly match the designed results shown in Figure 5.5, which proves the effectiveness of the easy axis alignment of the FePt/Fe-Ni anisotropic exchange-spring magnets.

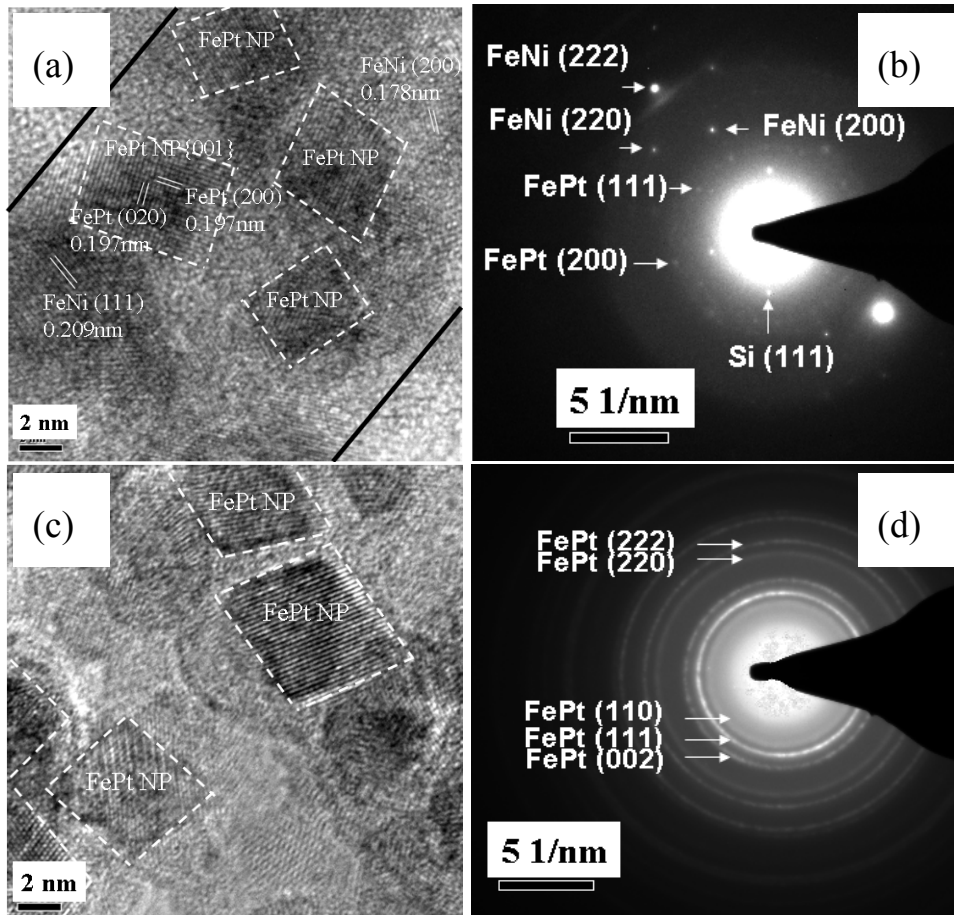


Figure 5.6 (a) YZ plane cross-section HRTEM pictures of the FePt/Fe-Ni anisotropic nanocomposites and (b) its corresponding diffraction pattern. (c) XY plane cross-section view HRTEM pictures of the FePt/Fe-Ni anisotropic nanocomposites and (d) its corresponding diffraction pattern.

To preparing the TEM plane view sample, SiO₂/Si substrate needs to be removed. A mechanical milling followed by long time ion milling process was performed. The FePt/Fe-Ni layer was also reduced to less than 10nm in the final state. Therefore FeNi matrix materials were seriously damaged during the ion milling process. This causes the diffraction patterns from FeNi matrix not clearly observed in Figure 5.6 (d).

5.4 Magnetic properties

Figure 5.7(a) shows the hysteresis loops of the anisotropic FePt/Fe-Ni nanocomposite measured at 5K. Along the defined easy-axis direction, the nanocomposite has a coercivity of 4.5 kOe, while the coercivity along hard-axis

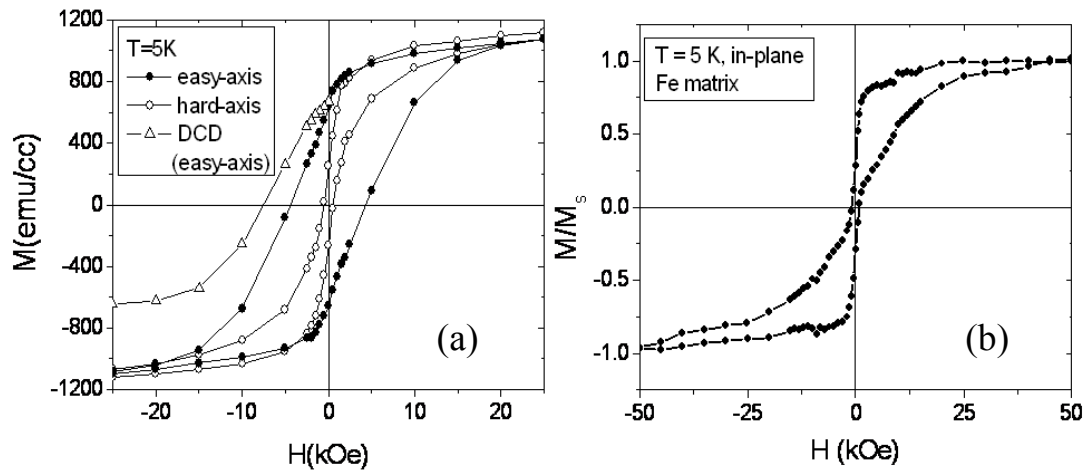


Figure 5.7 Magnetic properties of (a) anisotropic FePt/Fe-Ni nanocomposite, (b) FePt/Fe exchange decoupled nanocomposite.

is only 0.5 kOe. This result clearly shows that the FePt/Fe-Ni nanocomposites are anisotropic and ferromagnetic. The hysteresis loops and DCD curve in the moment

switching area show smooth one-step transition property, which indicates the hard and soft phases in the FePt/Fe-Ni nanocomposites are exchange coupled. Compare the hard and soft phases exchange decoupled FePt/Fe nanocomposite case, which is shown in Figure 5.7 (b), the hysteresis loop clearly shows two-step transition in the moment switching process, first step at zero field and second step at around 10 kOe. The exchange decoupling in FePt/Fe nanocomposite is caused by the large lattice mismatch between fct FePt and bcc Fe crystal structures.

Distributions of switching field ($H_{sw}=dM/dH$) and remanence switching field ($H_{swr}=dM_r/dH$) in easy-axis are showed in Figure 5.8 (a) and (b), which are calculated from the measured hysteresis loop and dc demagnetization curve (DCD) (Figure 5.7 (a)) respectively. Single distribution peak is observed in both the H_{sw} and H_{swr} distributions, which indicates the hard and soft phases in the FePt/Fe-Ni nanocomposites are exchange coupled. However the relatively wide peak spread reveals that the hard and soft phase exchange coupling is relatively weak, which could be caused by the rough contacts between two phases.

Recoil loops are normally used to characterize the exchange coupled two-phase structure^{25, 26}. Figure 5.9 (a) shows a group of recoil loops of the anisotropic FePt/Fe-Ni nanocomposite. Slightly open and fair steep recoil loops are observed, which indicates the existing of an exchange coupled two-phase structure in the nanocomposite¹⁷.

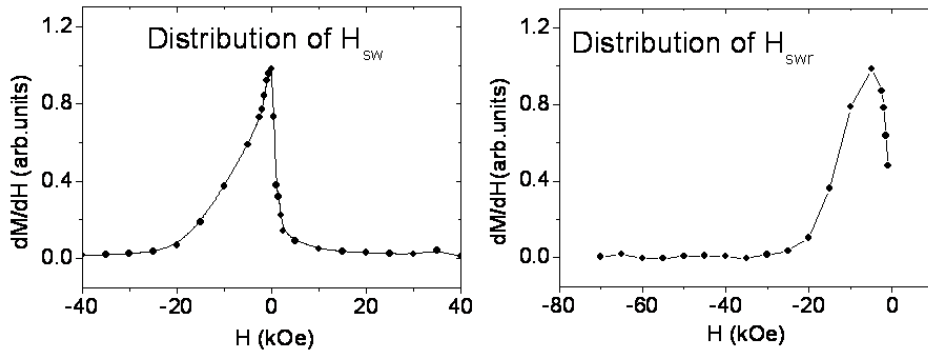


Figure 5.8 Distributions of (a) H_{SW} and (b) H_{SWR} .

To further evidence the existence of the exchange coupling in the anisotropic FePt/Fe-Ni nanocomposites, δM -H curve is measured²⁷. Here the δM is defined as $\delta M = M_d - (1 - 2M_r)$, where M_d is the dc demagnetization remanence and M_r is the isothermal remanence (both are in unit of saturation magnetization). So δM represents the deviation from the Wohlfarth relation ($M_d = 1 - 2M_r$)²⁸, which are caused by interactions. As plotted in Figure 5.9 (b), δM first has high positive value at around the coercivity field (4.5 kOe) which reveals the presence of an exchange coupling interaction during the magnetization switching of the anisotropic FePt/Fe-Ni nanocomposites. Then δM suddenly drops to negative values in the 10-20 kOe region which suggests that magnetostatic interaction is dominant after the magnetization switching.

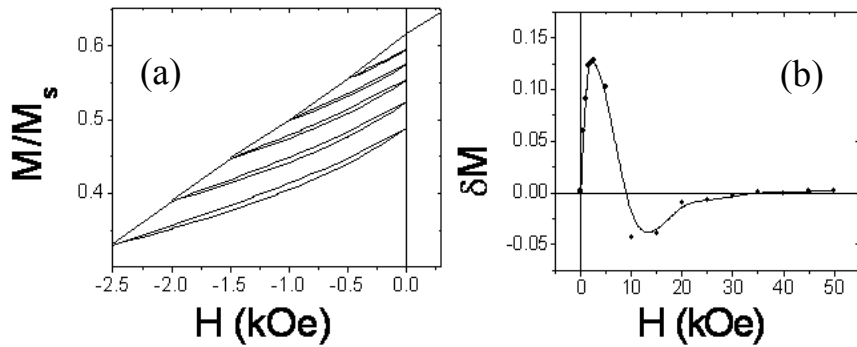


Figure 5.9 (a) Recoil loops and δM -H curve of FePt/Fe-Ni anisotropic nanocomposites.

This δM behavior is similar to the results that were reported in isotropic nanocomposites²¹. The study of recoil loops and δM curve further evidence the exchange coupling between the hard and soft phase in the anisotropic FePt/Fe-Ni nanocomposites.

The relatively wide positive peak spread in δM curve reveals that the hard and soft phase exchange coupling is relatively weak, which could be caused by the rough contacts between two phases. This weak exchange coupling with the small hard phase volume ratio (33%) limit the energy product to be only 5 MGOe at 5K (3.9 MGOe at room temperature). However the energy product of anisotropic exchange-spring magnets has huge room to improve.

5.5 Anisotropic vs. isotropic exchange-spring magnets

To study the energy product improvement of anisotropic nanocomposites compare to isotropic nanocomposites, the hysteresis loops of anisotropic and exchange coupled isotropic FePt/Fe-Ni nanocomposite (without easy-axis alignment during fabrication) are shown in figure 5.10.

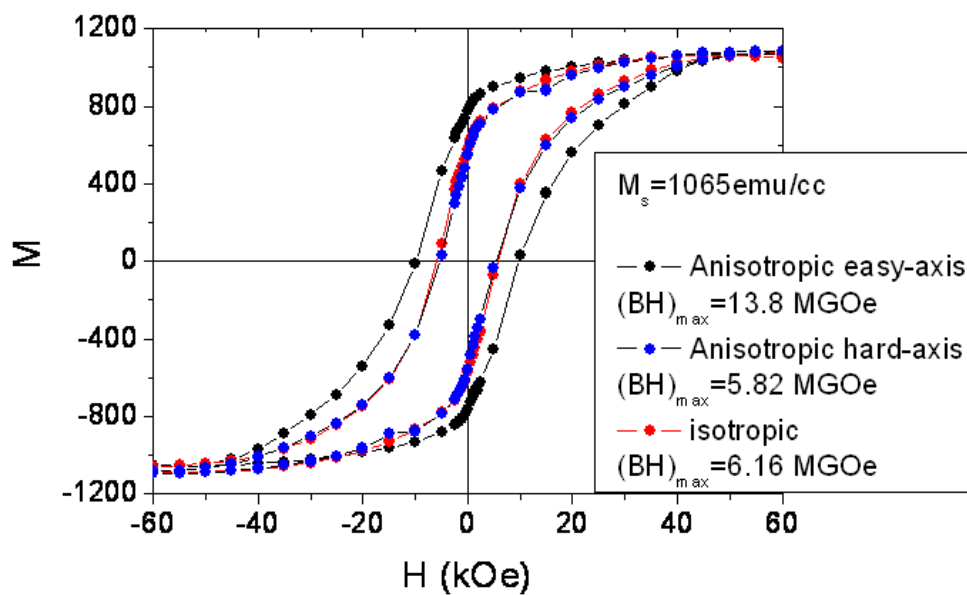


Figure 5.10 Hysteresis loops of anisotropic and isotropic FePt/Fe-Ni exchange-spring magnets.

The hysteresis loop of isotropic FePt/Fe-Ni nanocomposite measured in one random in-plane direction shows no difference to the loop measured in another in-plane direction but 90° to the first direction. This result proves that without easy-axis alignment, the nanocomposites are isotropic. Compare the anisotropic and isotropic cases, along the easy-axis, coercivity increases from 6 kOe to 10 kOe, magnetization remanence (M_r/M_s) increases from 0.55 to 0.74, the energy product increases from 6.16 MGOe to 13.8 MGOe. Therefore a 124% energy product improvement is achieved by making the FePt/Fe-Ni nanocomposite anisotropic from isotropic. Along the hard axis of the anisotropic magnets, the coercivity, magnetization remanence and energy product are very close but a little smaller than the values of the isotropic magnets, as shown in Figure 5.10.

For the anisotropic exchange-spring magnet shown in Figure 5.10, larger coercivity (10 kOe to 4.5 kOe), magnetization remanence (0.74 to 0.65) and energy product (13.8 MGOe to 5.0 MGOe) are achieved compared to the anisotropic magnet shown in Figure 5.7 (a). This improvement is achieved by increase the hardness (chemical ordering) of the $L1_0$ FePt nanoparticles. The ordering parameter for the FePt nanoparticles in Figure 5.10 is about 85%, compared to the 70% ordering parameter of the FePt nanoparticles in Figure 5.7 (a). The ordering parameters are estimated from the ordering parameter dependence of FePt anisotropy constant^{29, 30}. This result clearly shows the importance of the properties of the hard phase in the exchange-spring magnets.

5.6 Hard phase volume effect

From the theoretical model described in chapter 4, it is clear seen that the magnetic properties of the anisotropic-exchange-spring magnets heavily depend on the volume ratio, size and hardness of the hard phase. In this study, 6 nm $L1_0$ FePt nanoparticles are used as the hard phase, which satisfy the minimum hard phase size requirement. Therefore, studies focused on the hard phase volume ratio and hardness effect are performed in the section.

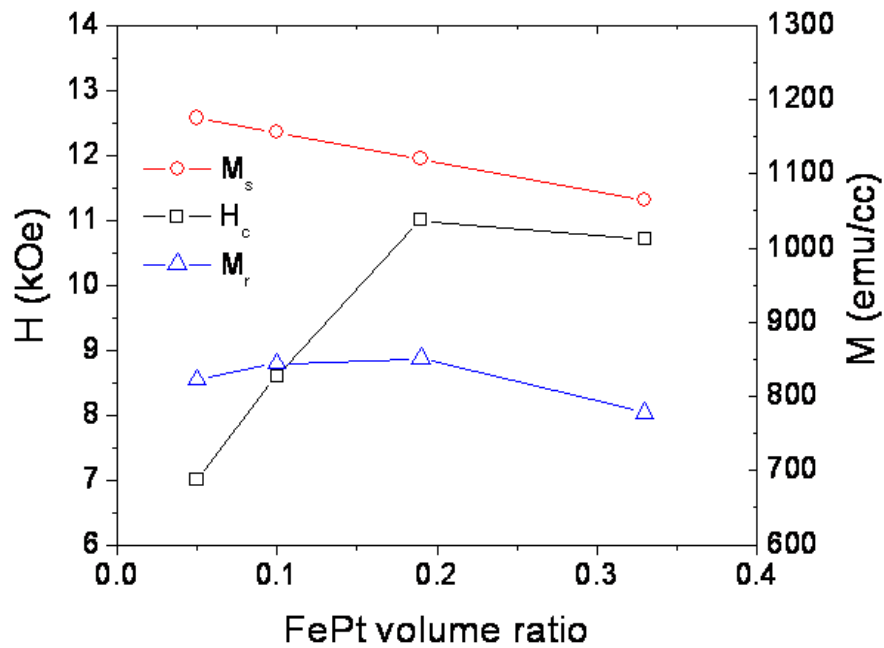


Figure 5.11 Coercivity (H_c), saturation magnetization (M_s) and magnetization remanence (M_r) as functions of $L1_0$ FePt volume ratio in the FePt/Fe-Ni anisotropic exchange-spring nanocomposites.

Figure 5.11 shows the coercivity (H_c), saturation magnetization (M_s) and magnetization remanence (M_r) as functions of $L1_0$ FePt volume ratio in the FePt/Fe-Ni anisotropic exchange-spring nanocomposites. As shown in Figure 5.11, the coercivity (H_c) first linearly increases following the increase of FePt volume ratio and then reaches a saturation value around 11 kOe when FePt volume ratio is about 19%. Following the increase of FePt volume ratio, the saturation magnetization (M_s) linearly decreases, however the magnetization remanence (M_r) first increases and then decreases.

These results are very reasonable based on the theoretical model of the exchange-spring magnets. When hard phase volume ratio is smaller than 20%, the coercivity will increase following the increase of hard phase volume ratio, which is easy to understand. However when the hard phase volume ratio further increases, the improvement of coercivity will become slow and eventually close to the coercive field of single hard phase. The linear decreasing of saturation magnetization (M_s) with increase of hard phase volume ratio is because hard phase has smaller magnetization value compared to soft phase. Therefore more hard phases included in the magnets cause smaller saturation magnetization (M_s). The changes of magnetization remanence (M_r) are caused by the competition between the nucleation field and saturation magnetization. The nucleation field increases but the saturation magnetization decreases with the increase of the hard phase volume. The result is

the magnetization remanence (M_r) first increases and then decreases with increase of hard phase volume ratio.

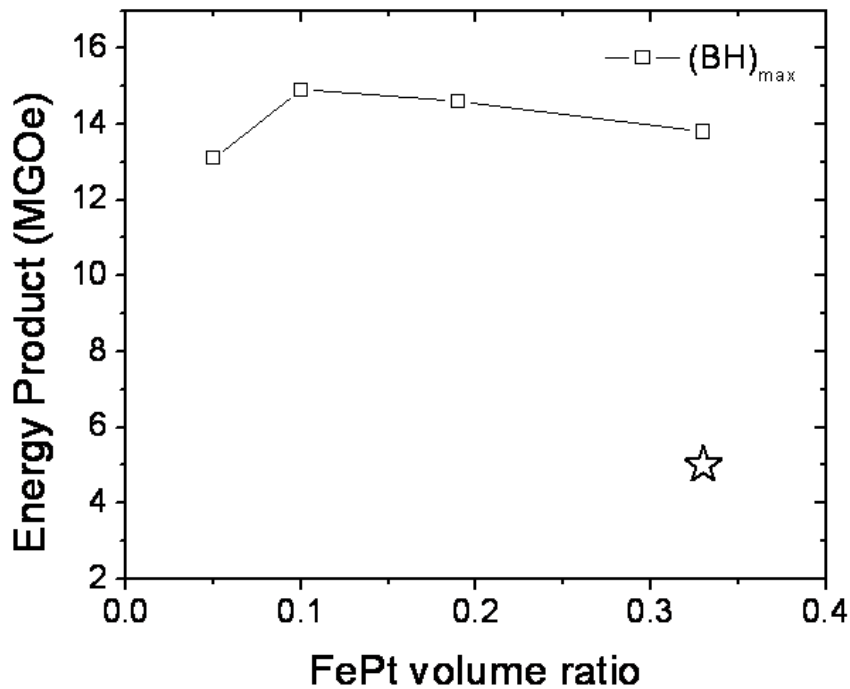


Figure 5.12 Energy product $(BH)_{\max}$ as a function of $L1_0$ FePt volume ratio in the FePt/Fe-Ni anisotropic exchange-spring nanocomposites. Exchange-spring magnets using $L1_0$ FePt nanoparticles with different ordering parameters, 85% are labeled with square marks and 70% are labeled with star mark.

Figure 5.12 shows the energy product $(BH)_{\max}$ as a function of $L1_0$ FePt hard phase volume ratio, where energy product $(BH)_{\max}$ first increases and then decreases with the increase of the hard phase volume ratio. This is a trade-off effect. The increase of the hard phase volume ratio increases the coercivity field but decreases

the saturation magnetization. Energy product $(BH)_{\max}$ reaches its maximum value of 15 MGOe when the FePt hard phase volume ratio is about 10%, which agrees well with the theoretical estimations^{4,5}.

Figure 5.12 also compares the energy product values of the exchange-spring magnets using $L1_0$ FePt nanoparticles with different ordering parameters, 85% labeled with square marks and 70% labeled with star mark. A 180% enhancement of the energy product is achieved by singly increasing the chemical ordering of FePt nanoparticles from 70% to 85%, which shows the importance of the hardness of the FePt hard phase.

5.7 Experimental result versus theoretical calculation

As shown in last section, an energy product of 15 MGOe is achieved in FePt/Fe-Ni anisotropic exchange-spring magnets with about 10% FePt volume ratio. Theoretically the highest energy product value in this FePt/Fe-Ni system can be calculated by the following equation⁵:

$$(\text{BH})_{\text{max}} = \frac{\mu_0 M_s^2}{4} \left[1 - \frac{\mu_0 (M_s - M_h) M_s}{2K_h} \right] \quad (5.1)$$

Here the M_s and M_h are the saturation magnetization of the soft and hard phase, which are 1.5 T and 1.0 T respectively. K_h is the anisotropy value of the hard phase, which is 7 MJ/m³.

The theoretical highest energy product is calculated to be 45 MGOe (360 kJ/m³), which is larger than the experimental result (15 MGOe) by a factor of 3.

The gap between the theoretical value and experimental result is caused by following factors:

1. Not fully aligned FePt easy axis. Only about 70% of the FePt nanoparticles are aligned by the external field, which gives a factor of 1.2 (based on the calculation in section 4.4).
2. Non uniformity of the FePt nanoparticles in the composite film. The remanence of magnetization is only about 0.75, which gives a factor of 1.3.

3. The hardness of the FePt nanoparticles. The anisotropy of the FePt nanoparticles is just about 3.5×10^7 erg/cc (3.5 MJ/m^3), just about half of the value of bulk FePt materials. This gives a factor of about 2.

Combine point 1-3, a total factor of $1.2 \times 1.3 \times 2 = 3.1 \approx 3 = 45 \text{ MGOe}/15 \text{ MGOe}$ is obtained. Therefore points 1-3 explains the gap between the theoretical value and experimental result.

5.8 Summary

In summary, the synthesis of anisotropic exchange-spring nanocomposites is successfully demonstrated for the first time using a novel sputtering technique on FePt/Fe-Ni system. The anisotropic nanocomposite achieved a 124% gain in energy product compared to isotropic case. Experimental result shows that only 10% (volume ratio) of FePt nanoparticles is required to achieve an optimized energy product value. This technique can be generally applied to fabricate anisotropic exchange-spring nanocomposites with various hard and soft magnetic materials, which will eventually break the permanent magnet's energy product record.

Reference:

- ¹ J.M.D. Coey, *J. Magn. Magn. Mater.* 140-144, 1041-1044 (1995)
- ² O Gutfleisch, *J. Phys. D: Appl. Phys.* 33, R157-R172 (2000)
- ³ David Brown, Bao-Min Ma, Zhongmin Chen, *J. Magn. Magn. Mater.* 248, 432-440 (2002)
- ⁴ Eckart F. Kneller and Reinhard Hawig, *IEEE Trans. Magn.* 27(4), 3588 (1991)
- ⁵ Ralph Skomski and J. M. D. Coey, *Phys. Rev. B* 48(21), 15812 (1993)
- ⁶ T. Schrefl, H. Kronmüller, and J. Fidler, *J. Magn. Magn. Mater.* 127, L273 (1993)
- ⁷ K. Khlopkov, O. Gutfleisch, D. Eckert, D. Hinz, B. Wall, W. Rodewald, K. –H. Muller and L. Schultz, “Local texture in Nd-Fe-B sintered magnets with maximized energy density”, *Journal of Alloys and Compounds* 365, 259-265 (2004)
- ⁸ I. A. Al-Omari and D. J. Sellmyer, *Phys. Rev. B.* 52(5), 3441 (1995)
- ⁹ Eric E. Fullerton, J. Samuel Jiang, C. H. Sowers, J. E. Pearson and S. D. Bader, *Appl. Phys. Lett.* 72(3), 380-382 (1998)
- ¹⁰ J. S. Jiang, J. E. Pearson, Z. Y. Liu, B. Kabius, S. Trasobares, D. J. Miller, S. D. Bader, D. R. Lee, D. Haskel, G. Srajer, and J. P. Liu, *Appl. Phys. Lett.*, 85(22), 5293-5295 (2004)
- ¹¹ J. Zhang, Y. K. Takahashi, R. Gopalan, and K. Hono, *Appl. Phys. Lett.* 86, 122509 (2005)

- ¹² V. Neu, K. Hafner, A. K. Patra and L. Schultz, *J. Phys. D: Appl. Phys.* 39, 5116-5120 (2006)
- ¹³ R.F. Sabiryanov, S. S. Jaswal, *J. Magn. Magn. Mater.* 177-181, 989-990(1998).
- ¹⁴ Joseph E. Davies, Olav Hellwig, Eric E. Fullerton, J. S. Jiang, S. D. Bader, G. T. Zimanyi and Kai Liu, *Appl. Phys. Lett.* 86, 262503 (2005).
- ¹⁵ Francesca Casoli, Franca Albertini, Simone Fabbri, Claudio Bocchi, Lucia Nasi, Roberta Ciprian and Luigi Pareti, *IEEE Trans. Magn.* 41(10), 3877 (2005).
- ¹⁶ Jian Zhou, Ralph Skomski, Xingzhong Li, Wei Tang, George C. Hadjipanayis and David J. Sellmyer, *IEEE Trans. Magn.* 38(5), 2802 (2002)
- ¹⁷ M. Shindo, M. Ishizone, H. Kato, T. Miyazaki, A. Sakuma, *J. Magn. Magn. Mater.* 161, L1-L5 (1996)
- ¹⁸ B. Z. Cui, M. J. O'Shea, *J. Magn. Magn. Mater.* 279, 27-35 (2004)
- ¹⁹ Matteo Amato, Angelo Rettori, Maria Gloria Pini, *Phys. B* 275, 120-123 (2000)
- ²⁰ Hao Zeng, Jing Li, J. P. Liu, Zhong L. Wang, and Shouheng Sun, *Nature* 420, 395 (2002)
- ²¹ Yanglong Hou, Shouheng Sun, Chuanbing Rong, and J. Ping Liu, *Appl. Phys. Lett.* 91, 153117 (2007)
- ²² J. M. Qiu and J. P. Wang, *Appl. Phys. Lett.* 88, 192505 (2006)
- ²³ Xiaoqi Liu and J. P. Wang, *J. Appl. Phys.* 105, 07A722 (2009)
- ²⁴ J. M. Qiu and J. P. Wang, *Appl. Phys. Lett.* 89, 222506 (2006)
- ²⁵ C.Rong, Yuzi Liu and J. P. Liu, *Appl. Phys. Lett.* 93, 042508 (2008)

²⁶ C. Rong and J. P. Liu, *Appl. Phys. Lett.* 94, 172510 (2009)

²⁷ P. E. Kelly, K. O'Grady, P. I. Mayo, and R. W. Chantrell, *IEEE Trans. Magn.* 25, 3881 (1989)

²⁸ E P Wohlfarth, *J. Appl. Phys.*, 29, 598, (1958)

²⁹ Okamoto S, et al, *Phys. Rev. B*, 66, 024413 (2002)

³⁰ J B Staunton, et al, *J. Phys.: Condens. Matter*, 16, S5623–S5631 (2004)

CHAPTER 6

CONCLUSIONS AND PERSPECTIVES

6.1 Conclusions

In this study, we developed a novel gas phase synthesis process for magnetic nanocomposite materials, which fabricating the different materials independently in the nanocomposite to obtain great flexibility of material manipulation.

Magnetic nanoparticle (nanocluster) is the most basic and most important component of the magnetic nanocomposite materials. Therefore we systematically studied the gas phase nanoparticle (nanocluster) synthesis theoretically and experimentally. Based on the energy control theory of nanoparticle (nanocluster) formation, we are able to control the size and phase of $L1_0$ FePt nanoparticles simultaneously. This technology can be generally applied to fabricate nanoparticles in all other material system.

Study on one important application of magnetic nanocomposites, exchange-spring magnets, was also performed. Major issues in exchange-spring magnets such as structures, critical dimensions and exchange coupling strength were discussed. Anisotropic exchange-spring magnets with nanocomposite structure were found to be preferred for extremely high energy products.

Finally, the fabrication of practical FePt/Fe-Ni anisotropic exchange-spring magnets were successfully demonstrated using our novel gas phase magnetic nanocomposite synthesis process.

6.2 Perspectives

Although great achievements are realized by the gas phase magnetic nanocomposite synthesis process, there is still a lot of work to do to implement this technique.

Theoretically, our energy control model about gas phase nanoparticle (nanocluster) has not been quantitatively defined. There are still some gaps between the model and experimental results.

Practically, the synthesis method also has some problems to be solved, such as yield improvement, efficiency of the sputtering target usage, etc. And the experimental results are too sensitive to the condition of fabrication system, which is unfavorable for industrial application.

However, it is impossible for these problems to shadow the great future of this gas phase synthesis technique. We have the confidence that this technique will eventually developed into mature technique with a wide application to most of the fields of the magnetis.

BIBLIOGRAPHY

Chapter Two

1 Kiyotaka Wasa, Makoto Kitabatake and Hideaki Adachi

Thin film materials technology: sputtering of compound materials, Publisher William Andrew, New York (2004)

2 Bunshah, R. F., (ed.), *Deposition Technologies for Films and Coatings*, Noyes Publications, NJ, (1982); Mattox, D. M., *Handbook of Physical Vapor Deposition Processing*, Noyes Publications, NJ (1998); Mahan, J. E., *Physical Vapor Deposition of Thin Films*, John Wiley & Sons, New York (2000); Elshabini-Riad, A., and Barlow, F. D., III, (ed.), *Thin Film Technology Handbook*, McGraw-Hill, New York (1997)

3 Esaki, L., Proc. 6th Int. Vacuum Congr., Kyoto, *Jpn. J. Appl. Phys.*, 13:Suppl. 2(Pt. 1):821–828 (1974)

4 Stark W J and Pratsinis S E, *Powder Technol.* 126, 103–8 (2002)

5 a) J. E. McDonald, *American Journal of Physics*, 30, 870, 1962; b) J. E. McDonald, *American Journal of Physics*, 31, 31, 1963

6 M. Ohring, *The materials science of thin films: deposition and structure*, 2nd ed. (Academic Press, San Diego, CA, 2002).

7 K. H. Lieser, *Angew. Chem. Internat. Ed.* 8, 188, 1969

8 C. G. Granqvist and R. A. Buhrman, *J. Appl. Phys.* 47(5), 2200, 1976

- 9 K. Sattler, J. Muhlbach and E. Recknagel, *Phys. Rev. Lett.* 45, 821 (1980).
- 10 a) H. Haberland, M. Karrais, M. Mall, and Y. Thurner, *J. Vac. Sci. Tech.* A10, 3266, 1992; b) H. Haberland, M. Mall, M. Moseler, Y. Qiang, T. Reiners, and Y. Thurner, *J. Vac. Sci. Tech.* A12, 2925, 1994
- 11 C. Binns, K. N. Trohidou, J. Bansmann, S. H. Baker, J. A. Blackman, J-P Bucher, D. Kechrakos, A. Kleibert, S. Louch, K-H Meiwes-Broer, G. M. Pastor, A. Perez, and Y. Xie, *J. Phys. D: Appl. Phys.* 38, R357, 2005

Chapter Three

- 1 H. N. Bertram, Theory of magnetic recording (Cambridge University Press, Cambridge, New York, 1994).
- 2 S. X. Wang and A. M. Taratorin, Magnetic information storage technology (Academic Press, San Diego, 1999)
- 3 Ziese M and Thornton M J (ed) 2001 Spin Electronics (Berlin: Springer)
- 4 Coey J M D, Viret M and von Moln'ar S 1999 *Adv. Phys.* 48 167
- 5 Grunberg P, Schreiber R, Pang Y, Brodsky M B and Sowers H, *Phys. Rev. Lett.* 57, 2442 (1986)
- 6 Baibich M N, Broto J M, Fert A, Nguyen Van Dau F, Petroff F, Etienne P, Creuzet G, Friederich A and Chazelas J, *Phys. Rev. Lett.* 61, 2472 (1988)
- 7 Cowburn R P and Welland M E, *Science* 287, 1466 (2000)
- 8 Lagmago Kamta G and Starace A F, *Phys. Rev. Lett.* 88, 107901 (2002)

-
- 9 C. G. Granqvist and R. A. Buhrman, *J. Appl. Phys.* 47, 2200 (1976).
 - 10 K. Sattler, J. Muhlbach and E. Recknagel, *Phys. Rev. Lett.* 45, 821 (1980).
 - 11 H. Haberland, M. Karrais, M. Mall and Y. Thurner, *J. Vac. Sci. Technol., A* 10, 3266 (1992).
 - 12 C. G. Granqvist, R. A. Buhrman, J. Wyns and A. J. Sievers, *Phys. Rev. Lett.* 37, 625 (1976).
 - 13 S. Stappert, B. Rellinghaus, M. Acet and E. F. Wassermann, *J. Cryst. Growth* 252, 440 (2003).
 - 14 S. Stoyanov, V. Skumryev, Y. Zhang, Y. Huang, G. Hadjipanayis and J. Nogues, *J. Appl. Phys.* 93, 7592 (2003).
 - 15 Z. R. Dai, S. H. Sun and Z. L. Wang, *Nano Lett.* 1, 443 (2001).
 - 16 C. Antoniak et. al., *Phys. Rev. Lett.* 97, 117201 (2007)
 - 17 M. E. Gruner, et. al., *Phys. Rev. Lett.* 100, 087203 (2008)
 - 18 Michael Muller, Karsten Albe, *Acta Materialia* 55, 6617 (2007)
 - 19 R. M. Wang, et. al. *Phys. Rev. Lett.* 100, 017205 (2008)
 - 20 C. A. Ross, *Annu. Rev. Mater. Res.* 31, 203 (2001).
 - 21 Shouheng Sun, et al., *Science* 287, 1989 (2000).
 - 22 D. Weller, A. Moser, L. Folks, M. E. Best, W. Lee, M. F. Toney, M. Schwickert, J. Thiele, and M. F. Doerner, *IEEE Trans. Magn.*, 36, 10 (2000)
 - 23 D. L. Peng, T. Hihara, and K. Sumiyama, *Appl. Phys. Lett.*, 83, 350 (2003).
 - 24 Z. R. Dai, S. Sun, and Z. L. Wang, *Nano Lett.* 1, 443 (2001).

- 25 Jiaoming Qiu and Jian-Ping Wang, *Appl. Phys. Lett.* 88, 19205 (2006)
- 26 Xiaoqi Liu and Jian-Ping Wang, *J. Appl. Phys.* 105, 07A722 (2009)
- 27 Jiaoming Qiu, Jianmin Bai and Jian-Ping Wang, *Appl. Phys. Lett.* 89, 222506 (2006)
- 28 K Wegner, P Piseri, H Vahedi Tafreshi and P Milani, *J. Phys. D: Appl. Phys.*, 39, R439–R459 (2006).
- 29 O. A. Ivanov, L. V. Solina, V. A. Demshina, L. M. Magat, *Fiz. Metal. Metalloved.* 35, 92 (1973)
- 30 G. H. O. Daalderop, P. J. Kelly, and M. F. H. Schuurmans, *Phys. Rev. B.* 44, 12054 (1991)
- 31 M. J. Goeckner, J. A. Goree, and T. E. Sheridan, *IEEE Trans. Plasma Sci.* 19, 301 (1991)
- 32 J. A. Thornton, *Thin Solid Films*, 54, 23 (1978)
- 33 O.H. Chin, *Journal Fizik Malaysia*, V.24 p107 (2003)
- 34 V. I. Kirichenko, *Sov. Phys. - Techn. Phys.*, 21(9), 1080 (1976)
- 35 Okamoto S, et al, *Phys. Rev. B*, 66, 024413 (2002)
- 36 J B Staunton, et al, *J. Phys.: Condens. Matter*, 16, S5623–S5631 (2004)
- 37 Kiyotaka Wasa, Makoto Kitabatake and Hideaki Adachi, *Thin film materials technology: sputtering of compound materials*, Publisher William Andrew, New York (2004); Bunshah, R. F., (ed.), *Deposition Technologies for Films and Coatings*, Noyes Publications, NJ, (1982); Mattox, D. M., *Handbook of Physical Vapor*

Deposition Processing, Noyes Publications, NJ (1998); Mahan, J. E., Physical Vapor Deposition of Thin Films, John Wiley & Sons, New York (2000); Elshabini-Riad, A., and Barlow, F. D., III, (ed.), Thin Film Technology Handbook, McGraw-Hill, New York (1997).

Chapter Four

1 Data source: Webmagnetics (2007 Data).

2 J.M.D. Coey, "Invited paper Perspectives in permanent magnetism", J. Magn. Mater. 140-144, 1041-1044 (1995).

3 O Gutfleisch, "Review article Controlling the properties of high energy density permanent magnetic materials by different processing routes", J. Phys. D: Appl. Phys. 33, R157-R172 (2000).

4 David Brown, Bao-Min Ma, Zhongmin Chen, "Topic review: Developments in the processing and Properties of NdFeb-type permanent magnets", J. Magn. Mater. 248, 432-440 (2002).

5 K. Khlopkov, O. Gutfleisch, D. Eckert, D. Hinz, B. Wall, W. Rodewald, K. -H. Muller and L. Schultz, "Local texture in Nd-Fe-B sintered magnets with maximized energy density", Journal of Alloys and Compounds 365, 259-265 (2004).

6 A. S. Kim and F. E. Camp, "High performance NdFeB magnets (invited)", J. Appl. Phys. 79(8), 5035-5039 (1996).

- 7 Eckart F. Kneller, and Reinhard Hawig, "The exchange spring magnet: A new material principle for permanent magnets", IEEE Trans. on Magn. 27(4), 3588-3600 (1991).
- 8 Ralph Skomski and J. M. D. Coey, "Giant energy product in nanostructured two-phase magnets", Phys. Rev. B 48(21), 15812-15816 (1993).
- 9 I. A. Al-Omari and D. J. Sellmyer, "Magnetic properties of nanostructured CoSm/FeCo films", Phys. Rev. B. 52(5), 3441 (1995)
- 10 Eric E. Fullerton, J. Samuel Jiang, C. H. Sowers, J. E. Pearson and S. D. Bader, "Structure and magnetic properties of exchange spring Sm-Co/Co superlattices", Appl. Phys. Lett. 72(3), 380-382 (1998).
- 11 J. S. Jiang, J. E. Pearson, Z. Y. Liu, B. Kabius, S. Trasobares, D. J. Miller, S. D. Bader, D. R. Lee, D. Haskel, G. Srajer, and J. P. Liu, "Improving exchange spring nanocomposite permanent magnets", Appl. Phys. Lett., 85(22), 5293-5295 (2004).
- 12 J. Zhang, Y. K. Takahashi, R. Gopalan, and K. Hono, "Sm(Co, Cu)₅/Fe exchange spring multilayer films with high energy product", Appl. Phys. Lett. 86, 122509 (2005).
- 13 V. Neu, K. Hafner, A. K. Patra and L. Schultz, "Fully epitaxial, exchange coupled SmCo₅/Fe/SmCo₅ trilayers", J. Phys. D: Appl. Phys. 39, 5116-5120 (2006).
- 14 A. Yan, A. Bollero, O. Gutfleisch, and K. -H. Muller, "Microstructure and magnetization reversal in nanocomposite SmCo₅/Sm₂Co₁₇ magnets", J. Appl. Phys. 91(4), 2192 (2002)

- 15 Jian Zhang, Shao-ying Zhang, Hong-wei Zhang and Bao-gen Shen, "Structure, magnetic properties and coercivity mechanism of nanocomposite SmCo₅/α-Fe magnets prepared by mechanical milling", *J. Appl. Phys.* 89(10), 5601 (2001)
- 16 Q. Zeng, Y. Zhang, M. J. Bonder, G. C. Hadjipanayis, and R. Radhakrishnan, "Bulk SmCo₅/α-Fe composite by plasma pressure consolidation", *IEEE Trans. Magn.* 39(5), 2974 (2003)
- 17 Yanglong Hou, Shouheng Sun, Chuanbing Rong, and J. Ping Liu, "SmCo₅/Fe nanocomposites synthesized from reductive annealing of oxide nanoparticles", *Appl. Phys. Lett.* 91, 153117 (2007)
- 18 N.V. Rama Rao, R. Gopalan, M. Manivel Raja, V. Chandrasekaran, D. Chakravarty, R. Sundaresan, R. Ranganathan, K. Hono, "Structural and magnetic studies on spark plasma sintered SmCo₅/Fe bulk nanocomposite magnets", *J. Magn. Mater.* 312, 252-257 (2007).
- 19 R.F. Sabiryanov, S. S. Jaswal, "Electronic structure and magnetic properties of hard/soft multilayers", *J. Magn. Mater.* 177-181, 989-990(1998).
- 20 Joseph E. Davies, Olav Hellwig, Eric E. Fullerton, J. S. Jiang, S. D. Bader, G. T. Zimanyi and Kai Liu, "Anisotropy dependence of irreversible switching in Fe/SmCo and FeNi/FePt exchange spring magnet films", *Appl. Phys. Lett.* 86, 262503 (2005).
- 21 Francesca Casoli, Franca Albertini, Simone Fabbri, Claudio Bocchi, Lucia Nasi, Roberta Ciprian and Luigi Pareti, "Exchange coupled FePt/Fe bilayers with perpendicular magnetization", *IEEE Trans. Magn.* 41(10), 3877 (2005).

- 22 Jian Zhou, Ralph Skomski, Xingzhong Li, Wei Tang, George C. Hadjipanayis and David J. Sellmyer, “ Permanent-Magnet Properties of Thermally Processed FePt and FePt-Fe Multilayer Films”, IEEE Trans. Magn. 38(5), 2802 (2002).
- 23 Hao Zeng, Jing Li, J. P. Liu, Zhong L. Wang, and Shouheng Sun, “ Exchange-coupled nanocomposite magnets by nanoparticle self-assembly”, Nature 420, 395 (2002)
- 24 Junichi Kawanura, Kazuhisa Sato and Yoshihiko Hirotsu, “Fabrication of exchange-coupled α -Fe/L10-FePd nanocomposite isolated particles”, J. Appl. Phys. 96(7), 3906 (2004)
- 25 Katayun Barmak, Jihwan Kim, Roger A. Ristau, and Laura H. Lewis, “Ferromagnetic exchange spring nanocomposites of A1+L10 CoPt”, IEEE Trans. Magn. Magn. 38(5), 2799 (2002).
- 26 X. Rui, J. E. Shield, Z. Sun, Y. Xu, and D. J. Sellmyer, “In-cluster-structured exchange-coupled magnets with high energy densities”, Appl. Phys. Lett. 89, 122509 (2006).
- 27 P. Sharma, J. Waki, N. Kaushik, D. V. Louzguine-Luzgin, H. Kimura, A. Inoue, “High coercivity characteristics of FePtB exchange-coupled nanocomposite thick film spring magnets produced by sputtering”, Acta materialia 55, 4203-4212 (2007)
- 28 M. Shindo, M. Ishizone, H. Kato, T. Miyazaki, A. Sakuma, “Exchange spring behavior in sputter-denposited α -Fe/Nd-Fe-B multilayer magnets”, J. Magn. Magn. Mater. 161, L1-L5 (1996).

- 29 B. Z. Cui, M. J. O'Shea, "Hard magnetic properties of rapidly annealed NdFeB/Co films and intergrain interactions", *J. Magn. Magn. Mater.* 279, 27-35 (2004)
- 30 R. Coehoorn, D. B. de Mooij, J. P. W. B. Duchateau, and K. H. J. Buschow, *J. Phys. (Paris), Colloq.* 8, 669 (1988).
- 31 L. Withanawasam, G. C. Hadjipanayis, R. F. Krause, "Enhanced remanence in isotropic Fe-rich melt-spun Nd-Fe-B ribbons", *J. Appl. Phys.* 75(10), 6646 (1994).
- 32 I. panagiotopoulos, L. Withanawasam, G. C. Hadjipanayis, "Exchange spring behavior in nanocomposite hard magnetic materials", *J. Magn. Magn. Mater.* 152, 353-358 (1996).
- 33 D. Goll, M. Seeger, H. Kronmuller, "Magnetic and microstructural properties of nanocrystalline exchange coupled PrFeB permanent magnets", *J. Magn. Magn. Mater.* 185, 49-60 (1998).
- 34 P. G. McCormick, W. F. Miao, P. A. I. Smith, J. Ding, R. Street, "Mechanically alloyed nanocomposite magnets (invited)", *J. Appl. Phys.* 83(11), 6256 (1998)
- 35 K. Raviprasad, M. Funakoshi, and M. Umemoto, "Synthesis and characterization of Nd₂Fe₁₄B-25% Fe nanocomposite magnets", *J. Appl. Phys.* 83(2), 921 (1998).
- 36 H. Ono, N. Waki, M. Shimada, T. Sugiyama, A. Fujiki, H. Yamamoto, "Isotropic bulk exchange spring magnets with 134kJ/m³ prepared by spark plasma sintering method", *IEEE Trans. Magn.* 37(4), 2552 (2001)
- 37 Z. C. Wang, H. A. Davies, S. Z. Zhou, M. C. Zhang and Y. Qiao, "Preparation

- and magnetic properties of melt-spun Nd₂Fe₁₄(BC)/ α -Fe nanocomposite magnets”, J. Appl. Phys. 91(10), 7884 (2002).
- 38 A. M. Gabay, Y. Zhang, and G. C. Hadjipanayis, “Die-upset hybrid Pr-Fe-B nanocomposite magnets”, Appl. Phys. Lett. 85(3), 446 (2004).
- 39 Y. Otani, A. Moukarika, Hong Sun and J. M. D. Coey, “Metal bonded Sm₂Fe₁₇N₃- δ magnets”, J. Appl. Phys., 69(9), 6735 (1991).
- 40 J. J. Wyslocki, P. Pawlik, W. Kaszuwara, M. Leonowicz, “Magnetic properties and intrinsic magnetic parameters of nanocrystalline Sm-Fe-N magnets”, J. Magn. Mater. 272-276, e1929-e1930 (2004).
- 41 T. Leineweber, H. Kronmuller, “Micromagnetic examination of exchange coupled ferromagnetic nanolayers”, J. Magn. Mater. 176, 145-154 (1997).
- 42 Matteo Amato, Angelo Rettori, Maria Gloria Pini, “Exchange-spring behavior of hard/soft magnetic multilayers: optimization study of the nanostructure”, Phys. B 275, 120-123 (2000).
- 43 Dieter Weller, Andreas Moser, Liesl Folks, Margaret E. Best, Wen Lee, Mike F. Toney, M. Schwickert, Jan-Ulrich Thiele, and Mary F. Doerner, “ High Ku materials Approach to 100 Gbits/in²”, IEEE Trans. Magn. 36(1), 10 (2000).
- 44 Robert C. O'Handley, “Modern Magnetic Materials: Principles and Applications”, publisher Wiley-Interscience (1999)
- 45 The material settings are: For m soft phase, $M_s=1.6 \times 10^6$ A/m, $A = 6 \times 10^{-12}$ J/m, $K=1 \times 10^5$ J/m³; For k hard phase, $M_s=1.6 \times 10^6$ A/m, $A = 6 \times 10^{-12}$ J/m, $K=7 \times 10^6$ J/m³.

Dimensions for m and k phase are both 2 nm. For strong m and k coupling, $A = 6 \times 10^{-12} \text{J/m.}$, for weak m and k coupling, $A = 1.2 \times 10^{-12} \text{J/m.}$ Calculation settings are: the damping coefficient used is $\alpha=0.5$, the cell size are 0.5nm.

46 M. Donahue and D. Porter, the Object Oriented MicroMagnetic Framework (OOMMF) project at ITL/NIST, <http://math.nist.gov/oommf/>.

Chapter Five

- 1 J.M.D. Coey, J. Magn. Magn. Mater. 140-144, 1041-1044 (1995)
- 2 O Gutfleisch, J. Phys. D: Appl. Phys. 33, R157-R172 (2000)
- 3 David Brown, Bao-Min Ma, Zhongmin Chen, J. Magn. Magn. Mater. 248, 432-440 (2002)
- 4 Eckart F. Kneller and Reinhard Hawig, IEEE Trans. Magn. 27(4), 3588 (1991)
- 5 Ralph Skomski and J. M. D. Coey, Phys. Rev. B 48(21), 15812 (1993)
- 6 T. Schrefl, H. Kronmuller, and J. Fidler, J. Magn. Magn. Mater. 127, L273 (1993)
- 7 K. Khlopkov, O. Gutfleisch, D. Eckert, D. Hinz, B. Wall, W. Rodewald, K. -H. Muller and L. Schultz, "Local texture in Nd-Fe-B sintered magnets with maximized energy density", Journal of Alloys and Compounds 365, 259-265 (2004)
- 8 I. A. Al-Omari and D. J. Sellmyer, Phys. Rev. B. 52(5), 3441 (1995)
- 9 Eric E. Fullerton, J. Samuel Jiang, C. H. Sowers, J. E. Pearson and S. D. Bader,

Appl. Phys. Lett. 72(3), 380-382 (1998)

10 J. S. Jiang, J. E. Pearson, Z. Y. Liu, B. Kabius, S. Trasobares, D. J. Miller, S. D.

Bader, D. R. Lee, D. Haskel, G. Srajer, and J. P. Liu, Appl. Phys. Lett., 85(22),
5293-5295 (2004)

11 J. Zhang, Y. K. Takahashi, R. Gopalan, and K. Hono, Appl. Phys. Lett. 86,
122509 (2005)

12 V. Neu, K. Hafner, A. K. Patra and L. Schultz, J. Phys. D: Appl. Phys. 39,
5116-5120 (2006)

13 R.F. Sabiryanov, S. S. Jaswal, J. Magn. Mater. 177-181, 989-990(1998).

14 Joseph E. Davies, Olav Hellwig, Eric E. Fullerton, J. S. Jiang, S. D. Bader, G. T.
Zimanyi and Kai Liu, Appl. Phys. Lett. 86, 262503 (2005).

15 Francesca Casoli, Franca Albertini, Simone Fabbri, Claudio Bocchi, Lucia Nasi,
Roberta Ciprian and Luigi Pareti, IEEE Trans. Magn. 41(10), 3877 (2005).

16 Jian Zhou, Ralph Skomski, Xingzhong Li, Wei Tang, George C. Hadjipanayis
and David J. Sellmyer, IEEE Trans. Magn. 38(5), 2802 (2002)

17 M. Shindo, M. Ishizone, H. Kato, T. Miyazaki, A. Sakuma, J. Magn. Mater.
161, L1-L5 (1996)

18 B. Z. Cui, M. J. O'Shea, J. Magn. Mater. 279, 27-35 (2004)

19 Matteo Amato, Angelo Rettori, Maria Gloria Pini, Phys. B 275, 120-123 (2000)

20 Hao Zeng, Jing Li, J. P. Liu, Zhong L. Wang, and Shouheng Sun, Nature 420,
395 (2002)

-
- 21 Yanglong Hou, Shouheng Sun, Chuanbing Rong, and J. Ping Liu, *Appl. Phys. Lett.* 91, 153117 (2007)
- 22 J. M. Qiu and J. P. Wang, *Appl. Phys. Lett.* 88, 192505 (2006)
- 23 Xiaoqi Liu and J. P. Wang, *J. Appl. Phys.* 105, 07A722 (2009)
- 24 J. M. Qiu and J. P. Wang, *Appl. Phys. Lett.* 89, 222506 (2006)
- 25 C.Rong, Yuzi Liu and J. P. Liu, *Appl. Phys. Lett.* 93, 042508 (2008)
- 26 C. Rong and J. P. Liu, *Appl. Phys. Lett.* 94, 172510 (2009)
- 27 P. E. Kelly, K. O'Grady, P. I. Mayo, and R. W. Chantrell, *IEEE Trans. Magn.* 25, 3881 (1989)
- 28 E P Wohlfarth, *J. Appl. Phys.*, 29, 598, (1958)
- 29 Okamoto S, et al, *Phys. Rev. B*, 66, 024413 (2002)
- 30 J B Staunton, et al, *J. Phys.: Condens. Matter*, 16, S5623–S5631 (2004)

APPENDIX

Appendix A: Localized Fe 3d electron states in Fe_{16}N_2

**Discovery of localized states of Fe 3d electrons in Fe_{16}N_2 and Fe_8N films: an
evidence of the existence of giant saturation magnetization**

Xiaoqi Liu¹, Yun-Hao Xu¹, Cecilia Sanchez-Hanke² and Jian-Ping Wang^{1*}

1. The Center for Micromagnetics and Information Technologies (MINT) and
Department of Electrical and Computer Engineering, University of Minnesota,

Minneapolis, MN, 55455

2. National Synchrotron Light Source, Brookhaven National Laboratory, Upton, NY

11973-5000

*Corresponding author: Email: jpwang@umn.edu; Tel: 612-625-9509

Abstract

The mystery of giant saturation magnetization of Fe_{16}N_2 has remained for 37 years. In this letter, X-ray absorption spectroscopy (XAS) and magnetic circular dichroism (XMCD) are used to study the electron states of Fe atoms in Fe_{16}N_2 and Fe_8N films. Localized Fe 3d electron states, which are not expected from current theories (models), are observed. The XMCD spectra and elemental hysteresis loops reveal the polarization of N atoms and the hybridization of N and Fe atoms. This discovery points to the origin of giant saturation magnetization in Fe_{16}N_2 .

Confirmation and understanding the origin of giant saturation magnetization is essential to revolutionize the exchange-spring type permanent magnets for any energy efficient applications and breakthrough the bottleneck for the writability of current magnetic heads for extremely high areal density recording up to several Terabit/in² without switching to heat assisted magnetic recording and bit patterned media. Currently the highest saturation magnetization value ($4\pi M_s$) in available magnetic materials is about 2.45 T (FeCo alloy), which was predicted by the band magnetism theory. The α'' -Fe₁₆N₂ thin film was noted for its giant saturation magnetization (2.9 T) thirty-seven years ago [1, 2], followed by many experimental studies [3-11] with controversial results. Sugita et al [5, 6] reported an average value of $3.2 \mu_B/\text{Fe}$ in MBE-grown α'' -Fe₁₆N₂ single crystal thin films. Okamoto et al [7] and Sun [11] et al reported $2.8 \mu_B/\text{Fe}$ in high-quality FeN films with partial α'' -Fe₁₆N₂ phase by substrate-bombardment-free non-traditional deposition processes. Takahashi et al [8] and several other groups [9,10] reported less than $2.4 \mu_B/\text{Fe}$ in FeN films by traditional magnetron sputtering process.

Theoretical calculations have been done on the electron band structures of Fe and N in α'' -Fe₁₆N₂ structure [12-18]. Common to all the calculations is the use of three types of Fe sites in the α'' -Fe₁₆N₂ structure as shown in Fig.1. One of the general assumptions for all calculations is that Fe 3d electrons in Fe₁₆N₂ structure are itinerant (delocalized) as in other magnetic metals or alloys. However, the calculated average magnetic moment per Fe atom has never been higher than $2.5 \mu_B/\text{Fe}$. In this letter, we will first report the successful fabrication of FeN films with partial α'' -Fe₁₆N₂ phase, for which giant saturation magnetization (2.9 T) is

confirmed. Then we will report the discovery of the localized states of Fe 3d electrons in FeN films with Fe_{16}N_2 and Fe_8N structures, which hasn't been expected and applied for all previous theoretical calculations on Fe_{16}N_2 structure, by using X-ray absorption spectroscopy (XAS) and x-ray magnetic circular dichroism (XMCD) technique [19, 20].

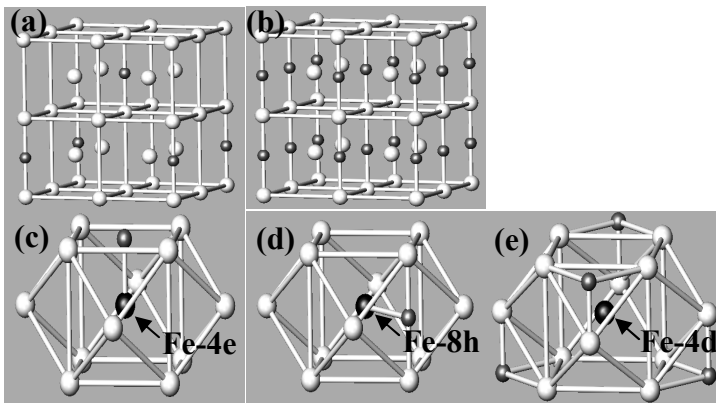


Fig. 1 Crystalline structure of (a) Fe_{16}N_2 and (b) Fe_8N (white-Fe; grey-N), (For Fe_8N , N atoms randomly distribute at all the possible N sites and keep N-Fe atom ratio at 1:8); Crystalline environment of (c) Fe-4e; (d) Fe-8h; (e) Fe-4d.

The FeN thin films with single Fe_8N phase and $\text{Fe}_{16}\text{N}_2 + \text{Fe}_8\text{N}$ mixed phases were grown by sputtering Fe targets in a mixture gas of Ar and N_2 using a facing-target-sputtering system. The base pressure of the sputtering chamber was 2×10^{-7} Torr. Si (100) substrates capping with about 100 nm SiO_2 were used. By adjusting the substrate temperature and the ratio of Ar and N_2 in the gas flow, a series of FeN films with different phases were successfully fabricated. The crystal structure of FeN thin films was characterized by a Co source x-ray diffractometer (XRD). Their magnetic properties were measured by a vibrating sample magnetometer (VSM).

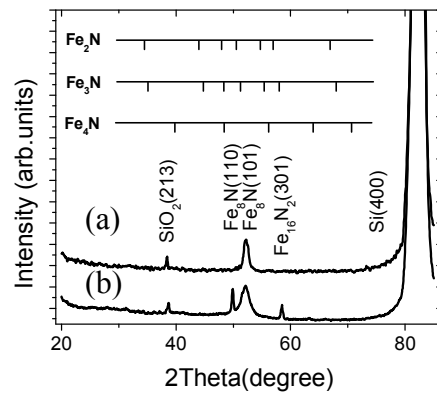


Fig. 2 XRD spectra of (a) sample A with single Fe_8N phase and (b) sample B with $\text{Fe}_8\text{N}+\text{Fe}_{16}\text{N}_2$ phases.

Fig. 2 shows the XRD spectra of two 50 nm thick FeN films. For sample A, besides $\text{SiO}_2(213)$ and $\text{Si}(400)$ peaks from the substrate, only one peak at 52.4° appears, corresponding to $\text{Fe}_8\text{N}(110)$ peak. To confirm the single Fe_8N phase in sample A, $\text{Fe}_8\text{N}(101)$ and (002) peaks were observed in grazing incident angle XRD measurements. Together, these peaks exclude other FeN phases such as Fe [30], Fe_2N [31], Fe_3N [32], or Fe_4N [32]. For sample B, three peaks are observed at 49.9° , 52.4° and 58.6° , corresponding to $\text{Fe}_8\text{N}(101)$, $\text{Fe}_8\text{N}(110)$ and $\text{Fe}_{16}\text{N}_2(301)$ respectively. The $\text{Fe}_{16}\text{N}_2(301)$ peak is one of characteristic peaks for Fe_{16}N_2 phase. Another characteristic peak, $\text{Fe}_{16}\text{N}_2(002)$, was detected by grazing incident angle XRD measurement. Therefore sample B contains two FeN phases, Fe_8N and Fe_{16}N_2 . The saturation magnetization ($4\pi M_s$) of sample A and B measured by the VSM are 2.14 T and 2.39 T respectively. The M_s value of Fe_8N (sample A) agrees very well with that reported by Okamoto et al [33]. The volume fraction of Fe_{16}N_2 phase in sample B is estimated to be about 30% by considering peak intensities of

$\text{Fe}_{16}\text{N}_2(301)$ and $\text{Fe}_8\text{N}(110)$ in the XRD pattern and the structure factors of these two peaks in the bct crystalline structure [34]. The saturation magnetization ($4\pi M_s$) of Fe_{16}N_2 phase was therefore calculated to be 2.96 T, which agrees well with that reported by Sugita et al [6].

The XAS and XMCD were performed on beamline X13A of the National Synchrotron Light Source (NSLS) at Brookhaven National Laboratory (BNL). The XAS and XMCD spectra were recorded in total electron yield mode (TEY) using elliptically polarized soft x-rays with $\sim 70\%$ degree of circular polarization. A magnetic field up to 0.2 T was applied parallel to the sample surface and along the incident x-ray direction. The photon incident angle was set at 8 degree. The line structures of XAS and XMCD directly represent the Fe 3d state electronic configurations [21, 22]. The spin and orbital moment of Fe atoms are studied based on XMCD sum rules [23, 24, 25]. The XAS and XMCD spectra with different multiplet structures are used to identify different localized Fe 3d states, as demonstrated in theory and experiment [26 - 29].

The remarkable observation in the XAS and XMCD spectra of Fe_8N and $\text{Fe}_{16}\text{N}_2 + \text{Fe}_8\text{N}$ films is the appearance of multiplet structures in the energy range of the Fe $L_{3,2}$ edge, as shown in Fig 3. The multiplet positions in the spectra were labeled with black dashed lines in fig 3 (A) and (B). Published XMCD spectra from bulk iron [25] and localized Fe $3d^7$ state [29] were also included in Fig.3 for comparison. In XAS and XMCD spectra, Fe $L_{3,2}$ edges with sharp multiplet structures are normally fingerprints of localized Fe atomic configurations [28, 29]. The reference XMCD spectra of delocalized Fe 3d states in bulk iron (Fig. 3(C)) and localized Fe $3d^7$ state (Fig. 3(D)) indicate that only XMCD spectra of localized Fe 3d states contain

multiplet Fe $L_{3,2}$ edges. In the XMCD spectra of delocalized Fe 3d states, multiplet Fe $L_{3,2}$ edges are clearly absent, only broad single negative L_3 and positive L_2 edges were obtained because of the presence of band like 3d states structure rather than discrete states. Therefore, these multiplet Fe $L_{3,2}$ edges in the XAS and XMCD spectra provide the first direct evidence of the existence of localized Fe 3d states in Fe_8N and $Fe_{16}N_2$ structures.

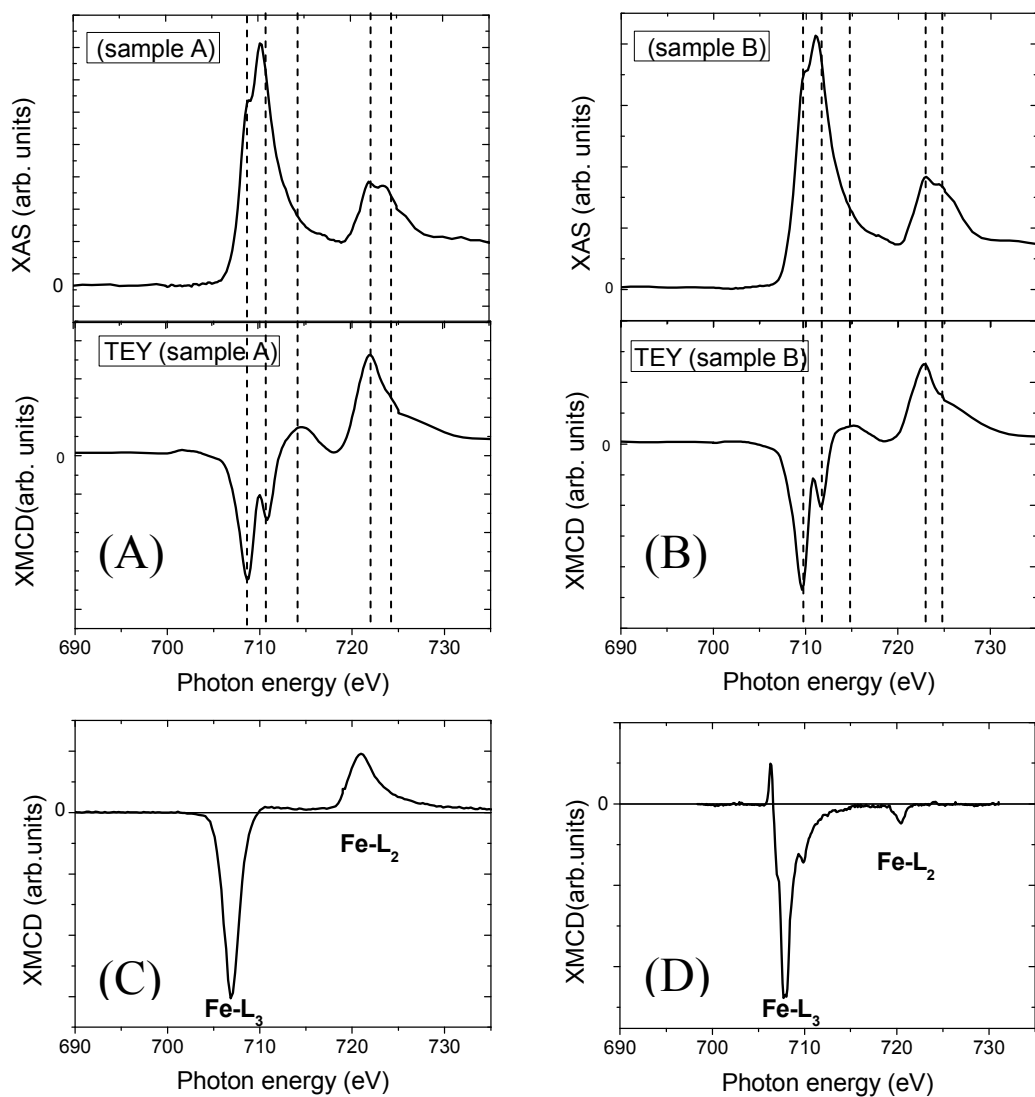


Fig. 3 XAS and XMCD spectra of (A) sample A, (B) sample B, (C) delocalized Fe 3d state in bulk iron [25] and (D) localized Fe 3d⁷ state [29].

Although localized Fe 3d states were observed in Fe₈N and Fe₁₆N₂ films, the fact that Fe₈N and Fe₁₆N₂ films possess low electrical resistivity, which is comparable to iron film [35], reveals that plenty of itinerant electrons still exist in the Fe₈N and Fe₁₆N₂ structures. This implies that these localized Fe 3d states are not completely but partially localized.

Furthermore, Fe 3d states in Fe₈N and Fe₁₆N₂ structures are confirmed to be partially localized based on a quantitative indicator, ratio R, defined as the ratio between Fe L₂ peak area and L₃ peak area in the XMCD spectra. Based on the equations of sum rules, the orbital moment contribution to the total magnetic moment of Fe atoms can be deduced from the R value [36]. An $R \sim -1$ indicates completely quenched orbital moment ($M_{\text{orbital}} \sim 0$), which is a basic characteristic of delocalized Fe state. For localized Fe 3d states, the orbital moment can be completely or partially unquenched. So the R value will be deviated from -1 . As summarized in table 1, R values for different Fe 3d states were extracted from XMCD spectra based on the method presented by Brewer et al [36]. The R values for sample A and sample B were -0.76 and -0.72 respectively, which indicate partially unquenched Fe 3d orbital moments, since the R values for localized Fe 3d⁵, 3d⁶ and delocalized Fe 3d states are -1 , -0.36 and -0.90 respectively. This result strongly supports the argument that Fe states in sample A and B are partially localized Fe 3d states. Therefore, the R values for sample A and B are strong evidence of the existence of localized Fe 3d states in Fe₈N and Fe₁₆N₂ structures. The differences between the XMCD spectra and R values of sample A and B also suggest that Fe 3d states in Fe₁₆N₂ are different from that in Fe₈N.

Table 1 Ratio R, orbital (M_o), spin (M_s) and total magnetic moment (M) of different Fe 3d states, extracted from XMCD spectra in Fig. 3. (M value of $Fe_{16}N_2$ phase was calculated from its saturation magnetization value. R value of Fe3d5 and 3d6 were calculated from the spectra in ref. [28]. The magnetic moment of Fe 3d⁵ and 3d⁶ were calculated by Hund's rules.)

	Fe ₈ N (sample A)	Fe ₁₆ N ₂ +Fe ₈ N (sample B)	Fe ₁₆ N ₂	Fe 3d ⁵ [28]	Fe 3d ⁶ [28]	Fe 3d ⁷ [29]	Fe in bulk iron[25]
Ratio R	-0.76	-0.72		-1	-0.36	0.09	-0.90
$M_o(\mu_B)$				0	2.45	3.46	0.09
$M_s(\mu_B)$				5.92	4.90	3.87	1.98
$M(\mu_B)$	2.20	2.46	3.20	5.92	6.71	6.67	2.07

Fe atoms in bulk iron are averaging 6.61 3d electrons. Therefore in Fe₈N/Fe₁₆N₂ structure, the average 3d electron number of Fe atoms will be in the range of 5-7 electrons. Table 1 shows the magnetic moments for localized Fe 3d⁵, 3d⁶ and 3d⁷ states which are calculated based on Hund's rules. All three localized Fe states possess much enhanced total magnetic moment compared to delocalized Fe states (in bulk iron). The localization of Fe 3d states largely enhances both the orbital moment (except 3d⁵ state) and spin moment of Fe^{atoms}. The same moment enhancement effect was also reported by Gambardella et al on isolated Fe atoms with 3d⁷ configuration [29]. The finding of localized Fe 3d states with enhanced magnetic moments in Fe₁₆N₂ structures points to the origin of giant saturation magnetization of Fe₁₆N₂, considering that the unit cell volume of bct-Fe₁₆N₂ is just 10% larger than bcc-Fe structure.

One immediate question is what may cause the loss of giant saturation magnetization in Fe₈N structure in which localized Fe 3d states were also observed.

One possible reason could be the lack of ordering of N atoms in Fe_8N structure. The random distributed N atoms in Fe_8N will result in a decrease in the number of Fe atoms in localized states and an increase in the number of Fe atoms in delocalized states, which both can lead to the decrease of total magnetization of Fe_8N .

In bct Fe_{16}N_2 and Fe_8N structures (figure 1 (a) and (b)), the localization of Fe 3d states from the delocalized Fe 3d state in bcc bulk iron arise from the perturbation of the crystal field of N atoms. Since Fe(4e) and Fe(8h) site are 60% and 50% closer to the N sites in distance than Fe(4d) site (Fig.1 (c-e)), Fe atoms at Fe(4e) and Fe(8h) sites should have stronger bonding with neighbor N atoms than that at Fe(4d) site, which indicate that Fe atoms at Fe(4e) and Fe(8h) sites have higher degree of localization than at Fe(4d) site.

The bonding (hybridization) between Fe atoms and N atoms is proved by a further XMCD analysis that was performed in the energy range of 340-460 eV for sample A and B. The Nitrogen K edge is found at 397.0 eV, which is consistent with the XPS result ($\sim 398\text{eV}$) [37]. The N K edge moves to lower energy compared to the binding energy of 1s electrons of single N atom (409.9 eV) [38]. The hybridization of N atoms with partially localized Fe atoms is expected to cause the N atoms negatively charged. Therefore the Coulomb interaction between electrons results in the increase of energy level of N 1s states and N K edge shifting to lower energy.

Hysteresis loops of N and Fe atoms recorded at the N K edge and Fe L_3 edge with an in-plane magnetic field provide direct evidence of the spin polarization of N atoms and the hybridization of N and Fe atoms as shown in Fig. 4. The hysteresis loops of N and Fe atoms exhibit the same coercive field of 15 Oe for both sample A and B. The spin polarization of N atoms and the hybridization between N and Fe atom could be the main cause of the localization of the 3d states of Fe atoms in the

Fe_8N and Fe_{16}N_2 structures.

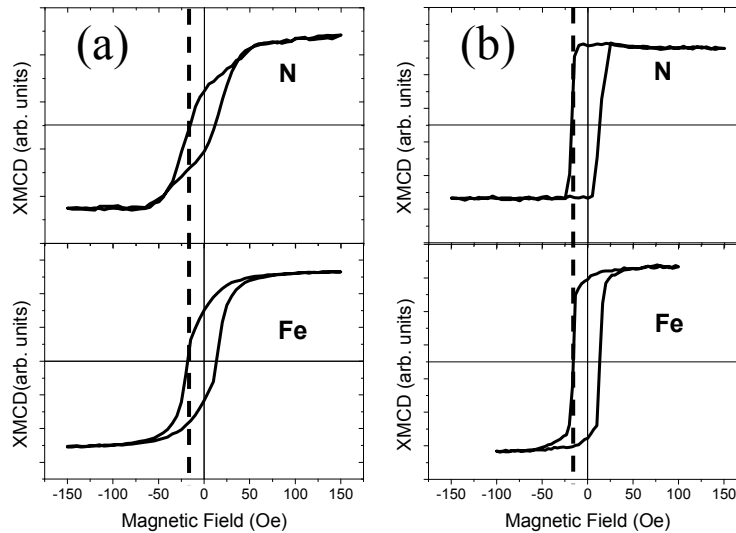


Fig. 4 Hysteresis loops recorded for N atoms at K-edge 399 eV and Fe atoms at L_3 edge 707eV on (a) sample A and (b) sample B.

In conclusion, we report the discovery of partial localized Fe 3d states in Fe_{16}N_2 and Fe_8N films. The partial localization of Fe 3d states introduced large unquenched orbital moment and enhanced spin moment in Fe atoms, therefore greatly increased the average magnetic moment of Fe atoms. This discovery may not only explain the origins of giant saturation magnetization in Fe_{16}N_2 structure but also points out a direction to search for new magnetic materials with giant saturation magnetization.

The work was partially supported by the U.S. Department of Energy, Office of Basic Energy Sciences under contract No. DE-AC02-98CH10886, National Science Foundation NNIN program at University of Minnesota, Seagate Technology and Western Digital Cooperation. The authors would like to thank Prof. Frank De Groot of Utrecht University for his help on the XMCD multiplet calculations, the useful conversations with Mr. Nian Ji, Prof. Jack Judy, Dr. Mark Kief and Dr. Yinjian

References:

- [1] T.K. Kim et al., *Appl. Phys. Lett.* 20, 492(1972)
- [2] K.H. Jack, *Proc. R. Soc. London Ser. A* 208, 216(1951)
- [3] K. Nakajima et al., *Appl. Phys. Lett.* 56, 92(1990)
- [4] C. Gao et al., *J. Appl. Phys.* 73, 6579(1993)
- [5] M. Komuro et al, *J. Appl. Phys.*, 67, 5126(1990)
- [6] Y. Sugita et al, *J. Appl. Phys.*, 70, 5977(1991)
- [7] S. Okamoto et al., *J. Appl. Phys.* 79, 1678(1996)
- [8] M. Takahashi et al., *J. Appl. Phys.* 76, 6642(1994)
- [9] J. M. D. Coey, *J. Appl. Phys.* 76, 6632 (1994)
- [10] C. Ortiz et al., *Appl. Phys. Lett.* 65, 2737(1994)
- [11] D.C. Sun et al., *J. Appl. Phys.* 79, 5440(1996)
- [12] A. Sakuma, *J. Magn. Magn. Mater.* 102, 127(1991)
- [13] S. Ishida et al., *J. Phys.: Condens. Matter* 4, 765(1992)
- [14] B.I. Min, *Phys. Rev. B*, 46, 8232(1992)
- [15] R. Coehoorn et al, *Phys. Rev. B*, 48, 3830(1993)
- [16] K. Miura et al., *J. Phys.: Condens. Matter* 5, 9393(1993)
- [17] H. Sawada et al., *Phys. Rev. B*, 50, 10004(1994)
- [18] H. Tanaka et al., *Phys. Rev. B*, 62, 15042(2000)
- [19] G. Schütz et al., *Phys. Rev. Lett.* 58, 737(1987)
- [20] J. Stöhr and H. König, *Phys. Rev. Lett.* 75, 3748(1995)
- [21] F. M. F. de Groot, J.C. Fuggle, B.T. Thole and G.A. Sawatzky, *Physical Review B*, 42, 5459 (1990)

-
- [22] B. T. Thole and G. van der Laan, Phys. Rev. Lett., 67, 3306 (1991)
- [23] B.T. Thole et al, Phys. Rev. Lett. 68, 1943(1992)
- [24] P. Carra et al., Phys. Rev. Lett. 70, 694(1993)
- [25] C.T. Chen et al., Phys. Rev. Lett., 75, 152(1995)
- [26] Y.X.Lu et al., Phys. Rev. B, 70, 233304(2004)
- [27] P. Morrall et. al., Phys. Rev. B 67, 214408(2003)
- [28] G. van der Laan, B. T. Thole, Phys. Rev. B, 43, 13401(1991)
- [29] P. Gambardella et al., Phys. Rev. Lett. 88, 047202(2002)
- [30] Swanson et al., natl. Bur. Stand. (U.S.), Circ. 539, IV, 3(1955)
- [31] A. Burdese, Metal. Ital., 49, 195(1957)
- [32] H. Jacobs et al., J. Alloys Compds. 227, 10(1995)
- [33] S. Okamoto et al., J. Appl. Phys. 79, 5250(1996)
- [34] H. Tanaka et al., Acta Mater., 45, 1401(1997)
- [35] H. Takahashi et al, J. Appl. Phys. 84, 1493(1998)
- [36] W.D. Brewer et al., Phys. Rev. Lett., 93, 077205(2004)
- [37] H. Takahashi et al., IEEE Trans. Magn. 36, 2921(2000)
- [38] M. Cardona and L. Ley, Eds., Photoemission in Solids I: General Principles (Springer-Verlag, Berlin1978)

Appendix B: Surface effects on the magnetization switching behavior of L1₀ FePt nanoparticle

Surface anisotropy in octahedral L1₀ phase FePt nanoparticles

Xiaoqi Liu, Jiao-Ming Qiu and Jian-Ping Wang*

The Center for Micromagnetics and Information Technologies (MINT) and the
Department of Electrical and Computer Engineering, University of Minnesota
200 Union ST SE, Minneapolis, Minnesota, 55455

*Correspondence to Jian-Ping Wang, Professor, Professor of Electrical and
Computer Engineering Department, Graduate Faculty of Physics Department and
Chemical Engineering and Materials Science Department, University of Minnesota,
4-174 200 Union Street SE, Minneapolis, Minnesota 55455

Email: jpwang@umn.edu, fax: 612-625-4583

Abstract

We report the experimental observation and micromagnetic simulation of surface anisotropy effect on the magnetization reversal process of uniform single-crystalline 5.8nm $L1_0$ phase FePt nanoparticles with octahedral shape. The surface anisotropy was found to be perpendicular to $\{111\}$ plane with a magnitude of 4×10^{-2} erg/cm² (4×10^{-5} J/m²). This surface anisotropy defines the direction of surface moments, which switch independently from the bulk. The surface moments have a switching field of 2000 Oe with little temperature dependence.

Surface atoms play an important role in determining the physical performance of nanostructured materials as they have increased overall fraction and lowered coordination number. The study of surface effect on magnetic phenomena is especially interesting and important with the continued shrinkage of feature sizes in magnetic recording devices [1] and for the emergence of spintronics [2]. Surface magnetism has inspired tremendous interest since the early work of Louis Néel [3] and remains as an important research topic [4]. However, very limited results were reported on the direct measurement of surface anisotropy of magnetic nanoparticles because of accessibility issues [5]. As a consequence, most of the treatments were done theoretically except for certain thin film cases, in which large and repeatable surfaces can be constructed experimentally [6]. In the case of nanoparticles it is even not easy to determine the magnetic easy direction on the surface [7]. Simulation results have shown that the surface contribution to the effective anisotropy of magnetic nanoparticles depends on both the orientation and magnitude of surface anisotropy, while the latter is usually just an estimation based on the strength of exchange interaction [8]. Attempt to mathematically deduce the magnitude of surface anisotropy from the total effective anisotropy which includes bulk contribution through pressure experiments is also reported [9].

Magnetic nanoparticles prepared using wet-chemical approaches [10] are often coated with small chemical stabilizers, which render the real surface

phenomenon study difficult. On the other hand, surface-contamination free magnetic nanoparticles can be made using physical vapor deposition methods [11-12] and a more reliable surface anisotropy study thus becomes possible. Here we report the experimental observation of surface anisotropy in octahedral FePt nanoparticles in $L1_0$ phase. FePt binary alloys with composition in the vicinity of equal atomic ratio have two crystal phases at room temperature, namely the chemically disordered A1 phase and the chemically ordered $L1_0$ phase. The latter has huge magnetocrystalline anisotropy (MCA, 7×10^7 erg/cc) with an easy axis along the [001] direction [13]. $L1_0$ FePt nanoparticles have great potential in current information storage media [14] and permanent magnets [15] because their huge bulk anisotropy could keep the magnetization thermally stable at a size of several nanometers. The huge magnetocrystalline anisotropy also makes $L1_0$ FePt nanoparticle an ideal object for the observation of surface anisotropy, since the magnitude of surface anisotropy normally has much smaller magnitude [8, 9] which makes the separate observation of magnetocrystalline and surface anisotropy experimentally possible.

The octahedral $L1_0$ FePt nanoparticles were prepared using a novel gas-phase condensation technique [16], which can selectively make single-crystalline FePt nanoparticles with either A1 or $L1_0$ phases [17]. Statistical analysis of more than 2800 particles from 50 different TEM micrographs shows that these $L1_0$ FePt nanoparticles have a Gaussian distribution with effective mean size of 5.8 nm and standard deviation of 11%. As single-crystalline particles they are

dominated by octahedron shape as shown in Fig. 1. The uniformity in both particle size and shape makes the interpretation of their physical performance reliable. The octahedral shape is clearly visible from the high resolution transmission electron microscopy (HRTEM) image of one particle. Along its [001] axis, which is parallel to the substrate plane, alternating atomic layers are distinguishable till the end corners of the octahedron. The corresponding 3-D particle structure illustrates the packing sequence of Fe and Pt atoms and all the surface atoms sit on (111) planes, which are most closely packed with lowest surface energy. This structure was built based on the HRTEM image (Fig. 1b) and it has a length along the [001] axis of 6.7 nm. At this size surface atoms on the eight equivalent (111) planes (Fig. 1d) have an overall fraction of 28.3 %.

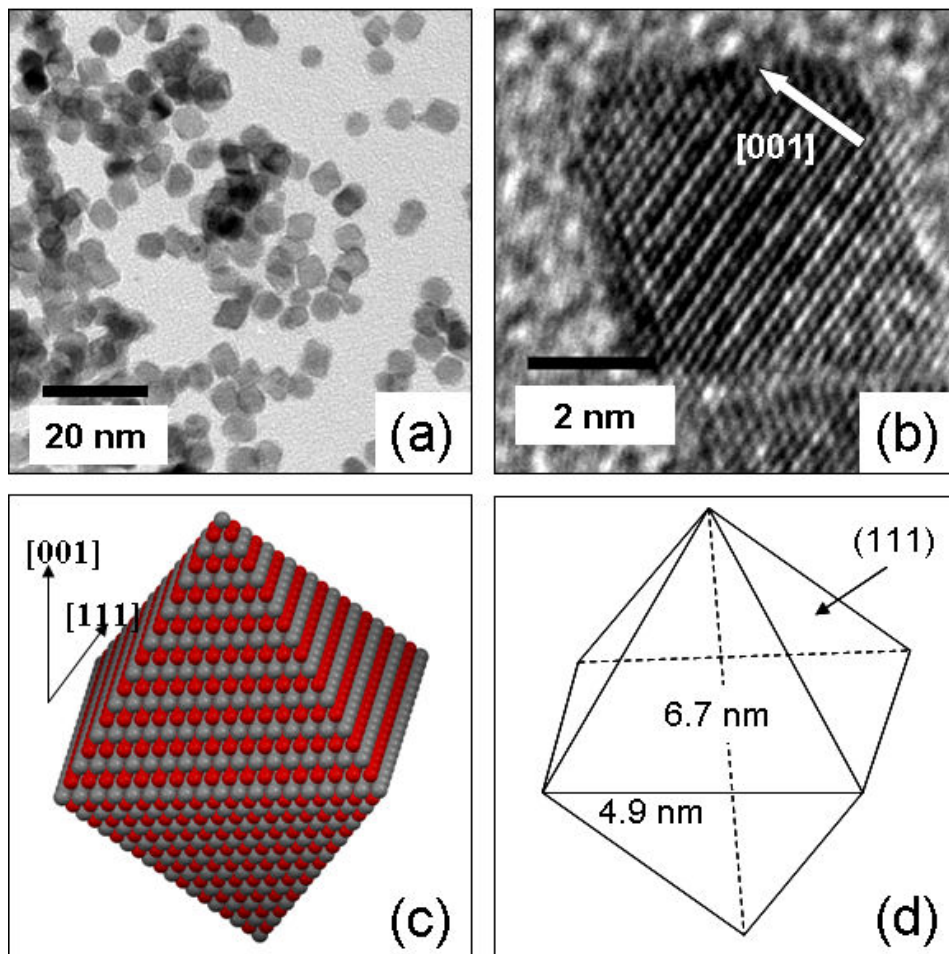


Figure 1. (Color online) Directly ordered $L1_0$ FePt nanoparticles prepared using a gas-phase aggregation technique at room temperature. (Ref [15]) (a) TEM micrograph of particles showing the uniform size distribution (b) HRTEM image of one chemically ordered particle with its c -axis (the magnetic easy axis) lying in-plane (c) A 3-D atomic reconstruction of the $L1_0$ FePt particle shown in (b). It has a length of 6.7 nm along the $[001]$ axis. (d) Schematic drawing of the eight equivalent $\{111\}$ planes in (c).

First we measured the magnetization reversal process of non-embedded nanoparticles using 30 layers of mono-dispersed 5.8 nm FePt nanoparticles with over 75% particles with their easy axes aligned parallel to the in-plane direction. The samples were prepared through in-flight guided landing by applying *in situ* magnetic field, which was applied directly over the silicon substrate [18]. The measurement fields were applied parallel to the easy axis direction. As shown in Fig. 2(a), the sample has a coercivity value of 33.4 kOe at measurement temperature of 5 Kelvin. Clearly there is a kink in the hysteresis loop around zero field. Second, the magnetization reversal process of 5.8nm FePt nanoparticles embedded in a non-magnetic matrix (carbon matrix) was measured, and identical magnetization reversal behaviors were observed compare to non-embedded 5.8nm FePt nanoparticles, which exclude the “kink” from the effect of dipole-dipole interaction. Similar behaviors have been found for highly ordered FePt particulate films [19] and octahedral-shaped FePt nanoparticles formed using FePt and MgO alternate deposition [20] at substrate temperature as high as 780°C. They were simply attributed to the existence of poorly ordered phase due to size effect, surface effects were not mentioned. Overlapping with the normal hysteresis loop a DC demagnetized (DCD) remanence curve (5 K) was plotted. The DCD curve was measured by first saturating the sample in a positive direction and then measuring zero field moment after applying incremental reversal fields. Here the remanence coercivity reads a value of 43.5 kOe, which implies that there is indeed certain

amount of partially ordered or even soft phase accounting for the reduction of overall coercivity. This is possible because very small particle size might decrease the ordering parameter of FePt nanoparticles [21 - 22]. However, a kink persisted in the remanence curve and it inspired further study.

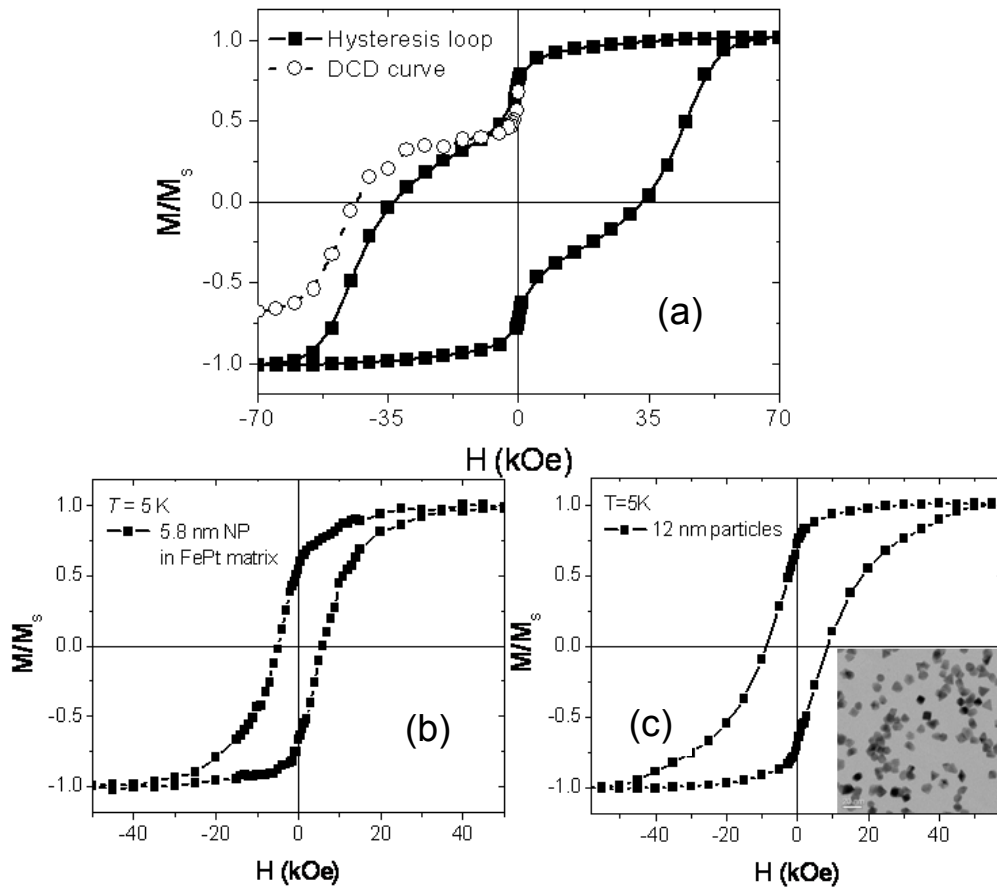


Figure 2. Reversal magnetization loops for (a) non-embedded 5.8nm L_{10} FePt nanoparticles (b) 5.8nm L_{10} FePt nanoparticles embedded in soft FePt matrix and (c) non-embedded 12nm L_{10} FePt nanoparticles, measured at 5 Kelvin. In (a) the solid line stands for a normal hysteresis loop including the signal contribution from both hard and soft phases, the dashed partial curve is a DC demagnetization remanence curve counting only the irreversible contribution.

What is more interesting is when we embedded 5.8nm $L1_0$ magnetic hard FePt nanoparticles into a magnetic soft FePt matrix film (A1 phase), the “kink” which existed in the magnetic reversal of non-embedded 5.8nm FePt nanoparticles disappeared, as shown in Fig.2 (b). Furthermore, we also successfully fabricated octahedral $L1_0$ FePt nanoparticles with a 12nm mean size and 10% size distribution. The “kink” was also disappeared or dramatically weakened in the magnetic reversal process of non-embedded 10 layers of 12nm $L1_0$ FePt nanoparticles, as shown in Fig.2 (c). In these two cases, the disappearances of the “kinks” are directly related to the significant reduction of the ratio of surface atoms over bulk atoms. For the case of embedding FePt nanoparticles in soft magnetic matrix, surface areas of FePt nanoparticles are greatly reduced by the soft magnetic matrix material. For the case of 12nm FePt nanoparticle, the fraction of surface atoms is only 3.2%, compare to the 28.3% surface atoms in 5.8nm FePt nanoparticle. These results strongly suggest that the “kink” comes from surface effect.

The “kink” might be suspected to come from those particles in A1 soft phase far from completely ordered. If this were the case, then nanoparticles in this sample would have been clearly categorized into two groups with distinct anisotropy difference. Given that these particles have a uniform size distribution, both of the two switches would have had similar temperature dependence. From the temperature dependent measurements shown in Fig. 3, it clearly shows that the magnetization

switching which happened at high field has strong temperature dependence, which is normal for magnetization reversal determined by magnetocrystalline anisotropy. However, the kinks are all due by a field around -2000 Oe and nearly independent of temperature.

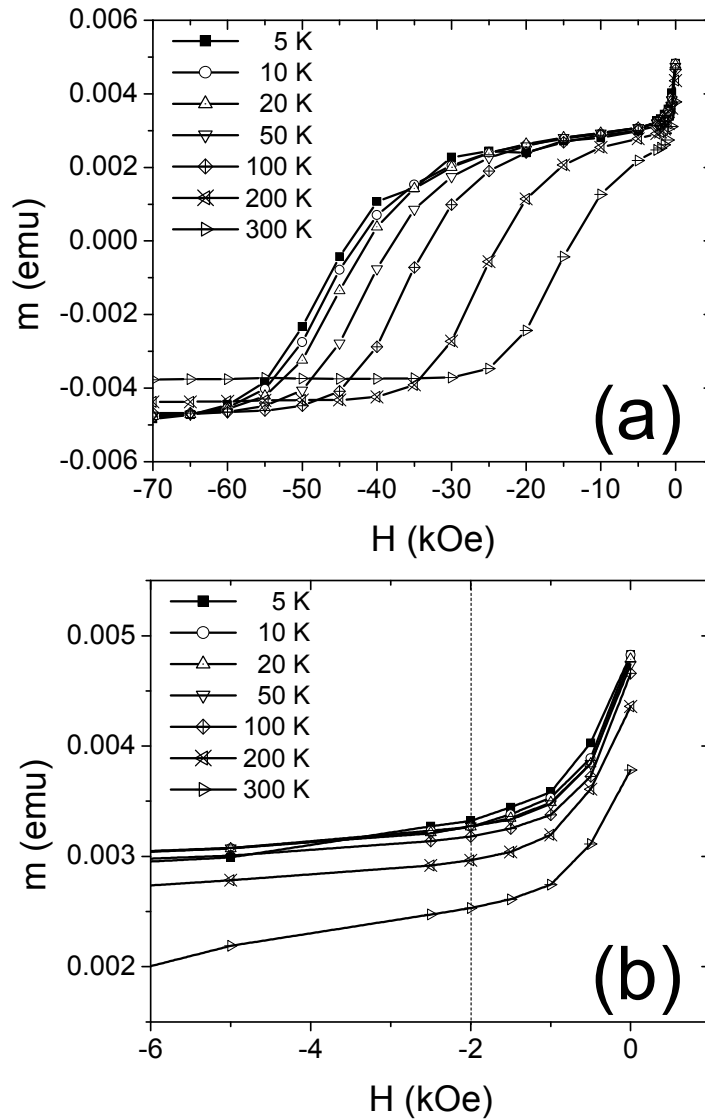


Figure 3. DCD remanence curves of 5.8nm L1₀ FePt nanoparticles as a function of measurement temperature. Figure (b) is a zoom-in of the kink area showing in figure (a) at low fields.

As a comparison the percentages of moments switched at -2000 Oe and -20000 Oe are plotted in Fig. 4. The percentages were calculated by dividing half of the moment drop after applying the reversal fields by the corresponding remanence moment for every measurement temperature. Clearly a gradual increase of moment switching happened at -20000 Oe as a result of thermal agitation. Moments switched at -2000 Oe have a percentage of 16%, independent of temperature. This result implies that the kinks found on the DCD curves can not be attributed to lower degree of chemical ordering. Instead, they come from surface magnetic moment reversal governed by surface anisotropy.

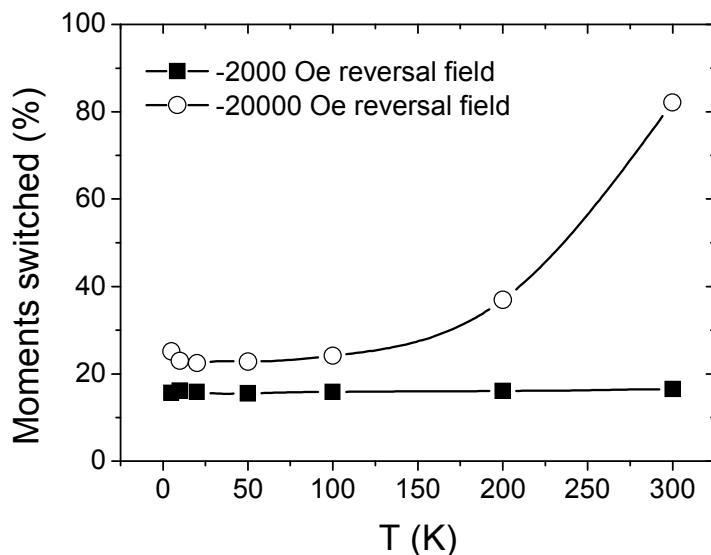


Figure 4. Comparison between moments switched at reversal fields of -2000 Oe and -20000 Oe (5.8nm $L1_0$ FePt nanoparticles). Up to -2000 Oe there are about 16 % of

all the moments switched and the switching is independent of temperature. Around -20000 Oe the percentage of switched moments is a function of temperature.

These magnetic moments experience an anisotropy associated with the broken symmetry of their crystal environment. When this surface anisotropy is comparable to or larger than exchange coupling interaction, surface moments will favor a full alignment along surface anisotropy direction. As a consequence, there will be jump(s) on magnetization curves [23]. The validity of the surface anisotropy assumption also lies in such an understanding that bulk anisotropy energy in FePt system is not simply a result of Néel model or directly due to the tetragonal distortion. Instead, the magnetocrystalline anisotropy energy comes from the polarization of Pt atoms due to the hybridization between Pt 5d and Fe 3d states, and the strong spin-orbit coupling in 5d electrons of Pt [24]. For the interior part every platinum atom has eight iron atoms as its nearest neighbors. On the contrary surface platinum atom has at most six iron atoms as its nearest neighbors as shown in Fig. 5a, four of which are surface iron atoms. Therefore, the polarization of Pt atoms and the interaction between Pt and Fe atoms becomes weaker from interior to the surfaces, which is crucial to the large magnetocrystalline anisotropy. As a result, the magnetocrystalline anisotropy must have a much reduced value at the eight {111} surfaces [25].

The next question is what is the direction of surface anisotropy on the {111} planes of octahedral $L1_0$ FePt nanoparticles. As mentioned earlier the surface atoms have a percentage of 28.3 % of all the atoms in the typical 5.8nm FePt nanoparticle with an octahedron shape. The magnetic moments are carried mostly by iron atoms which also have a percentage of 28.3 % at the surfaces. Because the {111} planes have an angle of 36.3° with the [001] easy axis [26], for the case of transverse surface anisotropy, 28.3% surface moments aligned perpendicular to {111} planes (Fig. 5b) should contribute 16.8% of the remanence. On the other hand, if the surface anisotropy is in-plane, 28.3% surface moments aligned parallel to {111} planes should contribute 22.8% to the remanence. Compare this with the experimental data of 16% contribution to the remanence, it is reasonable to claim that the surface anisotropy has an easy axis that is perpendicular to {111} planes, i.e. it is a transverse surface anisotropy. This partial contribution to the remanence can be considered as a “magnetic ineffective layer” effect as compared to the “magnetic dead layer effect”, which accounts for a reduced saturation magnetization due to surface effect [27].

The magnitude of surface anisotropy can be estimated from the saturation fields of the kinks. From Fig. 3, the switching of surface spins completes by the reversal field of -2000 Oe. Using the saturation magnetization of $Fe_{50}Pt_{50}$ alloy (1100 emu/cc or 1.1×10^6 A/m) we can estimate the surface anisotropy energy to be about 4×10^{-2} erg/cm² or 4×10^{-5} J/m².

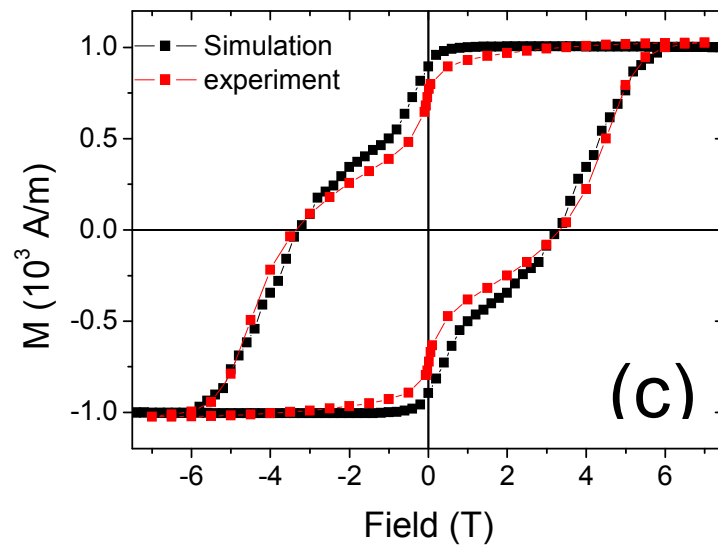
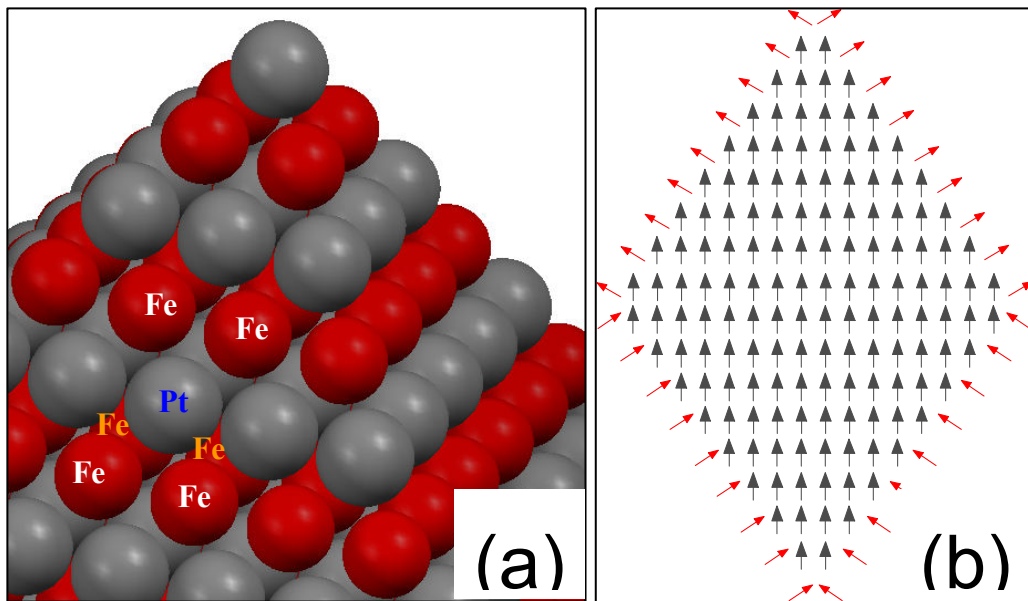


Figure 5. (Color online) (a) The chemical environment of a surface platinum atom (blue color) in the octahedral L₁₀ phase FePt nanoparticle. Four of the six iron atoms are on the surface (white color) and the other two are interior (orange color). (b) The remanence state of one octahedral L₁₀ FePt nanoparticles with transverse surface

anisotropy. Here arrows represent the moments from iron atoms and all platinum atoms have been omitted for clarity. Red arrows are surface moments and black arrows are interior moments, respectively. (c) 3D micro-magnetic simulated hysteresis loop of 5.8 nm L1₀ FePt nanoparticles using the model described in Fig. 5 (a) and (b), compared to experimental measurement.

To further confirm that the surface anisotropy model works for the switching behavior of 5.8 nm L1₀ FePt nanoparticles, a 3D micro-magnetic simulation was performed using OOMMF 1.2 [28]. The 3D magnetic structure of FePt nanoparticles are described shown in Fig. 5 (a) and (b). To compare with the experimental results measured at 5K, thermal effects were ignored. Saturation magnetization for FePt was $M_s=1.1 \times 10^6$ A/m. The damping coefficient used was $\alpha=0.5$ to reach a relatively fast converge. The exchange constants were $A=6 \times 10^{-12}$ J/m for interior moments and $A=1.2 \times 10^{-13}$ J/m for moments on the surface and interface between surface and interior moment. The anisotropy constants were $K=3.1(1 \pm 0.24) \times 10^6$ J/m³ for interior moment and surface anisotropy was $K=4 \times 10^{-5}$ J/m² for surface moment. The exchange length $L_{ex}=(A/K)^{1/2}$ were calculated to be 1.4 nm for interior moment and 1 nm for surface moment. Therefore, a 0.5 nm³ simulation cell size was chosen to provide sufficient resolution. Smaller cell sizes give the same results. This simulation included 70 L1₀ FePt nanoparticles with a practical anisotropy field distribution. Magnetic static energy inside each

nanoparticles was included in the simulation, but the weak magnetic static interactions among nanoparticles were ignored. A Gaussian distribution with 24% standard deviation of the anisotropy constants of L1₀ FePt nanoparticles and a 23.7° random distribution of easy axis of L1₀ FePt nanoparticles relative to the external field were included to consider the practical experiments conditions. The simulation successfully reproduced the two-step magnetization switching behavior which matched well with the experimental result, as shown in Fig. 5 (c).

In the simulation, the exchange constants $A=6\times 10^{-12}$ J/m for interior moments is close to the experimental data [29]. But the exchange constants $A=1.2\times 10^{-13}$ J/m for surface moments are much smaller. However the weak exchange constant on surface is understandable. Kurzweil et al recently reported [30] that the exchange coupling becomes extremely weak when the thickness of magnetic metal (Fe, Co and Ni) films is reduced to several atomic layers, which suggests that the exchange constant should be much smaller in a 2D system than 3D system. It is also supported by the observation that magnon energies in the Fe monolayer are much smaller than those in the bulk Fe [31].

In conclusion, we provided an experimental evidence and micromagnetic simulation support of the existence of surface anisotropy in 5.8nm octahedral L1₀ FePt nanoparticles. Surface moments on the eight {111} faces are confined in the transverse surface anisotropy direction and switch independently upon applying reversal magnetic fields. The existence of surface anisotropy in octahedral FePt

nanoparticles has influenced the overall reversal magnetization process and reduces their switching field, which might be useful in addressing the writability issue faced by current magnetic recording industry.

This work was performed as part of the Information Storage Industry Consortium (INSIC) program in Heat Assisted Magnetic Recording (HAMR), with the support of the U. S. Department of Commerce, National Institute of Standards and Technology, Advanced Technology Program, Cooperative Agreement Number 70NANB1H3056. Seagate Technology and Heraeus Corp. are acknowledged for partial financial support. We thank Dr. J. Bai and Mr. Y. Xu for fruitful discussion.

Reference:

-
- [1] D. Weller and A. Moser, *IEEE Trans. Magn.* **35**, 4423 (1999)
 - [2] I. Zutic, J. Fabian, S. Das Sarma, *Rev. Mod. Phys.* **76**, 323 (2004)
 - [3] L. Néel, *J. Phys. Radium*, **15**, 225 (1954)
 - [4] S. D. Bader, *Rev. Mod. Phys.* **78**, 1 (2006)
 - [5] M. Jamet, W. Wernsdorfer, C. Thirion, D. Mailly, V. Dupuis, P. Mélinon, and A. Pérez, *Phys. Rev. Lett.*, **86**, 4676 (2001)
 - [6] For example, see C. Liu, E. R. Moog, and S. D. Bader, *Phys. Rev. Lett.* **60**, 2422 (1988); H. C. Mireles, and J. L. Erskine, *Phys. Rev. Lett.* **87**, 037201 (2001)
 - [7] H. Kachkachi, H. Mahboub, *J. Mag. Mag. Mater.* **278**, 334 (2004)
 - [8] D. A. Garanin and H. Kachkachi, *Phys. Rev. Lett.* **90**, 065504 (2003)
 - [9] Y. Komorida, M. Mito, H. Deguchi, S. Takagi, A. Millan, N. J. O. Silva and F. Palacio, *Appl. Phys. Lett.* **94**, 202503 (2009)

-
- [10] M. A. Willard, L. K. Kurihara, E. E. Carpenter, S. Calvin and V. G. Harris. *International Materials Reviews*, **49**, 125 (2004)
- [11] C. Binns, K. N. Trohidou, J. Bansmann, S. H. Baker, J. A. Blackman, J-P Bucher, D. Kechrakos, A. Kleibert, S. Louch, K-H Meiwes-Broer, G. M. Pastor, A. Perez, and Y. Xie, *J. Phys. D: Appl. Phys.* **38**, R357 (2005)
- [12] K. Wegner, P. Piseri, H. Vahedi Tafreshi, and P. Milani, *J. Phys. D: Appl. Phys.* **39**, R439 (2006)
- [13] O. A. Ivanov, L. V. Solina, V. A. Demshina, L. M. Magat, *Fiz. Metal. Metalloved.* **35**, 92 (1973)
- [14] S. Sun, C. B. Murray, D. Weller, L. Folks, A. Moser, *Science* **287**, 1989 (2000)
- [15] H. Zeng, J. Li, J. P. Liu, Z. L. Wang, S. Sun, *Nature* **420**, 395 (2002)
- [16] J. M. Qiu, J. P. Wang, *Appl. Phys. Lett.*, **88**, 192505 (2006)
- [17] J. M. Qiu, J. P. Wang, *Adv. Mater.* (2007, in press)
- [18] J. M. Qiu, J. M. Bai, J. P. Wang, *Appl. Phys. Lett.* **89**, 222506 (2006)
- [19] T. Shima, K. Takanashi, Y. K. Takahashi, K. Hono, *Appl. Phys. Lett.* **85**, 2571 (2004)
- [20] T. Shima, K. Takanashi, Y. K. Takahashi, K. Hono, *Appl. Phys. Lett.* **88**, 063117 (2006)
- [21] Y. K. Takahashi, T. Ohkubo, M. Ohnuma, and K. Hono, *J. Appl. Phys.* **93**, 7166 (2003)
- [22] R. V. Chepulskii and W. H. Butler, *Phys. Rev. B.* **72**, 134205 (2005)
- [23] H. Kachkachi and M. Dimian, *Phys. Rev. B.* **66**, 174419 (2002)
- [24] G. H. O. Daalderop, P. J. Kelly, and M. F. H. Schuurmans, *Phys. Rev. B.* **44**, 12054 (1991)

-
- [25] T. Burkert, O. Eriksson, S. I. Simak, A. V. Ruban, B. Sanyal, L. Nordstrom and J. M. Wills, Phys. Rev. B. 71, 134411 (2005)
- [26] J. P. Wang, J. M. Qiu, T. A. Taton, B. S. Kim, IEEE Trans. Magn. **42**, 3042 (2006)
- [27] L. N. Liebermann, D. R. Fredkin, and H. B. Shore, Phys. Rev. Lett. **22**, 539 (1969)
- [²⁸] M. Donahue and D. Porter, The Object Oriented MicroMagnetic Framework (OOMMF) project at ITL/NIST, <http://math.nist.gov/oommf/>.
- [²⁹] S. Okamoto, N. Kikuchi, O. Kitakami, T. Miyazaki, Y. Shimada, K. Fukamichi, Phys. Rev. B. **66**, 024413 (2002)
- [³⁰] N. Kurzweil, E. Kogan and A. Frydman, Phys. Rev. Lett. **102**, 096603 (2009)
- [³¹] J. Prokop, W. X. Tang, Y. Zhang, I. Tudosa, T. R. F. Peixoto, Kh. Zakeri and J. Kirschner, Phys. Rev. Lett. 102, 177206 (2009)

Appendix C: Studies on SmCo_5 with ultrahigh crystalline anisotropy

1. Film Composition, Substrate Temperature and Thickness Dependence of $\text{Sm}(\text{Co,Cu})_5/\text{Ru}$ thin films with perpendicular anisotropy

Xiaoqi Liu¹, Haibao Zhao¹, Yukiko Kubota² and Jian-Ping Wang^{1*}

1. The Center for Micromagnetics and Information Technologies, Department of Electrical and Computer Engineering, University of Minnesota, Minneapolis, U.S

2. Seagate Research, 1251 Waterfront Place, Pittsburgh, PA 15222, U.S

*Corresponding author, contact email: jpwang@umn.edu

Abstract

SmCo_5 thin film is considered a promising candidate for future high areal density perpendicular recording media because of the demand of media with extremely small but thermally stable grains. In this paper $\text{Sm}(\text{Co,Cu})_5$ films with perpendicular anisotropy on Ru underlayer were successfully fabricated by DC sputtering with relatively small grain size. Zero in-plane coercivity and 11 kOe out-of-plane coercivity were reached on $\text{Ta}(3\text{nm})/\text{Sm-Co-Cu}(10\text{nm})/\text{Ru}(20\text{nm})/\text{Ta}(4.2\text{nm})$ thin

films. Studies about the effects of deposition temperature, film composition and film thickness on the magnetic properties of SmCoCu films were performed.

I. Introduction

Extremely high density recording (EHDR) requires magnetic thin film media with very small grain size (5nm or less) [1-3]. To maintain its thermal stability, magnetic media with very small grain size must use magnetic materials with ultrahigh anisotropy energy [1]. Therefore, SmCo₅ alloy becomes a very attractive candidate with anisotropy constant larger than 10⁸erg/cm³ [4].

SmCo₅ alloy has been extensively studied as the material for permanent magnets since 1960s [5]. Since SmCo₅ attracted much attention as a potential candidate for future thin film media, many researchers reported the fabrication of Sm-Co film with in-plane anisotropy [6 – 13]. Recently, following the application of perpendicular recording, SmCo₅ thin film with perpendicular anisotropy was obtained on Cu underlayer [14 – 16]. In their studies, Cu underlayer was very essential for the perpendicular anisotropy. SmCo₅ (001) texture could not be achieved without a Cu underlayer, because Cu diffused into the Sm-Co layer and had a key effect on the microstructure controlling. There may be a concern to use Cu underlayer for its application for perpendicular recording media. The mean grain size of the Cu underlayer is as large as 100-200nm as reported in [16]. Cu addition in the Sm-Co permanent magnets has been widely studied. It has been reported that

Cu makes the SmCo_5 phase stable, makes the $\text{Sm}_2\text{Co}_{17}$ phase unstable [17-20].

Although both saturation magnetization value and anisotropy constant decrease when the Cu addition is over certain value, Sm-Co-Cu still can form high anisotropy $\text{Sm}(\text{Co,Cu})_5$ phase if with a proper Cu concentration [21].

In this paper, hcp phase Ru(0002) was used as a underlayer instead of Cu, because Ru can form films with much smaller grain size than Cu. And by co-sputtering Sm, Co and Cu targets, $\text{Sm}(\text{Co,Cu})_5$ (0001) textured films on Ru underlayer were successfully fabricated. The effects of deposition temperature, film composition and film thickness on the magnetic properties of SmCoCu films were studied systematically.

II. Experiment

The Ta(3nm)/Sm-Co-Cu-(X nm)/Ru(20 nm)/Ta(4.2nm) films were deposited on glass substrates with a conventional dc magnetron sputtering system. The base pressure of this system was 2×10^{-7} Torr. And the sputtering gas pressure was 3×10^{-3} Torr. The bottom Ta layer was deposited for texture control and the cap Ta layer was deposited as a protective layer against oxidation. The Sm-Co-Cu layer was deposited by co-sputtering Sm, Co and Cu targets. The deposition temperature of Sm-Co-Cu layer was controlled by heating the substrates. All other layers including cap and under layers were prepared at room temperature. The thickness of Sm-Co-Cu magnetic layer ranged from 5nm to 20nm.

Magnetic properties of the films were measured by a vibrating sample magnetometer (VSM), and a superconducting quantum interference device (SQUID). The crystallographic texture of the films was investigated by X-ray diffraction (XRD) with Cu K α radiation. Transmission electron microscope (TEM) and Rutherford backscattering spectroscopy (RBS) were also used to study the structure and composition of the Sm-Co-Cu films.

III. Results and Discussion

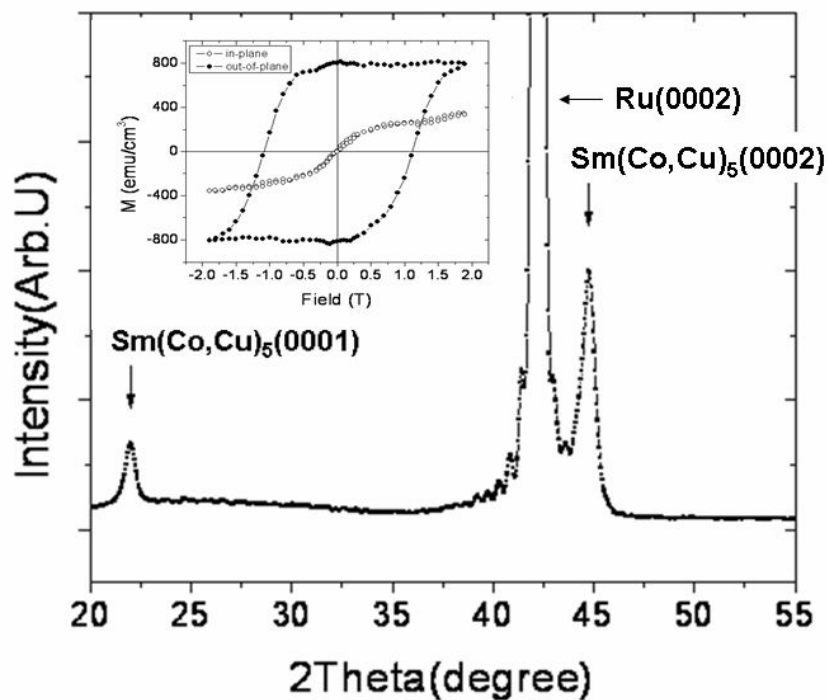


Figure1. XRD pattern of

Ta(3nm)/Sm₁₄Co₅₈Cu₂₈(10nm)/Ru(4nm)/Ru(16nm)/Ta(4.2nm)/glass. The inset shows its magnetic hysteresis loops in out-of-plane (black dots) and in-plane (white dots) directions.

Figure 1 shows the XRD pattern and magnetic hysteresis loops of sample Ta(3nm)/Sm₁₄Co₅₈Cu₂₈(10nm)/Ru(4nm)/Ru(16nm)/Ta(4.2nm)/glass. The substrate temperature for this SmCoCu layer deposition is 350 °C. The composition of Sm-Co-Cu film is determined from RBS testing. Here the double-Ru-layer is used to decrease the grain size and obtain better grain isolation in the Sm-Co-Cu layer. Only two peaks at 21.9° and 44.8° are observed besides the underlayer Ru(0002) peak in the XRD pattern, corresponding to Sm(Co,Cu)₅ (0001) and (0002) peaks respectively, which indicates that the Sm-Co-Cu layer is in the Sm(Co,Cu)₅ phase. The lattice constant in (0001) direction of this Sm(Co, Cu)₅ film is 1.5% larger than that of bulk SmCo₅ [22], which is caused by the addition of Cu [23]. The XRD measurement shows that the easy axis of Sm-Co-Cu layer ((0001) direction) is in the perpendicular direction. The grain size of Sm-Co-Cu layer is 17nm, calculated from the full width of half maximum (FWHM) of the Sm(Co,Cu)₅ (0001) peak, which is consistent to the TEM observation. This grain size is much smaller than that in the literature using Cu underlayer [14-16].

The hysteresis loops (inset of Figure 1) show that the remanence squareness (M_r/M_s) and coercivity of Sm-Co-Cu film in the out-of-plane direction were 1 and 11 kOe, respectively. While its remanence and coercivity in the film plane direction were both zero. This result reveals that the easy-axis direction of the Sm-Co-Cu film perpendicular to the film plane, which is consistent with the XRD measurement.

From the hysteresis loops in two directions, we can approximately estimate the H_k value of the sample, which is larger than 200 kOe. A precise high-field measurement is under way.

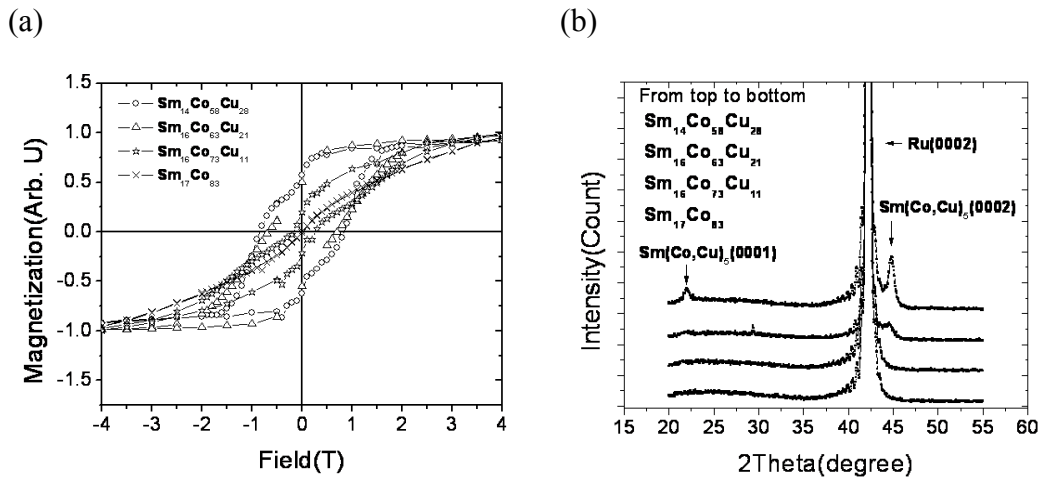


Figure 2 (a) Magnetic hysteresis loops in the perpendicular direction and (b) XRD patterns of samples with different Sm-Co-Cu compositions. (XRD results from top to bottom represent sample with composition: $\text{Sm}_{14}\text{Co}_{58}\text{Cu}_{18}$, $\text{Sm}_{16}\text{Co}_{63}\text{Cu}_{21}$, $\text{Sm}_{16}\text{Co}_{73}\text{Cu}_{11}$, and $\text{Sm}_{17}\text{Co}_{83}$.)

Figure 2 shows the out-of-plane magnetic hysteresis loops and XRD spectra of samples with different Sm-Co-Cu compositions. Here Sm/(CoCu) ratio was kept constant and Co/Cu ratio was varied. The magnetic properties indicates that Sm-Co-Cu with higher Cu composition have larger remanence and coercivity. The XRD results show that with proper Cu concentration, Sm-Co-Cu layer can reach

better crystallization. This is supported by the studies of Cu addition in bulk SmCo_5 materials [20, 21]. Attempts to fabricate Sm-Co film with perpendicular anisotropy without Cu's addition were failed, which also supports that Cu may exist in the lattice to stabilize SmCo_5 phase. This result indicates that Cu's addition is very important for the realization of the (0001) texture in Sm-Co-Cu films.

“Kinks” are observed around the remanence points in the hysteresis loops, which may be due to a soft phase existing in the Sm-Co-Cu layer. A possible explanation for the formation of this soft phase is the oxidization of the Sm-Co-Cu layer. But the oxidization is more likely to happen in a short period after the deposition. After this period, Sm-Co-Cu samples are stable with Ta top layer. Further studies are needed to get more solid conclusion.

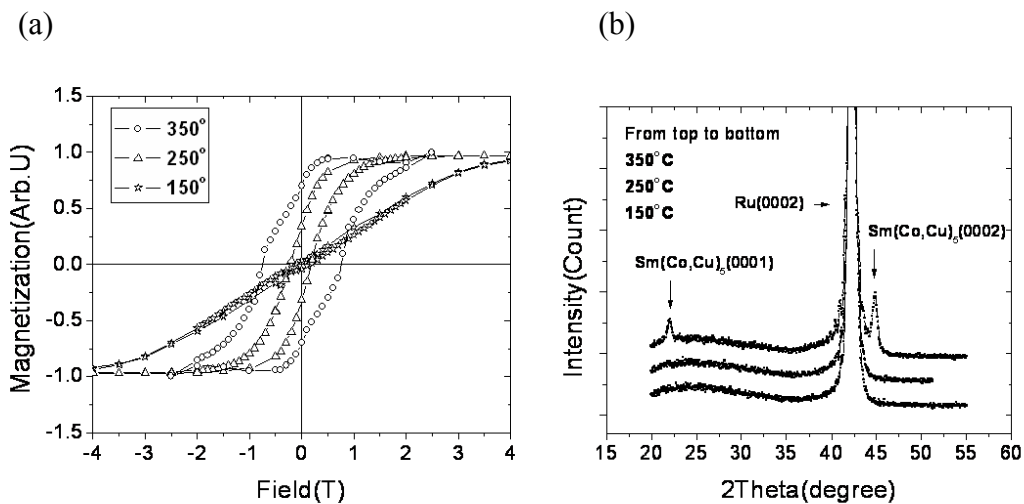


Figure 3 (a) Magnetic hysteresis loops and (b) XRD patterns of $\text{Sm}_{14}\text{Co}_{58}\text{Cu}_{28}$.

(XRD results from top to bottom represent sample with deposition temperature:

350°C, 250°C, and 150°C.)

Figure 3 shows the out-of-plane magnetic hysteresis loops and XRD patterns of samples prepared at various substrate temperatures. While the hysteresis loops of samples prepared with substrate temperature of 250°C and 350 °C show the behavior with an out-of-plane easy axis, hysteresis loop of sample prepared with substrate temperature of 150°C, shows the behavior with an in-plane easy axis. As seen in XRD patterns, $\text{Sm}(\text{Co,Cu})_5$ (0001) and (0002) peaks are present only for the sample prepared at 350 °C substrate temperature. Both the magnetic measurements and the XRD results clearly show that a relatively high deposition temperature is required to form $\text{Sm}(\text{Co,Cu})_5$ (0001) texture. “Kinks” are also observed in some hysteresis loops.

As revealed in figure 2 and 3, Cu’s addition shows the similar effect as increasing the deposition temperature, which may help form SmCo_5 phase. This implies that Cu’s addition in the Sm-Co-Cu layer may lower the crystallization temperature that is required for Sm-Co-Cu to form $\text{Sm}(\text{Co,Cu})_5$ (0001) crystal structure, and stabilize the $\text{Sm}(\text{Co,Cu})_5$ phase[20].

Figure 4 shows the out-of-plane magnetic hysteresis loops of $\text{Sm}_{14}\text{Co}_{58}\text{Cu}_{28}$ (0001) films on pure Ru(0002) underlayer with different thicknesses. The remanence squareness of four loops were all close to 1, which suggests that all Sm-Co-Cu films were strongly (0001) textured. However, the coercivity of

Sm-Co-Cu film clearly showed its thickness dependence. With the increase of Sm-Co-Cu film thickness from 5nm to 10nm, its coercivity increases from 4 to 11

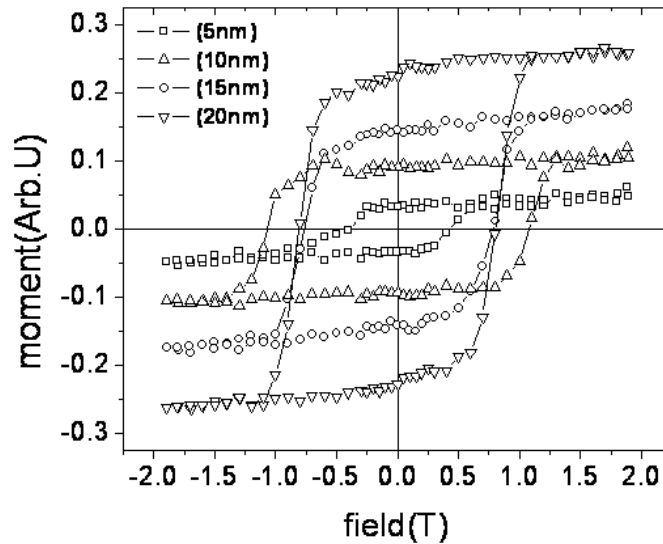


Figure 4 Magnetic hysteresis loops in the out-of-plane direction of Sm₁₄Co₅₈Cu₁₈ films on pure Ru (0002) underlayer with different thicknesses.

kOe. But a further increase of film thickness to 15nm, results in the drop of coercivity down to 8 kOe. After this, more thickness increase (20nm) doesn't affect the film coercivity. The thickness dependence of the coercivity of Sm₁₄Co₅₈Cu₁₈ film could be explained by considering the effects of grain growth and magnetic dead layer at the interface of Sm-Co-Cu layer and Ru underlayer. The existence of magnetic dead layer could be caused by strain stress [24] or ion etching during sputtering [25]. The strain stress is induced by the lattice misfit between Sm(Co,Cu)₅ layer and Ru underlayer. The iron etching comes from Ar⁺ ion in the plasma. In this

case, strain stress should be the main reason for the dead layer because of the 8% percent lattice misfit between $\text{Sm}(\text{Co}, \text{Cu})_5(0001)$ plane and $\text{Ru}(0002)$ plane. The dead layer thickness, estimated by fitting M_s vs. $1/\text{Thickness}$ curve, was around 2.2 nm. When the film was 5nm, the coercivity of entire film was lowered down by the magnetic dead layer which is low coercivity or even non-magnetic layer. If the Sm-Co-Cu layer is thicker (10nm), the influence of dead layer is smaller. Therefore the coercivity of 10 nm SmCoCu film increased. When the film is thicker, 15 or 20nm, the film's column growth may be weakened. Small grains may begin to agglomerate to big grains, which caused the coercivity of the entire film to decrease. Based on the balance of the above two factors, the 10 nm SmCoCu film shows the highest coercivity.

IV. Conclusion

In this work, highly ordered SmCo_5 phased Sm-Co-Cu thin film samples with high perpendicular anisotropy were prepared. The study of the effects of Cu addition and deposition temperature showed both of them could help the crystallization of $\text{Sm}(\text{Co}, \text{Cu})_5(0001)$ films. Oxidation problem is still a concern for the application of this SmCo_5 phased Sm-Co-Cu compound. The thickness dependence of SmCoCu films was explained by considering effects of grain agglomeration and magnetic dead layer at the interface of Sm-Co-Cu layer and Ru underlayer.

V. Acknowledgement

This work is partially support by the Seagate Research, Information & Storage Industry Consortium (INSIC) EHDR program. Authors also thank the support from Dr. Bin Lu and Dr. Ganping Ju from Seagate Research.

Reference:

1. M.F. Doerner, et al., IEEE Trans. Magn. 36, 43 (2000)
2. J.P. Wang, Y.Y. Zou, C.H. Hee, T.C. Chong, IEEE Trans. Magn. 39(4), 1930 (2003)
3. J.P. Wang, W.K. Shen, J.M. Bai, IEEE Trans. Magn. 43(2), 682 (2007)
4. K. J. Strnat, in Ferromagnetic Materials, edited by E. P. Wohlfarth and K. H. J. Buschow (North-Holland, Amsterdam, 1988), Vol. 4, Chap. 2, pp. 131-209, and references cited therein.
5. D.K. Das, IEEE Trans. Magn. 5, 214 (1969)
6. E.E. Fullerton, J.S. Jiang, C. Rehm, C.H. Sowers, S.D. Bader, J.B. Patel, and X.Z.Wu, Appl. Phys. Lett. 71, 1579 (1997)
7. R. Rani, F.J. Cadieu, X.R. Qian, W.A. Mendoza, S.A. Shaheen, J. Appl. Phys. 81, 5634 (1997)
8. Y. Liu, R.A. Thomas, S.S. Malhotra, Z.S. Shan, S.H. Liou, D.J. Sellmyer, J. Appl. Phys. 83, 6244 (1998)

9. V. Neu, S.A. Shaheen, *J. Appl. Phys.* 86, 7006 (1999)
10. A. Singh, R. Tamm, V. Neu, S. Fähler, C.G. Oertel, W. Skrozki, L. Schultz, and B. Holzapfel, *J. Appl. Phys.* 97, 093902 (2005)
11. A. Singh, V. Neu, R. Tamm, K. Subba Rao, S. Fähler, W. Skrozki, L. Schultz, and B. Holzapfel, *Appl. Phys. Lett.* 87, 072505 (2005)
12. E.M.T. Velu and D.N. Lambeth, *IEEE, Trans. Magn.*, Vol. 28, No. 5, 3249 (1992)
13. S. Takei, S. Shomura, A. Morisako, M. Matsumoto, and T. Haeiwa, *J. Appl. Phys.* 81, 4674 (1997)
14. J. Sayama, T. Asahi, K. Mizutani, and T. Osaka, *J. Phys. D* 37, L1 (2004)
15. S. Takei, A. Morisako, and M. Matsumoto, *J. Magn. Magn. Mater.* 272-276, 1703 (2004)
16. I. Kato, S. Takei, X. Liu, and A. Morisako, *IEEE Trans. On Magn.* Vol. 42, No.10 (2006)
17. F. Hofer, *IEEE Trans. On Magn.* Vol. 6, No. 221 (1970)
18. K. Kamino, Y. Kimura, T. Suzuki, Y. Itayama, *Trans. Jpn. Inst. Met.* 14, 135 (1973)
19. A.J. Perry, *J. Less-Common Met.* 51, 153 (1977)
20. W.Y. Zhang, X.D. Zhang, Y.C. Yang, B.G. Shen, *J. Alloy. Compd.* 353, 274 (2003)
21. E. Lectard, C.H. Allibert, R. Ballou, *J. Appl. Phys.* 75, 6277 (1994)

-
22. F. Meyer-Liautaud, S. Derkaoui, etc, J. Less-Common Met. 127, 231 (1987)
 23. J.C. Tellez-Blanco, et. al., Journal of Alloys and Componds, 281, 1-5 (1998)
 24. Kei Hayashi, et. al., J. Phys. Soc. Jpn., Vol. 73 No. 9, pp. 2550-2553 (2004)
 25. Weimin Si, et. al., J. Appl. Phys. 97, 10N901 (2005)

2. Polycrystalline Sm(Co,Cu)₅ Films with Perpendicular Anisotropy

Grown on (0002) Ru(Cr)

Xiaoqi Liu¹, Haibao Zhao¹, Yukiko Kubota² and Jian-Ping Wang^{1*}

¹The Center for Micromagnetics and Information Technologies (MINT) and
Department of Electrical and Computer Engineering, University of Minnesota,

Minneapolis, MN55455

²Seagate Research, 1251 Waterfront Place, Pittsburgh, PA 15222

*Corresponding author: Email: jpwang@umn.edu; Tel: 612-625-9509

Abstract

Polycrystalline Sm-Co-Cu films with SmCo₅ phase and (0001) texture using a DC magnetron sputtering process were successfully fabricated directly on (0002) Ru(Cr) underlayer on heated glass substrates at 350 °C. The mean grain size of Sm(CoCu)₅ layer is 17 nm, the smallest ever reported on SmCo₅ film with perpendicular anisotropy. Strong exchange-coupling between grains, as indicated by the coercivity squareness, was found in the obtained Sm(Co,Cu)₅ films. An estimated perpendicular magnetic anisotropy constant, as high as 1.4×10^8 erg/cm³, was achieved on these films. An “unusually” high perpendicular coercivity (11 kOe) was

found on these exchange-coupled polycrystalline $\text{Sm}(\text{Co,Cu})_5$ films. This was explained by a pinning-site model which was supported by the measurement of the coercivity angular dependence.

1. Introduction

SmCo_5 is a very attractive magnetic material because of its ultrahigh uniaxial magneto-crystalline anisotropy ($2 \times 10^8 \text{ erg/cm}^3$) [1]. Its earliest application was for high-energy permanent magnets [2]. SmCo_5 is a promising candidate for the future perpendicular magnetic recording (PMR) thin film media when the magnetic recording areal density approaches 1 Terra bits/inch² and beyond. This density requires recording media's minimum thermally-stable grain diameter to be less than 4 nm [3]. Although SmCo_5 thin film has been studied by many researchers, most have been fabricated with in-plane anisotropy [4-8]. For the application of extremely high areal density perpendicular recording, SmCo_5 films must be fabricated with (0001) texture, magnetic easy-axis in the out-of-plane direction. Previously, the epitaxial growth of Sm-Co films were only reported for a composition of $\text{Sm}_{22}\text{Co}_{78}$ which mainly consisted of Sm_2Co_7 phase [9, 10]. Singh *et al.* [11, 12] reported their success of epitaxial growth of $\text{SmCo}_5(11-20)$ film on Cr/MgO(100) with in-plane anisotropy. Only until recently, SmCo_5 thin films with perpendicular anisotropy were obtained on Cu underlayers [13, 14]. However a Cu underlayer results in a large grain size of SmCo_5 layer. In ref. 13 and 14, a Cu underlayer was essential for

obtaining SmCo_5 with perpendicular anisotropy. Even a Ru/Cu/Ru sandwich underlayer was tried by Kato *et al.* [15] to reduce the grain size of Sm-Co layer, but the Cu sub-underlayer was still essential to obtain a perpendicular orientation of SmCo films.

The addition of Cu in the Sm-Co permanent magnets has been widely studied. It has been reported that Cu addition makes the SmCo_5 phase stable, and the $\text{Sm}_2\text{Co}_{17}$ phase unstable [16-19]. Although saturation magnetization value and anisotropy constant of SmCoCu samples decrease quickly when the Cu addition exceeds a certain value, Sm-Co-Cu still can form high anisotropy $\text{Sm}(\text{Co,Cu})_5$ phase[20]. Furthermore it has been reported that the addition of Cu improved the corrosion resistance of Sm-Co-Cu films [13].

In this study, we proposed to use Ru(Cr) as the underlayer, because both Ru and SmCo_5 have hex-type structure. The lattice mismatch between the atomic distance of Ru-Ru in the plane of Ru (0002) ($\sim 2.706\text{\AA}$) and Co-Co in the plane of SmCo_5 (0001) ($\sim 2.501\text{\AA}$) is about 8%. Introducing the small atom Cr into Ru lattice was expected to make the lattice mismatch smaller. Accordingly, Cr doped Ru (0002) should be a good underlayer for the epitaxial growth of SmCo_5 (0001) thin films. In particular, we expected that some of Cr atoms may diffuse into Ru grain boundaries to induce the growth of small and isolated Ru grains. In this paper we report the success in fabricating Sm-Co-Cu films with perpendicular anisotropy directly on Ru(Cr) underlayer. In addition, we report a study of the microstructures, crystalline

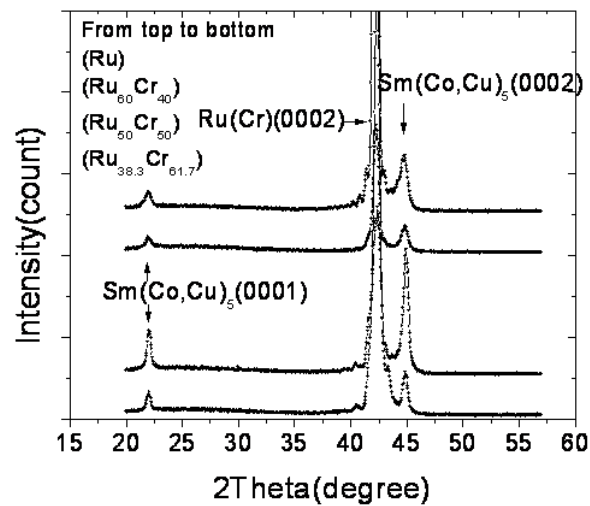
structures and magnetic properties of Sm-Co-Cu thin films grown on Ru(Cr) underlayers.

2. Experiments

All layers of the films were deposited by an eight-target DC magnetron sputtering system with a base pressure of less than 1×10^{-7} Torr. Thin films with structure Ta(3nm)/Sm-Co-Cu(10-20nm)/Ru(Cr)(X nm)/Ru(Cr)((20-X) nm)/Ta(4.2nm) (X= 4 or 10) were deposited onto glass substrates. The substrate temperature for the deposition of the Sm-Co-Cu layer was 350 °C, and all other layers were deposited at room temperature. Sm-Co-Cu layers were deposited by co-sputtering Sm, Co, and Cu targets. 4 nm and 16 nm Ru(Cr) layers were deposited at an Argon gas pressure of 6 mTorr and 3 mTorr, respectively. All other layers were prepared at a gas pressure of 3 mTorr. The double-Ru(Cr)-layer was used to improve the Ru(0002) texture with reduced grain size and better grain isolation [21]. The magnetic properties, crystalline structures and element compositions of our samples were measured by a vibrating sample magnetometer (VSM), a superconducting quantum interference device (SQUID), a transmission electron microscope (TEM), a Cu source X-ray diffractometer (XRD), and a rutherford backscattering spectroscopy (RBS), respectively.

3. Results and Discussion

(a)



(b)

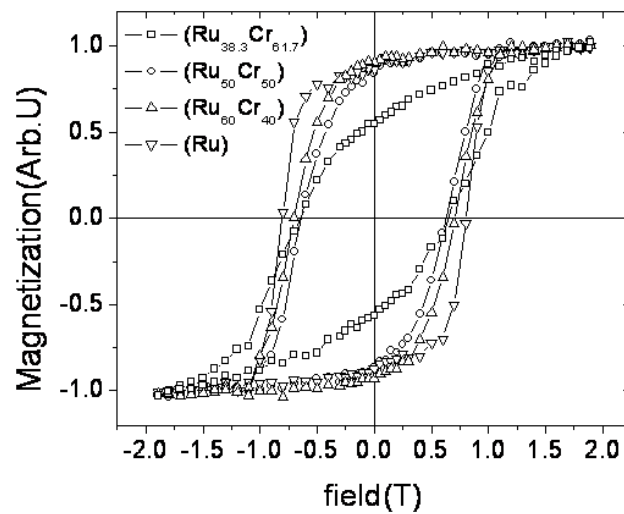


Figure 1 (a) XRD patterns and (b) Magnetic hysteresis loops in the out-of-plane direction of Sm-Co-Cu (20nm) films on Ru(Cr)(10nm)/Ru(10nm) underlayer with different Ru-Cr compositions.

Figure 1 shows (a) XRD patterns and (b) out-of-plane hysteresis loops of Sm-Co-Cu (20 nm) films on Ru(Cr)(10nm)/Ru(10nm) underlayers with different RuCr compositions. In Figure 1 (a), for Sm-Co-Cu films on all four Ru(Cr)/Ru underlayers, Ru(Cr)(0002) peaks are clearly seen. The peak position shifts from 42.21° to 42.34° and the full width of half maximum (FWHM) value increases, following the doping of Cr concentration from 0 to 61.3%. The change of Ru(Cr)(0002) peaks' position shows that the addition of Cr into Ru reduces the lattice constant of Ru(Cr) underlayer. The increase of FWHM indicates the small grain size. One interesting finding is that the higher Cr concentration doesn't change the RuCr from hex-texture to bcc-texture, due to the 10nm hcp (0002) textured Ru sublayer under the Ru(Cr) layer. This result is consistent with the observation of the increase of FWHM. Some of Cr atoms may have migrated into grain boundaries for samples with high Cr concentration. Besides the (0002) Ru(Cr) peak, diffraction peaks only at around 21.9° and 44.8° are clearly observed, which are corresponding to SmCo₅ (0001) and (0002) peaks respectively. No other peaks appear in the XRD patterns. This result suggests that these films are all strongly (0001) textured. Although the XRD results suggest all films were strongly oriented in (0001) direction, which is the easy axis of SmCo₅ compound, not all films showed typical easy axis hysteresis behavior in the out-of-plane direction (figure 1 (b)). The shapes of the hysteresis loops reveal that the Sm-Co-Cu films on Ru-Cr underlayer with less Cr have stronger (0001) texture. Since the addition of Cr in Ru reduces the

lattice constant in the Ru(Cr) (0002) plane, which makes the lattice mismatch between Ru(Cr) layer and Sm-Co-Cu layer smaller, this result indicates that a slightly larger lattice misfit may be better for the growth of Sm-Co-Cu (0001) texture. Also the possible diffusion of Cr in RuCr underlayer into the interface between SmCo₅ and Ru may degrade the (0001) texture of SmCo₅ film. Elements other than Cr can be tried in future to solve this problem.

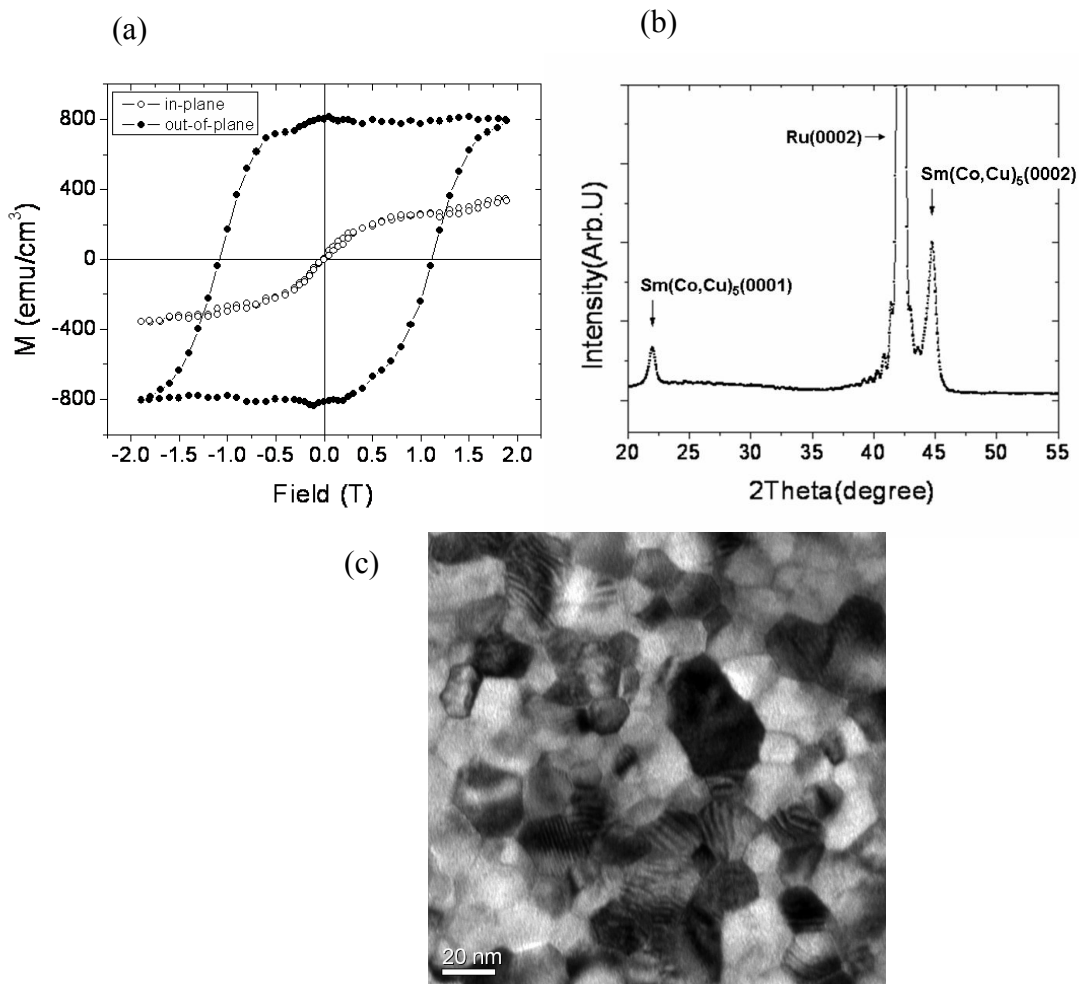


Figure 2. (a) Magnetic hysteresis loops, (b) XRD and (c) TEM image of Ta(3nm)/Sm-Co-Cu(10nm)/Ru(4nm)/Ru(16nm)/Ta(4.2nm)/glass

Figure 2 shows the magnetic hysteresis loops, XRD pattern and TEM image of a typical Sm-Co-Cu film with following multi-layer structure: Ta(3nm)/Sm-Co-Cu(10nm)/Ru(4nm)/Ru(16nm)/Ta(4.2nm)/glass. Figure 2 (a) clearly shows the magnetic easy axis is perpendicular to the film plane. In the out-of-plane direction, the film coercivity is about 11 kOe, and remanence squareness is almost 1. In the in-plane direction, the film shows a hard axis behavior with zero coercivity, which confirms the success of pure perpendicular orientation of Sm-Co-Cu thin film. The saturation magnetization of this Sm-Co-Cu film is 800 emu/cm^3 . Using the hysteresis loops along easy and hard directions, approximate the H_k of the sample is about 350 kOe, and the anisotropy constant of this sample was calculated to be around $1.4 \times 10^8 \text{ erg/cm}^3$. Both the tested M_s and estimated K_u values are smaller than the reported values for bulk SmCo_5 materials¹. Only two peaks at 21.9° and 44.8° are observed besides the underlayer Ru(0002) peak in the XRD pattern (figure 2 (b)), which correspond to SmCo_5 (0001) and (0002) peaks respectively, indicating that the Sm-Co-Cu layer is in the SmCo_5 phase. The lattice constant in (0001) direction of this $\text{Sm}(\text{Co}, \text{Cu})_5$ film is 1.5% larger than that of bulk SmCo_5 [22], which is caused by the addition of Cu atoms[23]. The XRD measurement again confirms that the magnetic easy axis of Sm-Co-Cu layer is in the perpendicular direction. The mean thickness of crystallized grains in Sm-Co-Cu layer is estimated as 8.6 nm from the FWHM value of the

Sm(Co, Cu)₅ (0002) peak. The mean grain size obtained from planar-view TEM observation is 17 nm, the smallest ever reported on SmCo₅ film with perpendicular anisotropy, as shown in Figure 2 (c). This result means that the grain size is much smaller using Ru underlayer than that reported in the literature using Cu underlayer [13-15]. It is worth noting that the substrate temperature for depositing Sm-Co-Cu layer is 350 °C in this report. The deposition time is about 260 seconds. During this period, the Ru grains may coalesce and form larger grains. It is reasonable to expect that the Sm-Co-Cu grain size can be further reduced in the future if the substrate temperature can be reduced for the SmCoCu layer deposition. The mean grain size of hex-textured (0002) Co alloy layer grown on (0002) Ru underlayer at room temperature is reported as small as 7 – 8 nm, which is being used in current perpendicular media product.²⁴ Another interesting observation is that many hexagonal shape grains can clearly be identified in the TEM image. This result indicates the growth of fully crystallized Sm-Co-Cu grains, which have the hexagonal crystalline structure.

The composition of the Sm-Co-Cu films was tested by RBS as shown in Figure 3. The composition determined is Sm₁₄Co₅₈Cu₂₈. The atomic ratio between Sm and CoCu is about 1:6.1. As shown in Figure 1 and 2, there are only Sm(Co, Cu)₅ (0001) and (0002) peaks in XRD patterns, which means that only Sm(Co, Cu)₅ phase exists in the film grains. This implies that grain boundaries are either a Co or Cu rich phase. It is more likely that extra Cu atoms had diffused into the grain

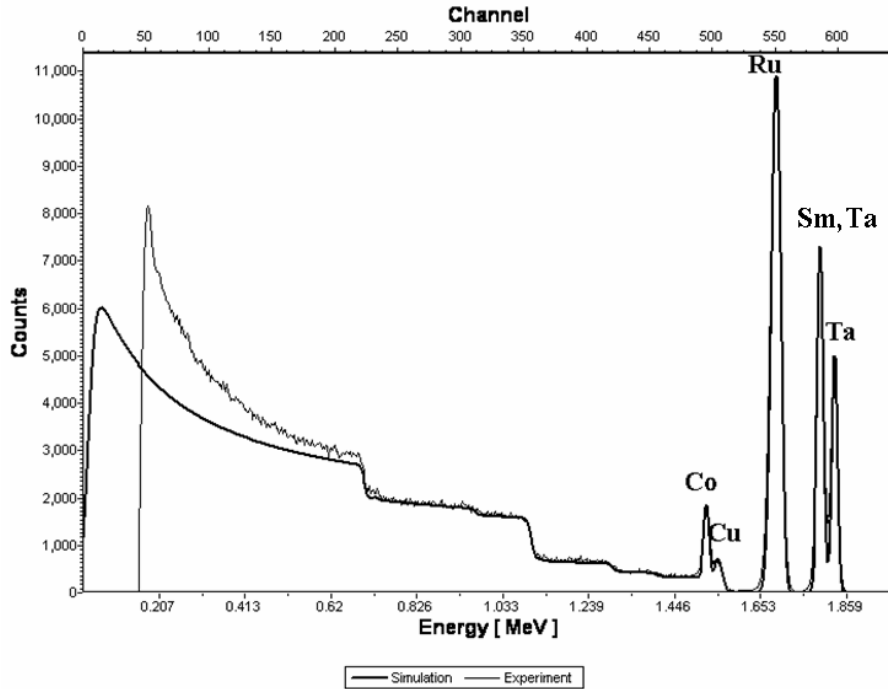


Figure 3 RBS spectra for Sm-Co-Cu films with structure

Ta(3nm)/Sm-Co-Cu(10nm)/Ru(4nm)/Ru(16nm)/Ta(4.2nm)/glass.

boundaries, because of their high mobility so that Cu atoms not only existed in the film grain, but also in the grain boundaries. This result shows that with a proper Cu composition, Sm-Co-Cu layer can form well crystallized $\text{Sm}(\text{Co}, \text{Cu})_5$ (0001) texture. This is supported by the studies of Cu addition in bulk SmCo_5 materials [19, 20]. Our attempt to fabricate Sm-Co film with perpendicular anisotropy without

proper Cu addition failed, which implies that Cu atoms existing in the lattice to stabilize SmCo₅ phase at relatively low temperature.

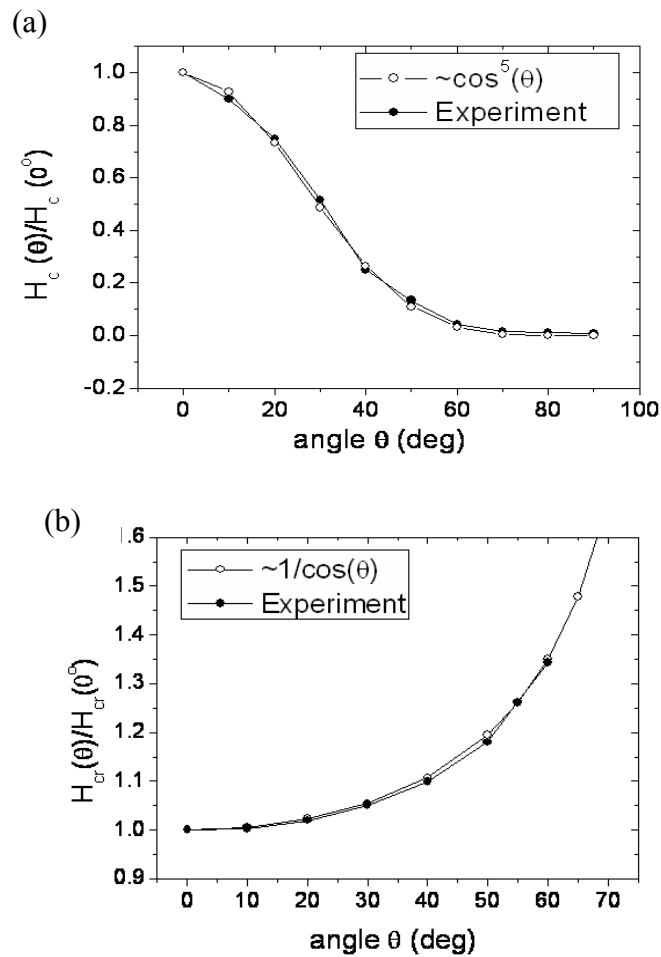


Figure 4 Angle dependence of (a) coercivity H_c and (b) remanence coercivity H_{cr} of Sm-Co-Cu film with structure Ta(3nm)/Sm-Co-Cu(10nm)/Ru(4nm)/Ru(16nm)/Ta(4.2nm)/glass (angles respect to the out-of-plane direction).

Figure 4 (a) and (b) show the experimental and fitting data of the angle dependences of coercivity (H_c) and remanence coercivity (H_{cr}) of the same sample shown in Figure 2 and 3. The angles in the figure were defined as the external field direction relative to the out-of-plane direction, which is films' easy axis direction. All the H_c and H_{cr} values were normalized by their values at zero degree. In Figure 4 (a), H_c keeps decreasing following the increase of angle and it is well-fitted by $H_c(\theta)/H_c(0) \sim \cos^5 \theta$. Figure 4 (b) shows that H_{cr} keeps increasing with the increase of angle, and follows $H_{cr}(\theta)/H_{cr}(0) \sim 1/\cos \theta$. We did not have experimental H_{cr} data for angles larger than 60° because the H_{cr} value exceeded the maximum field that our VSM could provide. The angle dependence of H_{cr} clearly shows that the magnetization reversal process of the Sm-Co-Cu films is dictated by magnetic domain wall movement (Kondorsky switching [25]). Meanwhile it is interesting to see a different angle dependence of H_c . This angle dependence is not only totally different from the Stoner-Wolfarth model but also can not be explained by a simple domain-wall movement model [26].

In this paper, we have discussed how Sm-Co-Cu films formed with a $\text{Sm}(\text{Co,Cu})_5$ (0001) textured structure having a high out-of-plane coercivity and high perpendicular magnetic anisotropy constant. As discussed in former sections, extra Cu atoms may exist in the grain boundaries. If a perfect exchange-decoupling between grains is assumed, the calculated coercivity based on the Stoner-Wolfarth model by using the estimated anisotropy field is about 350 kOe. This value is much

higher than the observed coercivity of only 11 kOe. This difference implies that Cu atoms may not form in grain boundaries to fully exchange-decouple the Sm-Co-Cu grains, which in agreement with the evidences of angle dependences of H_c and H_{cr} . A relatively strong exchange-coupling between grains in the obtained $\text{Sm}(\text{Co,Cu})_5$ films was also disclosed by the large coercivity squareness (S^*) as shown figure 2(a). However, if the SmCoCu layer is assumed to form a perfect continuous film with all Cu atoms staying in SmCoCu lattice, we also can't expect this relatively high coercivity based on the Kondorsky model that predicts an extremely low coercivity. Here we would like to propose a pinning-site model or the domain-wall pinning model to explain these observed magnetic properties. The Cu atoms or Cu clusters or the defects induced by the Cu additions may function as the pinning sites which will pin the domain-wall motion and result in a relatively higher coercivity. This is different from the pinning mechanism in Sm-Co hard magnets, in which the domain wall pinning is caused by the interfaces between two Sm-Co phases with different anisotropy values [27, 28]. This pinning-site model could point a way to explain the complicated behavior of H_c versus angle since the pinning sites in the films may not be uniformly distributed. Most of pinning sites exist in or around the grain boundaries. Since the Sm-Co-Cu films were deposited onto rotating substrate by co-sputtering Sm, Co and Cu targets, the film composition is uniform through the film. Thus, another possible high coercivity mechanism for continuous films, anisotropy fluctuation through films [29, 30], which is caused by the fluctuation of

film grain composition, should not work for our case. Therefore, the relatively high coercivity of these $\text{Sm}(\text{Co,Cu})_5$ films could be understood by a pinning-site mechanism. This result may imply a possible approach to fabricate a perpendicular medium with controllable pinning sites [31] and a recently proposed percolation perpendicular medium [32] if we could further understand and control the Cu addition and its induced defects.

4. Summary and Conclusions

In summary, a Ru(Cr) layer was successfully used as an underlayer to introduce the perpendicular magnetic anisotropy in polycrystalline $\text{Sm}(\text{Co,Cu})_5$ films. The usage of Ru(Cr) underlayer also reduced the grain size of SmCoCu layer to 17 nm, which could be further reduced by optimizing sputtering process parameters. Highly-ordered SmCo_5 phased Sm-Co-Cu sample with high perpendicular magnetic anisotropy ($1.4 \times 10^8 \text{ erg/cm}^3$) was prepared with perpendicular coercivity of 11 kOe and remanence squareness close to 1. Based on the angle dependences of coercivity H_c and remanence coercivity H_{cr} of the Sm-Co-Cu films, the magnetization reversal mechanism was identified to be domain-wall pinning.

Acknowledgements

This work has been partially supported by Seagate Research. Authors thank the useful discussion with Prof. Jack H. Judy at MINT Center, University of Minnesota.

References

- [1] K. J. Strnat, in *Ferromagnetic Materials*, edited by E. P. Wohlfarth and K. H. J. Buschow (North-Holland, Amsterdam, 1988), Vol. 4, Chap. 2, pp. 131-209, and references cited therein.
- [2] D.K. Das, *IEEE Trans. Magn.* 5, 214 (1969).
- [3] M.F. Doerner, et al., *IEEE Trans. Magn.* 36, 43 (2000)
- [4] R. Rani, F.J. Cadieu, X.R. Qian, W.A. Mendoza, S.A. Shaheen, *J. Appl. Phys.* 81,5634 (1997)
- [5] Y. Liu, R.A. Thomas, S.S. Malhotra, Z.S. Shan, S.H. Liou, D.J. Sellmyer, *J. Appl.Phys.*83, 6244 (1998)
- [6] V. Neu, S.A. Shaheen, *J. Appl. Phys.* 86, 7006 (1999)
- [7] E.M.T. Velu and D.N. Lambeth, *IEEE, Trans. Magn.*, Vol. 28, No. 5, 3249 (1992)
- [8] S. Takei, S. Shomura, A. Morisako, M. Matsumoto, and T. Haeiwa, *J. Appl. Phys.* 81,4674 (1997)
- [9] E. E. Fullerton, J. S. Jiang, C. Rehm, C. H. Sowers, S. D. Bader, J. B. Patel, and X.Z.Wu, *Appl. Phys. Lett.*, **71**, 1579, (1997).
- [10] A. Singh, R. Tamm, V. Neu, S. Fähler, C.-G. Oertel, W. Skrozki, L.Schultz,

and B. Holzapfel, *J. Appl. Phys.* 97, 093902, (2005).

- [11] A. Singh, V. Neu, R. Tamm, K. Subba Rao, S. Fähler, W. Skrotzki, L. Schultz and B. Holzapfel, *Appl. Phys. Lett.*, 87, 072505 (2005).
- [12] A. Singh, V. Neu, S. Fähler, K. Nenkov, L. Schultz, and B. Holzapfel, *Phys. Rev. B*, 77, 104443 (2008). (Published after our paper's first submission to APL)
- [13] J. Sayama, T. Asahi, K. Mizutani, and T. Osaka, *J. Phys. D* 37, L1 (2004).
- [14] S. Takei, A. Morisako, and M. Matsumoto, *J. Magn. Magn. Mater.*, 272-276, 1703 (2004).
- [15] I. Kato, S. Takei, X. Liu, and A. Morisako, *IEEE Trans. On Magn.*, Vol. 42, No.10,2366 (2006).
- [16] F. Hofer, *IEEE Trans. Magn.* Vol. 6, No. 221 (1970)
- [17] K. Kamino, Y. Kimura, T. Suzuki, Y. Itayama, *Trans. Jpn. Inst. Met.* 14, 135 (1973)
- [18] A.J. Perry, *J. Less-Common Met.* 51, 153 (1977)
- [19] W.Y. Zhang, X.D. Zhang, Y.C. Yang, B.G. Shen, *J. Alloy. Compd.* 353, 274 (2003)
- [20] E. Lectard, C.H. Allibert, R. Ballou, *J. Appl. Phys.* 75, 6277 (1994)
- [21] Shi JZ, Piramanayagam SN, Mah CS, et al. *Appl. Phys. Lett.*, 87 (22): Art. No. 222503 (2005)
- [22] F. Meyer-Liautaud, S. Derkaoui, etc, *J. Less-Common Met.* 127, 231 (1987)
- [23] J.C. Tellez-Blanco, et. al., *Journal of Alloys and Componds*, 281, 1-5 (1998)
- [24] T. Oikawa, et. al. *IEEE Trans. On Magn.*, 38, 1976 (2002)
- [25] E. Kondorsky, *J. Phys. (Moscow) II*, 161 (1940)
- [26] Robert C. O'Handley, "Modern Magnetic Materials: Principles and Applications", Wiley Inter-Science, 2000

-
- [27] R. Skomski, J. Appl. Phys., 81, 8 (1997)
- [28] H. Kronmuller and D. Goll, Physica B, 319, 122-126 (2002)
- [29] A.M.Gabay, P. Larson, I.I. Mazin, and G.C. Hadjipanayis, J. Phys. D 38, 1337 (2005)
- [30] Y.K. Takahashi, T. Ohkubo, and K. Hono, J. Appl. Phys. 100, 053912 (2006)
- [31] T. Suzuki, et. al., J. Appl. Phys., 85, 4301 (1999)
- [32] J. Zhu, and Y. Tang, J. Appl. Phys. 99, 08Q903 (2006)